Properties of Unusually Luminous Supernovae

Properties of Unusually Luminous Supernovae

A dissertation presented

by

Tony Shih Arng Pan

to

The Department of Physics

in partial fulfillment of the requirements

for the degree of

Doctor of Philosophy

in the subject of

Physics

Harvard University

Cambridge, Massachusetts

April 2013

Dissertation Advisor: Professor Abraham Loeb Tony Shih Arng Pan

Properties of Unusually Luminous Supernovae

Abstract

This thesis is a theoretical study of the progenitors, event rates, and observational properties of unusually luminous supernova (SN), and aims to identify promising directions for future observations.

In Chapter 2, we present model light curves and spectra of pair-instability supernovae (PISNe) over a range of progenitor masses and envelope structures for Pop III stars. We calculate the rates and detectability of PISNe, core-collapse supernovae (CCSNe), and Type Ia SNe at the Epoch of Reionization with the *James Webb Space Telescope* (JWST), which can be used to determine the contribution of Pop III versus Pop II stars toward ionizing the universe. Although CCSNe are the least intrinsically luminous supernovae, Chapter 5 shows that a JWST survey targeting known galaxy clusters with Einstein radii $> 35''$ should discover gravitationally lensed CCSNe at redshifts exceeding $z = 7$–8.

In Chapter 3, we explain the Pop II/I progenitors of observed PISNe in the local universe can be created via mergers in runaway collisions in young, dense star clusters, despite copious mass loss via line-driven winds. The PISN rate from this mechanism is consistent with the observed volumetric rate, and the *Large Synoptic Survey Telescope* could discover $\sim 10^2$ such PISNe per year. In Chapter 4, we identify 10 star clusters which may host PISN progenitors with masses up to $600 M_\odot$ formed via runaway collisions. We estimate the probabilities of these very massive stars being in eclipsing

binaries to be $\gtrsim 30\%$, and find that their transits can be detected even under the contamination of the background cluster light, due to mean transit depths of $\sim 10^6 L_\odot$.

In Chapter 6, we show that there could be X-ray analogues of optically super-luminous SNe that are powered by the conversion of the kinetic energy of SN ejecta into radiation upon its collision with a dense but optically-thin circumstellar shell. We find shell configurations that can convert a large fraction of the SN explosion energies into X-ray emission, producing unabsorbed X-ray luminosities of 10^{44} erg/s in events lasting a few months, or even 10^{45} erg/s flashes lasting days.

Contents

Acknowledgments

First and foremost, I'm grateful to my family for their unconditional love, support, and humor as I venture through life. I dedicate this work to my late father, and who above all else taught me to be curious.

My thesis advisor Avi Loeb has been a true mentor. Avi's enthusiasm is contagious and his breadth of knowledge in astrophysics is humbling. It has been incredibly fun to explore a wide range of ideas with Avi, many of which would not have reached fruition without Avi's insights. Avi always responded quickly to any questions I had, and supported my graduate career by advocating for me and sending me to conferences and schools early on. More than anything, I thank Avi for encouraging me to take risks, even when they take me to unusual places.

I sincerely thank Dan Kasen and Dan Patnaude – my collaborators for several of the papers comprising this thesis – for their contributions, suggestions, and guidance. I'm also grateful to Rennan Barkana – my collaborator on 21-cm cosmology research outside of this thesis – who graciously hosted my visit in Tel Aviv. Many other astronomers have shared their knowledge and technical expertise with me, and are acknowledged at the end of every chapter in this thesis.

I'm very much obliged to Chris Stubbs and Doug Finkbeiner at the Physics Department for their advice over the years. I also thank Sharad Ramanathan and Venkatesh Murthy at the Department of Molecular and Cellular Biology for allowing me to help build and teach the new Biological Signal Processing course.

I'd like to thank my fellow astrophysics graduate students Nick Stone, Eli Visbal,

Bob Penna, Laura Blecha, Gongjie Li for their help and friendship. I'd also like to thank my physics buddies from college – Mike McCourt, Mike Belyaev, John Rutherford, AJ Kumar – who've continued to help me as we all try to conquer graduate school. I'd also like to thank Alec Chapman, Adam Marblestone, and Dan Roberts for other entertaining science projects and conversations.

Finally, I am grateful to the Fannie and John Hertz Foundation, the Paul and Daisy Soros Foundation, and the National Science Foundation for their fellowship support. In particular, I owe a great debt to Philip Eckhoff and especially Lowell Wood of the Hertz community for broadening my horizons and for giving me incredible opportunities.

In Loving Memory of Dad

Chapter 1

Introduction

Supernovae (SNe), observed since antiquity, are extremely bright transients resulting from the explosion of stars. Their luminosity is so great that at the peak of their light curves, supernovae often outshine the combined output of the other billions of stars in their host galaxies. These spectacular explosions expel much of the stellar material at velocities as much as 10% the speed of light, and can leave behind exotic remnants such as neutron stars and black holes, or even completely unbind the star. Supernova expel into the interstellar medium the elements necessary for life that were forged in the furnaces of stars, and are responsible for creating the elements heavier than iron during explosive nucleosynthesis. The supernova explosion drives shock waves into the surrounding medium, shaping star formation and galaxy formation, and creating supernova remnants that are an important source of high-energy emission from X-rays to cosmic rays. Both the observational properties of supernova and their physical causes are diverse, ranging from the core collapse of massive stars, to the thermonuclear explosion of white dwarfs. The extraordinary brightness of supernovae allow them to act

as lighthouses into the distant universe, and their properties have been used to study cosmology, most notably in the discovery of dark energy.

Even among supernova, there are events that are unusually luminous. Although most supernovae have explosion energies of a few 10^{51} ergs, usually only 1% of that energy is released as optical emission during the supernova, with peak luminosities less than 10^{43} erg s^{-1}. However, in the past decade, numerous super-luminous supernovae (SLSNe) have been discovered with peak luminosities that are greater by a factor of ~ 10 (Gal-Yam 2012). The order-of-magnitude larger luminosities of SLSNe suggest that they may have unusual progenitors, and are powered by different physical mechanisms.

In particular, the pair-instability supernova (PISN), a type of SLSN powered by the radioactive decay of ^{56}Ni (with up to ~ 100 times the amount synthesized in regular core collapse SN), might be associated with the demise of the most massive stars $> 150 M_{\odot}$ exceeding the Galactic upper stellar mass limit. These massive stars reach extreme luminosities at very high surface temperatures, which drastically increase their ultraviolet flux and thus their ionizing efficiencies. Therefore, the progenitors of PISNe during the Cosmic Dawn, when the first sources of light turned on in the Universe, may have had an unique contribution toward the reionization of the intergalactic medium. Conversely, PISNe in the local universe are exceedingly rare, and may be associated with truly gargantuan stars with masses up to $\sim 10^3 M_{\odot}$, formed via mergers in extremely dense stellar environments. Alternatively, other types of SLSNe are powered by the conversion of kinetic energy into radiation via the collision of SN ejecta with circumstellar material. Regular supernovae may even masquerade as their luminous cousins via gravitational lensing by massive galaxy clusters.

In this thesis, we make theoretical predictions on a variety of luminous supernova, based on (1) whether they are intrinsically super-luminous or instead magnified via gravitational lensing, or (2) whether they are optically super-luminous powered via radioactive decay, or instead luminous in X-rays powered by circumstellar interactions, and (3) whether they have pristine progenitors from the first generation of stars during the Cosmic Dawn, or massive high-metallicity progenitors formed via successive mergers in the local universe.

1.1 Intrinsically luminous supernova

1.1.1 Powered by radioactive decay: Pair-instability Supernova

Pair-instability supernovae are thought to occur for stars with helium cores between $\sim$ 64 and $133 M_{\odot}$. Unlike their smaller counterparts, which form a dense iron core that eventually collapses under its own weight, the core of a PISN progenitor reaches extraordinarily high temperatures at relatively low densities, before the heavier elements have a chance to form. These conditions favor the runaway production of electron-positron pairs, which remove high-energy gamma-rays providing radiation pressure that supports the star. The resulting collapse leads to the explosive burning of oxygen, a thermonuclear event that reverses the collapse and ejects all of the stellar material, leaving no remnant behind. PISN progenitors near the upper end of the allowed mass range can synthesize several solar masses of ^{56}Ni, whose radioactive decay heats the otherwise cooling ejecta, and delays the inward-propagating recombination wave, resulting in a delayed light curve that peaks at 200-300 days after the explosion,

reaching extraordinary luminosities up to ~ -21.5 mag. This extended light curve is not replicated in other SLSNe, and may be the most important signature of PISNe.

Progenitor: Pop III stars at $z > 6$

After the Big Bang, as the universe expanded, cosmic gas eventually cooled to a point where electrons and protons combined to form neutral hydrogen at around a redshift of 1,100. This is when the universe became transparent, and photons that escaped during this recombination epoch form the cosmic microwave background we see today. Eventually, as perturbations in the density of cosmic gas grew under gravitational attraction, and collapsed to form stars and galaxies capable of radiating UV photons, the gas in the universe became ionized again between $6 < z < 20$ in the epoch of reionization. An interesting question is whether Pop III stars (the first generation of stars) were sufficient for ionizing most of the universe, or whether the budget of ionizing photons was dominated by Pop II stars (the second generation of stars), which formed from interstellar gas that had already been enriched by a prior burst of primordial star formation.

At zero metallicity, stars with initial stellar masses between ~ 140 and $260 M_{\odot}$ are thought to end their lives with sufficient core masses to explode as a pair-instability supernova. Since primordial clouds can only cool to ∼200–300 K (compared with ~ 10 K in line-cooled star-forming clouds enriched with metals), and the mass growth rate of stars during their formation is proportional to the gas cloud temperature $\propto T^{3/2}$, Pop III stars are thought to reach much larger masses of a few hundred $M_{\odot}$. Therefore, most PISNe may originate from Pop III progenitors, and serve as beacons for their presence.

In Chapter 2, we model the light curves and spectra of PISNe over a range of progenitor masses and structures, and calculate their detectability with the *James Webb Space Telescope* (JWST). We show that by using the observed rates of PISNe versus core-collapse SNe at $z > 6$, it is possible to constrain the stellar mass function at those times, and determine the contributions of Pop III and Pop II stars toward reionization. We also determine the rate of Type Ia supernovae, and show that contrary to prior literature, they are not rare toward the end of reionization, and can be used to probe the stellar mass function at $4 - 8M_{\odot}$, as well as independently map the ionization history of the intergalactic medium, albeit the latter requires an unrealistic survey time on JWST. If the production of ionizing UV photons was dominated by Pop III stars, we predict that the bright end of the galaxy luminosity function should be contaminated by PISNe.

Progenitor: Pop II/I stars in the local universe

In Chapter 3, we discuss the paradox that low-redshift PISNe, which have already been observed, require very massive progenitors with initial masses greatly exceeding the stellar mass limit inferred in the Milky Way, due to copious mass loss via line-driven winds. However, in young and extremely compact star clusters, dynamic friction can quickly sink all massive stars into the cluster center, which drive a runaway collision event in which many of the massive stars merge to form a very massive star that can serve as the Pop II/I progenitor of a PISN. We show the PISN rate from this mechanism is consistent with the observed volumetric rate at low redshifts of $\sim 2 \times 10^{-9}$ Mpc^{-3} yr^{-1}. We estimate that the *Large Synoptic Survey Telescope* can discover $\sim 10^2$ PISNe per year from the runaway collision merger product in star clusters, but can only observe PISNe out to redshift $z \approx 2$ despite their extreme luminosities.

In Chapter 4, we set out to find massive PISN progenitors in the local universe. We identify ten clusters that may host merged stars with masses up to $600M_{\odot}$ formed via runaway collisions. We also estimate that these stars have a $\gtrsim 30\%$ chance of being in eclipsing binaries with respect to observers on Earth. Although the very massive star cannot be spatially resolved from other stars in the dense star cluster core, we show that their transits can be detected with modest telescopes even under the contamination of the background cluster light, due to the large luminosity $\sim 10^7 L_{\odot}$ of the very massive star and the large associated transit depths.

1.1.2 Powered by circumstellar interaction: Super-luminous X-ray emission

A majority of SLSN light curves do not show the characteristic ~ 0.01 mag/day decay rate indicative of ^{56}Co, the daughter nuclide of ^{56}Ni, and are thus not primarily powered by radioactive decay. Instead, many of these SLSNe are associated with Type IIn supernovae, which show intermediate or narrow lines in their spectra, indicative of strong interactions of the SN ejecta with surrounding gas. If the mass of the circumstellar medium (CSM) gas is substantial compared to the SN ejecta mass, it can convert a large fraction of the SN ejecta's kinetic energy back into radiation. This mechanism has been used to explain observed super-luminous *optical* emission from supernova; in this thesis, we conjecture that if the SN ejecta collides with a dense but optically-thin CSM shell, much of the supernova energy may instead be released as super-luminous X-ray emission. In Chapter 6, we derive simple formulas for the X-ray luminosity from the resulting forward shock in the CSM shell as a function of the shell's mass, radius, and thickness,

for different regimes in which the shock will be radiative or adiabatic, and dominated by free-free emission or line-cooling emission. We find CSM shell configurations that can produce X-ray analogues of SLSNe, maintaining 10^{43} to 10^{44} erg s^{-1} luminosities over a few months. The most luminous events produce hard X-rays less prone to photoelectric absorption, and can negate absorption by completely ionizing the intervening unshocked CSM shell despite the latter's large column density. Regardless, once the shock traverses the entire CSM shell, the full luminosity could be available for observation.

1.2 Magnified supernova via gravitational lensing

Clusters of galaxies can act as gravitational lenses, focusing light-rays from sources behind them and magnifying their images. Current Hubble Space Telescope surveys are underway to observe galaxy clusters with high lensing strengths, i.e. with Einstein radii $> 35''$, to maximize the chance of observing high redshift galaxies, and it is likely JWST will have similar surveys. Supernova from the epoch of reionization situated behind these galaxy clusters could have their fluxes moderately boosted via gravitational lensing, raising them above the detection threshold and increasing their duration of visibility. In Chapter 5, we find the optimal JWST filter for detecting high redshift core collapse supernova, and estimate the expected number of magnified supernova observed around each gravitational lens.

Chapter 2

Pair-Instability Supernovae at the Epoch of Reionization

Tony Pan, Daniel Kasen, and Abraham Loeb.

The Monthly Notices of the Royal Astronomical Society, Vol. 422, Issue 3, pp. 2701-2711, 2012.

Abstract

Pristine stars with masses between ∼140 and 260 $M_\odot$ are theoretically predicted to die as pair-instability supernovae. These very massive progenitors could come from Pop III stars in the early universe. We model the light curves and spectra of pair-instability supernovae over a range of masses and envelope structures. At redshifts of reionization $z \geq 6$, we calculate the rates and detectability of pair-instability and core collapse supernovae, and show that with the *James Webb Space Telescope*, it is possible to

determine the contribution of Pop III and Pop II stars toward reionization by constraining the stellar initial mass function at that epoch using these supernovae. We also find the rates of Type Ia supernovae, and show that they are not rare during reionization, and can be used to probe the mass function at 4-8 $M_{\odot}$. If the budget of ionizing photons was dominated by contributions from top-heavy Pop III stars, we predict that the bright end of the galaxy luminosity function will be contaminated by pair-instability supernovae.

2.1 Introduction

The life of a massive star ends in a supernova (SN). The detection of neutrinos from SN 1987A verified the idea that some SNe are set off by the gravitational collapse of the iron core of their progenitor star (Krauss 1987). However, theory predicts that very massive stars with helium cores between ∼64 and 133 $M_{\odot}$ could find another way to blow up, through the thermonuclear explosion of oxygen via the pair-production instability (Rakavy & Shaviv 1967; Barkat et al. 1967; Heger & Woosley 2002). The production of electron/positron pairs in the core softens the equation of state, leading to collapse and the ignition of explosive oxygen burning. The subsequent thermonuclear runaway reverses the collapse and ejects the entire star, leaving no remnant behind. Unlike iron core-collapse supernovae (CCSNe), which involves poorly constrained physical processes such as turbulence, pulsations, perhaps rotation and magnetic fields, the physics involved in pair-instability supernovae (PISNe) is fairly well understood and can be modeled with fewer uncertainties (Langer 2009).

Due to the extremely large stellar mass required, the progenitors of PISNe are expected to be rare, and may only form under unusual conditions. One such condition

existed in the early universe, when metal-free Population III stars were born (Loeb 2010). In star formation, it is the accretion process that ultimately sets the final mass of a star. From dimensional arguments, the mass growth rate is simply given by the Jeans mass $M_J \sim c_s^3 G^{-\frac{3}{2}} \rho^{-\frac{1}{2}}$ over the free-fall time $t_{ff} \sim 1/\sqrt{G\rho}$, implying $dM/dt \propto c_s^3/G \propto T^{\frac{3}{2}}$, where the sound speed $c_s \sim \sqrt{kT/m_p}$. In present day star-forming regions, heavy elements radiatively cool the gas to a temperature as low as $T \sim 10$K. However, in primordial clouds, the primary coolant at low temperatures is molecular hydrogen, which can only cool the gas to $T \sim 200 - 300$K, implying an accretion rate higher than present day by two orders of magnitude. Hence, theoretical studies suggest that the initial mass function (IMF) of Pop III stars might have been biased toward masses much higher than today, e.g. several hundred $M_\odot$ (Bromm & Larson 2004). The nucleosynthesis imprints of this top heavy IMF have been seen in globular clusters and damped Lyman alpha systems (Cooke et al. 2011; Puzia et al. 2006). Moreover, massive stars have strong winds driven by radiation pressure through spectral lines, with a mass loss rate scaling with stellar metallicity $\dot{M} \propto Z^{0.5\sim0.7}$ (Vink et al. 2001; Kudritzki 2002). Most PISNe should therefore be from Pop III stars, which have weak radiation-driven winds due to their extremely low metallicities, and retain enough of their initial masses at the end of their lives to undergo a pair-instability explosion.

Naturally, studies of the rates and detectability of PISNe focused on high redshifts before reionization. Mackey et al. (2003) found the PISNe rate to be ~ 50 deg^{-2} yr^{-1} at $z > 15$, while Weinmann & Lilly (2005), using more conservative assumptions for the number of PISNe produced per unit Pop III stellar mass formed, found the PISNe rate to be ~ 4 deg^{-2} yr^{-1} at similar redshifts. Assuming that only one supermassive Pop III star forms in unenriched minihalos, and that none form in protogalaxies, Wise & Abel (2005)

found the PISNe rate be ~ 0.34 deg^{-2} yr^{-1} at $z \sim 20$. After our paper was submitted, Hummel et al. (2012) presented a complimentary analysis of the source density of PISNe from pristine minihalos, and determined the observability of such events with the *James Webb Space Telescope* (JWST), finding approximately ~ 0.4 PISNe visible per JWST field of view at any given time. PISNe after the epoch of reionization were also considered; Scannapieco et al. (2005) calculated a suite of PISNe model light curves with blackbody spectra, and analyzed the detectability and rates of PISNe from Pop III stars formed from leftover pristine gas at $z \lesssim 6$. As for CCSNe during reionization, Mesinger et al. (2006) presented detailed predictions for the number of core collapse SNe that JWST could observe as a function of different survey parameters.

In this paper, we present light curves and spectral time series for PISNe from our multi-wavelength radiation-hydrodynamics simulations. As the stellar population responsible for reionization is currently unknown, instead of predicting a fixed SNe rate, we normalize the star formation rate by requiring that enough ionizing photons must be produced by either Pop III or Pop II stars in protogalaxies to complete reionization by $z \sim 6$, and calculate the rates of pair-instability, core-collapse, and Type Ia SNe and their detectability with JWST for these two scenarios; the actual SNe rates will be in between these limiting cases. We show that using the observed rates of these SNe, it is possible to distinguish the contribution of Pop III and Pop II stars toward reionization by characterizing the IMF at that time.

2.2 Light Curves and Spectra

The stellar evolution and explosion of PISN models, and the resulting broadband light curves and spectral time-series are described in detail in Kasen et al. (2011); here we summarize the results. Models R150, R175, R200, R225, R250 represent explosions of 150-250 $M_\odot$ red supergiant stars, respectively, each with their hydrogen envelope intact. In principle, blue supergiants are also possible progenitors of PISNe, but convective mixing of metals into the hydrogen envelope makes it more likely that the progenitor dies as a red supergiant. Models He80, He100, He130 were explosions of 80, 100, 130 $M_\odot$ bare helium cores. Such models may represent stars that lost they hydrogen envelope due to a prior pulsational phase or through binary interactions. Here we use an approximate empirical relation between the helium core mass and the progenitor main-sequence mass (Heger & Woosley 2002):

$$M_{He} \approx \frac{13}{24}(M_{ZAMS} - 20M_\odot). \tag{2.1}$$

Properties of all presupernova stars and their explosions are given in Table 2.1.

A few days after the explosion, hydrodynamical processes subside and the ejected material reaches a phase of nearly free expansion. The energy powering the subsequent light curve may derive from three possible sources: (*i*) Lingering thermal energy from the explosion itself; (*ii*) The radioactive decay of synthesized ^{56}Ni; (*iii*) The interaction of the ejecta with a dense circumstellar medium. Thermal energy suffers adiabatic losses on the expansion timescale $t_{ex} = R_0/v$, and so source (*i*) is only significant for stars with large initial radii R_0. Circumstellar interaction has not been included in the models discussed here.

We have computed light curves and spectral time series of the explosion models using

Table 2.1: Parameters of supernova explosion models. The R-prefix models refer to red supergiant progenitor PISNe, and the He-prefix models refer to the exposed helium core PISNe. The proxy core-collapse SN model (CC), a model Type IIP supernova, is shown for comparison. R_0 is the presupernova radius. M_i, M_f are the initial and final masses of the progenitor, respectively, while M_{He} is the helium core mass and M_{Ni} is the amount of ^{56}Ni synthesized in the explosion. All mass units are in $M_\odot$.

Name	M_i	M_f	M_{He}	M_{Ni}	R_0 (10^{12}cm)
R150	150	142.9	72.0	0.07	162
R175	175	163.8	84.4	0.70	174
R200	200	181.1	96.7	5.09	184
R225	225	200.3	103.5	16.5	333
R250	250	236.3	124.0	37.86	225
He80	80	80	80	0.19	-
He100	100	100	100	5.00	-
He130	130	130	130	40.32	-
CC	15	13.3	-	0.28	44

the time dependent radiative transfer code SEDONA (Kasen et al. 2006). All models shown here assume spherical symmetry, and calculations of atomic level populations assume local thermodynamic equilibrium. Using Monte Carlo methods, we solve the full multi-wavelength radiative transfer problem using realistic opacities as a function of wavelength, composition and temperature, over millions of line transitions. Unlike previous blackbody models (Wise & Abel 2005; Scannapieco et al. 2005), our results allow us to calculate more accurate light curves for any given color bands and to study

the time evolution of the supernova colors and spectral features.

The shape and duration of PISN light curves depend on the mass and radius of their progenitors. Model R250 shows a weak and then strong peak in its light curve (Figure 2.1), the initial peak powered by thermal energy and the second by the radioactive decay of ^{56}Ni. The heating from radioactive decay delays the inward-propagating recombination wave from ejecta cooling, regulating the electron scattering opacity (and thus the release of thermal energy), and causing the second peak to rise at 200-300 days, which reaches a spectacular brightness of ~ -21.5 mag. However, model R150 produces very little ^{56}Ni, and therefore lacks a prominent second peak; the light curve is essentially thermally powered and reaches a brightness less than that of a Type Ia SN.

The helium core models are more compact and hence lack an initial thermal peak (Figure 2.2). Model He130 reaches an exceptional peak brightness of 2×10^{44} ergs s^{-1}, whereas Model He80 demonstrates that despite being massive and energetic, not all PISNe are bright. This steep mass-luminosity relation for PISNe suggests that to increase the sheer number of SNe detected, it is better to conduct a wide rather than deep survey of the sky (Weinmann & Lilly 2005).

The spectra of a PISN resemble that of average SNe, with P-Cygni line profiles on top of a blackbody, see Figures 2.3, 2.4. For the RSG models, at early times, the spectrum is rather featureless with only weak Balmer and calcium lines, reflecting the low abundance of metals in unburned ejecta. The spectral energy distributions of the models are blue at earlier times ($\lesssim 50$ days) but become redder over time as the expanding ejecta cools. In addition, line blanketing of the bluer wavelengths becomes more prominent over time, as the photosphere recedes into the deepest layers which

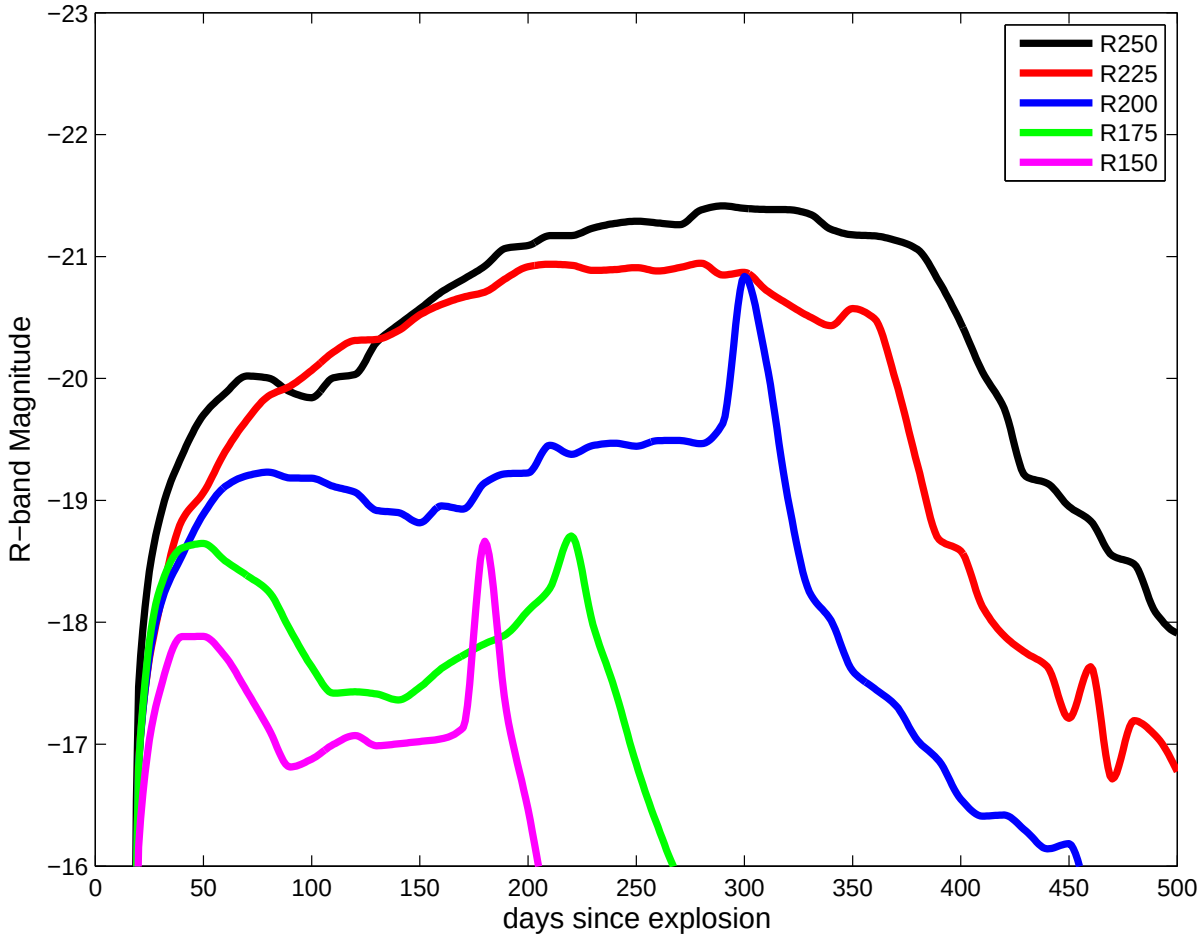

Figure 2.1.— Rest frame R-band light curves for the red supergiant progenitor models. In some models, a brief spike in luminosity occurs at the end plateau when radiation is released by hydrogen recombination. The sharpness of the spike may be exaggerated by the lack of numerical convergence of the ionization front recession.

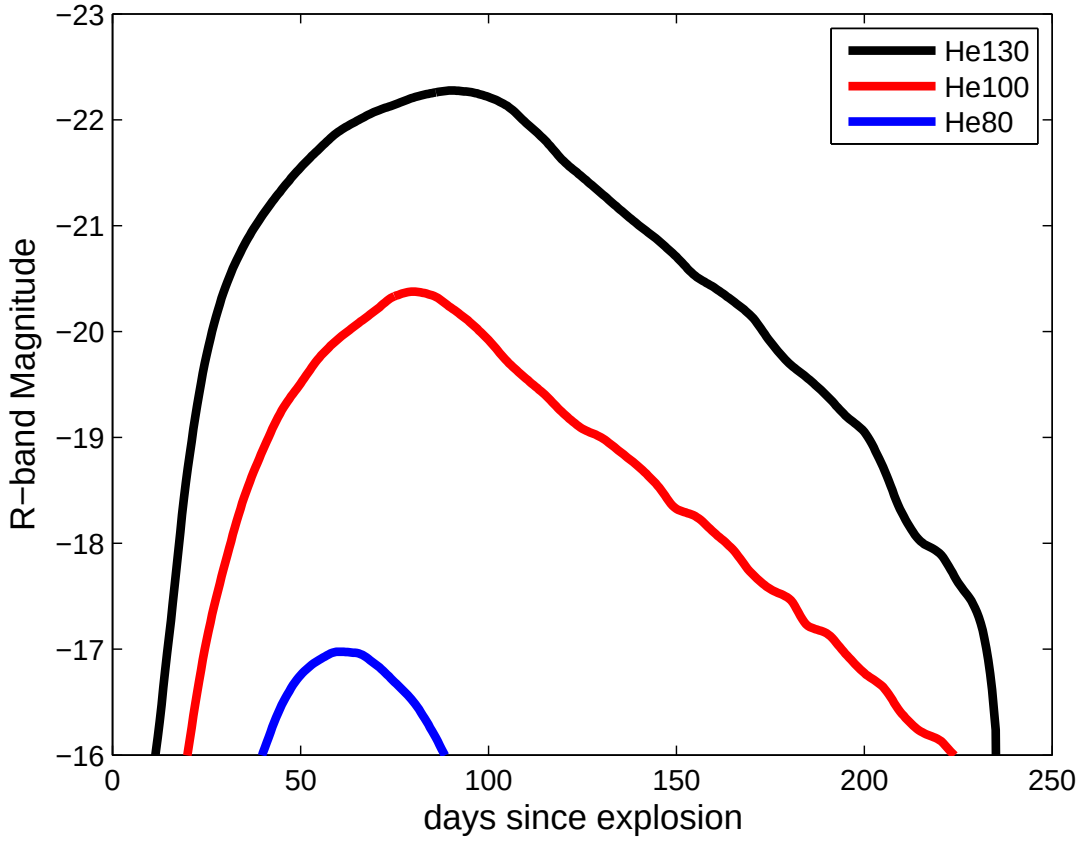

Figure 2.2.— Rest frame R-band light curves for the helium core progenitor models.

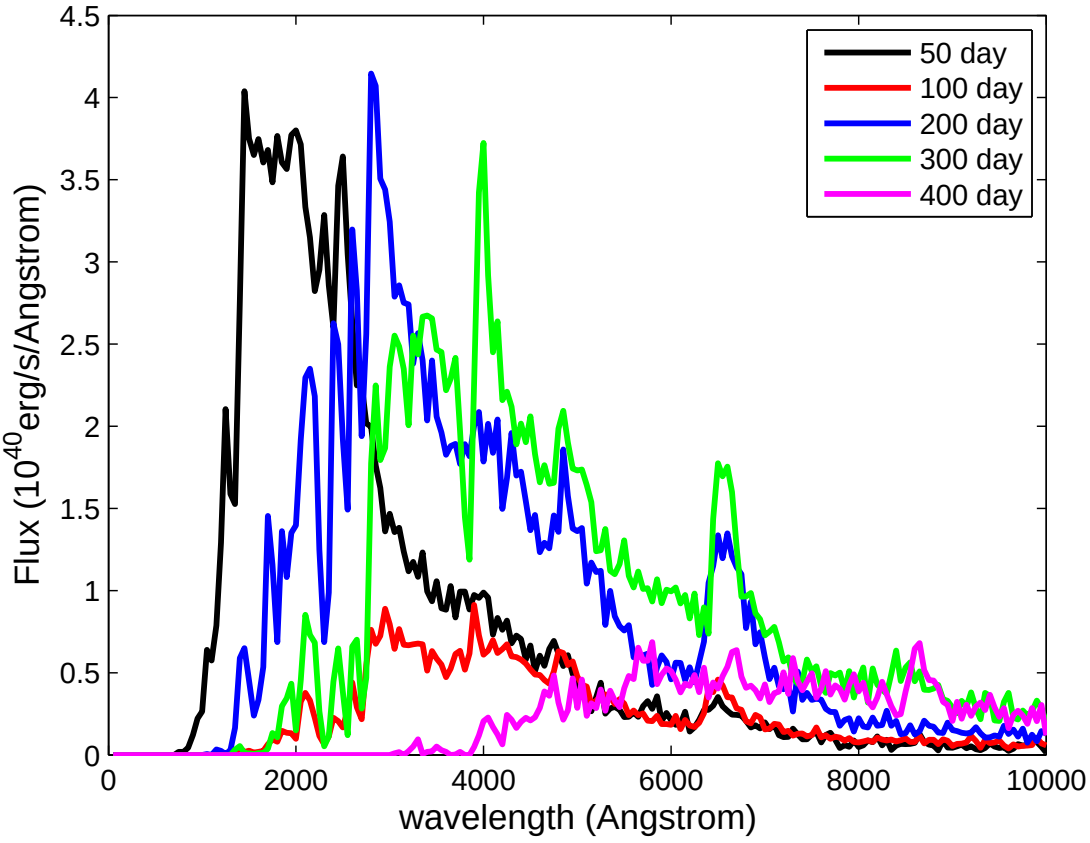

Figure 2.3.— Time evolution of the rest frame spectra for the R250 red supergiant model.

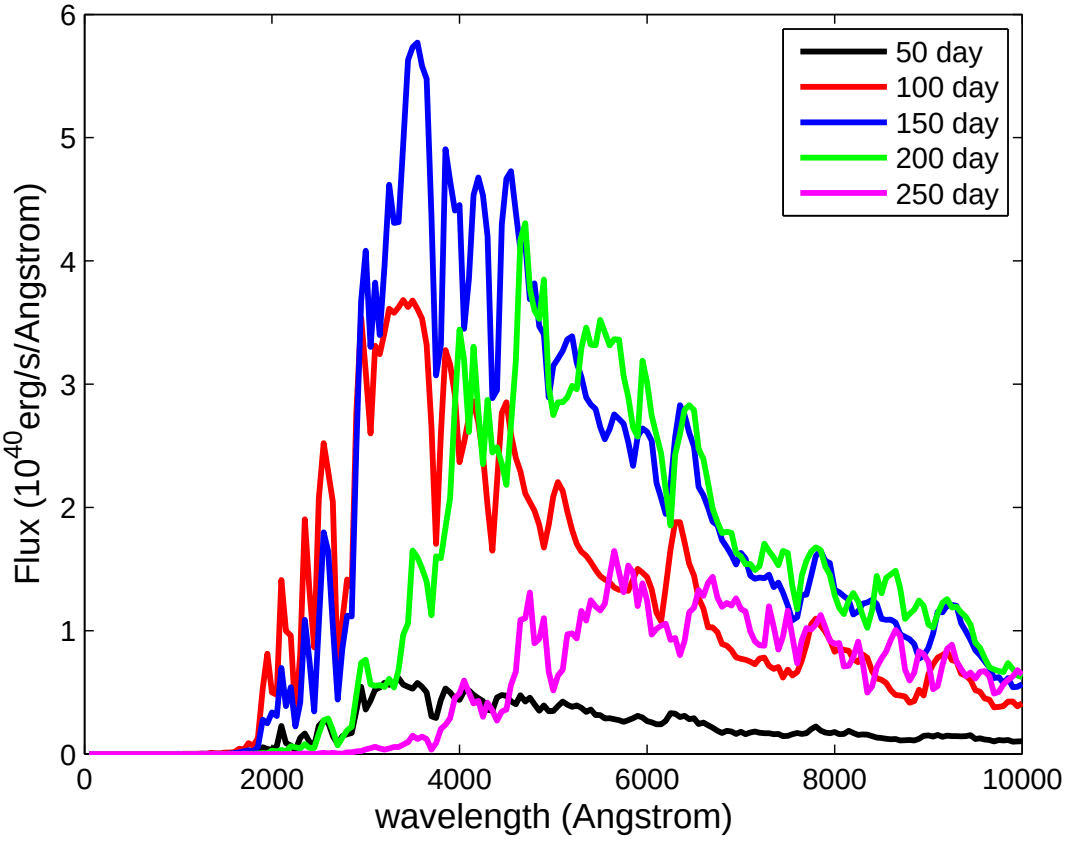

Figure 2.4.— Time evolution of the rest frame spectra for the He130 helium core model.

are abundant in freshly synthesized iron group elements. For PISNe at the redshifts of reionization, JWST will mostly be observing in the rest frame UV, so it is important to use more accurate spectral models, rather than the blackbody models of Scannapieco et al. (2005).

Spectroscopic or rest frame UV observations of PISNe may be able to constrain the metallicity of the progenitor star. However, the hydrogen envelope may be polluted by newly synthesized metals mixed out during the explosion. Chen et al. (2011) simulated multi-dimensional models of PISNe to predict the degree of mixing. They found relatively small fluid instabilities generated from burning at the boundaries of the oxygen shell, and concluded that PISNe keep their onion-shell structure in the explosion, until the reverse shock passes which generates Rayleigh-Taylor instabilities. This is in contrast with CCSNe, in which a shock runs through the inner metal-rich core, inducing the growth of instabilities and mixing. Also, ordinary Pop II/I CCSNe have non-zero metallicity in their hydrogen envelopes to begin with. Hence, metal lines in early-time spectroscopy might be able to distinguish PISNe from CCSNe, before the photosphere has receded deep into the ejecta. With a little mixing, N and possibly some C and O might appear in the early spectra of PISNe, but PISNe will not have any Si, Ni, Fe lines (Joggerst & Whalen 2011). This best applies to the red supergiant models, as the Helium core models undergo significant burning and have spectra that show many metal lines at maximum light.

2.3 Supernovae During Reionization

Observations of quasar absorption spectra (Fan et al. 2006) indicate that reionization was completed by $z = 6$. It is believed that most of the ionizing photons came from stars (Loeb 2010; Bouwens et al. 2011b). Although the very first stars could have ignited as early as $z \sim 30 - 40$, due to the exponential nature of structure formation, most of ionizing photons originated from stars born in the later stages of reionization at $z \sim 10$. Although it is not known which population of stars dominated at this epoch, an unusual stellar mass function 10-20 times more efficient than the standard Salpeter IMF in producing ionizing photons is required at $z \sim 6$ (Cen 2010). This favors the existence of a top-heavy Pop III stars at these redshifts, which may be observable via their extraordinary deaths as PISNe if the IMF included mostly stars between 140 and 260 $M_{\odot}$. Moreover, the observed rates of PISNe, CCSNe, and Type Ia SNe may be used to infer the IMF responsible for reionization at $z \gtrsim 6$.

2.3.1 The Initial Mass Function

The ionizing photon yield per baryon incorporated into present day stars with a Salpeter IMF is $\overline{\eta_{\gamma}} \sim 4000$. However, if the IMF is dominated by massive metal free stars ($M > 100 M_{\odot}$), then $\overline{\eta}$ can be up to a factor of 20 higher (Bromm et al. 2001; Raiter et al. 2010). The transition from Pop III to Pop II/I star formation is thought to occur at a critical metallicity of $Z_{crit} \sim 5 \times 10^{-4} Z_{\odot}$, above which cooling and fragmentation become efficient, which stops the preferential formation of massive stars (Bromm & Loeb 2003).

This transition can be associated with the assembly of atomic H cooling halos with virial temperatures $> 10^4$K (Haiman 2009). Molecular hydrogen is fragile to photodissociation, and the molecular coolant in halos are likely depleted after a single episode of metal free star formation. Therefore, molecular hydrogen halos are unlikely to allow continued formation of stars above Z_{crit}. Subsequent star formation only occurs when the deeper gravitational potential wells of atomic H cooling halos are assembled, corresponding to a virial temperature of $T_{vir} \approx 10^4$K and a minimum halo mass of $M_{halo} \approx 10^8 M_{\odot}$ The gas in these halos will thus have already gone through a burst of primordial star formation, and contain traces of metals, leading to Pop II star formation. Most of the photons responsible for reionization will come from the profusion of these Pop II stars in this scenario, although without contribution from Pop III stars, this may require an unrealistic star formation efficiency, see Figure 2.5.

There is another possibility. Most molecular H_2 cooling halos may not have formed stars at all, due to global H_2 photodissociation by an early cosmic background of 11.2-13.6 eV photons (the Lyman-Werner band), to which the universe is otherwise transparent. In this scenario, the majority of primordial star formation will appear in atomic H cooling halos with $M_{halo} \approx 10^8 M_{\odot}$. During blowouts from repeated SN explosions, these halos allow most of their self-generated metals to be accelerated into the IGM as SN ejecta, but, in contrast to smaller molecular H_2 cooling halos, these halos hold on to most of their interstellar gas (Mac Low & Ferrara 1999), and can have significant Pop III star formation. Coupled with the high ionizing efficiency of massive metal free stars, in this scenario Pop III stars will make a significant contribution to reionization.

Hence, we consider two mutually exclusive scenarios for reionization, where

either Pop III or Pop II stars reionize the universe; the actual star formation history of reionization will be in between these limiting cases. As for the IMF in each scenario, for massive, metal free Pop III stars, we use either a Salpeter IMF slope $dN/d\log M \propto M^{-1.35}$, or a flat IMF slope $dN/d\log M \propto M^{0}$ hinted by recent simulations (Clark et al. 2011; Greif et al. 2011), with $M_{upper} = 500M_{\odot}$ and $M_{lower} = 1M_{\odot}$. Note that the resulting PISN rates are not sensitive to the upper and lower mass bounds of reasonable Pop III IMFs. As long as $M_{upper} > 260M_{\odot}$, due to the steepness of dN/dM, there are not enough stars at the most massive end to affect the overall normalization. Moreover, for our SFR model described in the next section, any reasonable M_{lower} ranging from 0.1 - $10M_{\odot}$ makes negligible difference to the PISN rates of Pop III stars. This is because we normalize star formation by requiring the generation of enough stellar UV photons necessary to reionize the universe, and massive stars $M \gtrsim 10M_{\odot}$ are drastically more efficient at producing ionizing photons. In essence, we fix the number of massive stars produced in any IMF, but are free to vary the number of low mass stars, as the latter do not contribute to reionization anyway. $M_{lower} = 1M_{\odot}$ was chosen to match the smallest Pop III stars seen in recent simulations by Clark et al. (2011).

For Population II stars forming with traces of metals, we use a Salpeter IMF with $M_{upper} = 125M_{\odot}$ and $M_{lower} = 0.1M_{\odot}$, where we include a factor 0.7 in the mass integral to account for the reduced number of low mass stars in a realistic IMF (Fukugita et al. 1998), compared to the original Salpeter IMF. The different IMF models are tabulated in Table 2.2.

Table 2.2: Model parameters of the different IMFs. Here α is the slope of the stellar mass function, i.e. $dN/d\log M \propto M^{\alpha}$, and the slope of the Pop II IMF flattens at $M < 0.5M_{\odot}$. All mass units are in $M_{\odot}$.

IMF model $\phi(M)$	M_{lower}	M_{upper}	α	$\overline{\eta}_{\gamma}$
Pop III Salpeter	1	500	-1.35	28683
Pop III Flat	1	500	0	77087
Pop II	0.1	125	-1.35	5761

2.3.2 The Star Formation Rate

We calibrate the SFR by requiring enough UV photons are produced by stars so as to ionize the intergalactic medium (IGM) by the end of reionization. This requires $C \sim 10$ ionizing photons per baryon in the IGM, accounting for recombinations (Trac & Cen 2007). Using the time-averaged ionizing flux and stellar lifetime for individual stars from Schaerer (2002), we find the number of ionizing photons per baryon incorporated into stars $\eta_{\gamma}(M)$ as a function of stellar mass, for Pop III stars and early Pop II stars ($Z = 1/50Z_{\odot}$). For a given stellar track, the average ionizing photon per baryon in star is thus:

$$\overline{\eta}_{\gamma} = \frac{\int \eta_{\gamma}(M)\phi(M)MdM}{\int \phi(M)MdM}, \tag{2.2}$$

where $\phi(M)$ denotes the IMF. Then, the fraction of total baryons in the universe that are in stars $F_s(z)$ must satisfy:

$$\frac{F_s(z_{end})\overline{\eta}_{\gamma} f_{esc}}{C} = 1, \tag{2.3}$$

where z_{end} is the redshift at the end of Reionization, chosen to be $z_{end} = 6$ in our model, and where f_{esc} is the escape fraction of ionizing photons from the host galaxy

into the IGM. In the calibration of the SFR as a function of redshift, we assume the stars instantaneously produce all the ionizing photons at birth that they would normally produce during their lifetimes. For a fixed redshift of reionization, this will underestimate the SFR. Nevertheless, since most of the ionizing radiation was dominated by the massive stars ($M \gg 10 M_{\odot}$), with lifetimes < 10 Myr, this is an adequate approximation.

The mass in stars per comoving volume as a function of redshift, $\rho_*(z)$, can be related to the fraction of gas in halos which converts to stars, i.e. the star formation efficiency f_*, using the Sheth-Tormen mass function $\frac{dn}{dM}$ (Sheth & Tormen 1999) of halos:

$$\rho_*(z) = F_s(z)\rho_b = f_* \frac{\Omega_b}{\Omega_m} \int_{M_{min}}^{\infty} M \frac{dn(z)}{dM} dM. \tag{2.4}$$

Here ρ_b is the cosmological baryon density, and $M_{min} \sim 10^8 M_{\odot}$ for both Pop II and Pop III scenarios, corresponding to halos with atomic H cooling. For cosmological parameters used in generating the Sheth-Tormen mass function, we adopt $h = 0.71$, $\Omega_m = 0.27$, $\Omega_\Lambda = 0.73$, and $\Omega_b = 0.045$, where h is the Hubble constant in units of 100 km s^{-1} and Ω_m, Ω_Λ, and Ω_b are the total matter, vacuum, and baryonic densities in units of the critical density (Komatsu et al. 2011). Since $F_s(z_{end})$ is known via equation (2.3), by plugging $z = z_{end}$ into equation (2.4), we can calibrate the value of f_*, and evaluate $\rho_*(z)$ at any redshift. Although f_* will generally vary with redshift, here we take f_* as a constant for simplicity of calibration. The star formation rate is then simply:

$$SFR(z) = \frac{d\rho_*(z)}{dz}. \tag{2.5}$$

Figure 2.5 shows the resulting star formation rates, using $C = 10$ and $f_{esc} = 0.1$. Observations of Lyman-break galaxies around $z \sim 3$ suggests that f_{esc} could be larger at higher redshifts (Steidel et al. 2001). However, theoretically the high gas densities at the redshifts of the first galaxies could decrease the escape fraction down to $f_{esc} \lesssim 0.01$

(Wood & Loeb 2000), in which case using $f_{esc} = 0.1$ is a conservative choice that may underestimate the SFR and the corresponding SN rates. To consider different choices of these parameters, note that the SFR in our model linearly scales with C and f_{esc}^{-1}.

2.3.3 Snapshot Rate with JWST

The *James Webb Space Telescope*[1] (JWST) will include a Near Infrared Camera (NIRCam), with a spectral coverage from 0.6-5 μm with $\sim$10 nJy sensitivities in 10^4 s of integration time (10σ); a Near Infrared Spectrograph (NIRSpec) which operates at approximately the same wavelength range. The Mid InfraRed Instrument (MIRI) covers 5-27 μm, but is an order of magnitude less sensitive than NIRCam. Since isolated Pop III stars are likely beyond the reach of JWST, to test the prediction that metal-free stars had a top-heavy IMF (which has been recently debated, see Hosokawa et al. (2011)), we can either observe the cumulative properties of the first stars by imaging Pop III galaxies (Zackrisson et al. 2011), or detect their deaths as extraordinary bright supernova.

The number of new events at a given redshift that can be observed per unit solid angle is (Woods & Loeb 1998):

$$N(z) = R(z)\,(1+z)^{-1}\,\frac{dV_c}{dz},\ \text{for}\ z < z_{max(F;\nu)}, \tag{2.6}$$

where $z_{max(F;\nu)}$ is the maximum redshift at which a source will appear brighter than limiting flux F at an observed frequency ν, $R(z)$ is the event rate per unit comoving volume, and dV_c is the cosmology-dependent comoving volume element corresponding to a redshift interval dz. The above expression includes the (1+z) reduction in apparent rate owing to cosmic time dilation.

[1] http://www.jwst.nasa.gov/

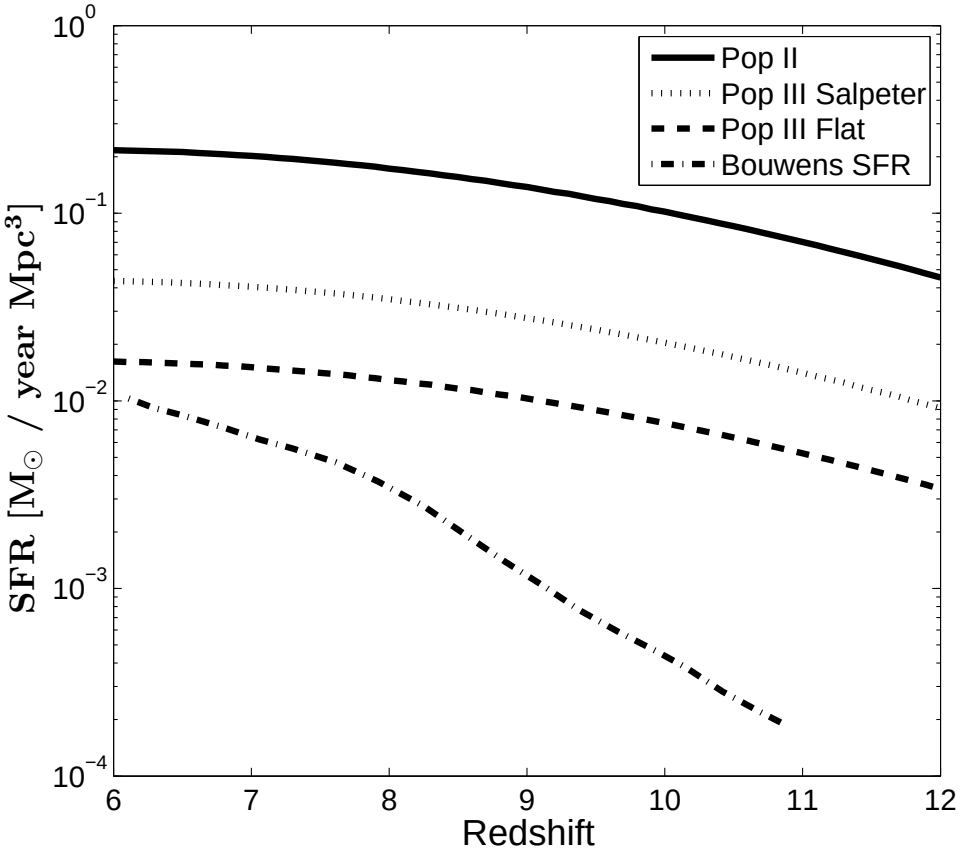

Figure 2.5.— The SFR for Pop II or Pop III stars required to reionize the universe by $z_{end} = 6$. The calibrated star formation rate is $f_* = 0.3\%$, 0.8%, and the unrealistically high 24.1% for the Pop III Flat, Pop III Salpeter, and Pop II IMF models, respectively, suggesting that Pop II stars could not have driven reionization by themselves. The SFR inferred by Bouwens et al. (2011c) from integrating the observed galaxy UV luminosity densities to $M_{AB} \approx 18$ is plotted for comparison; their substantially lower SFR is not surprising, as the contribution from the very steep faint-end slope of lower-luminosity galaxies was omitted (Bouwens et al. 2011a). The SFR for our models and the resulting SN rates all linearly scale with C and f_{esc}^{-1}. $C = 10$ and $f_{esc} = 0.1$ were used throughout this paper.

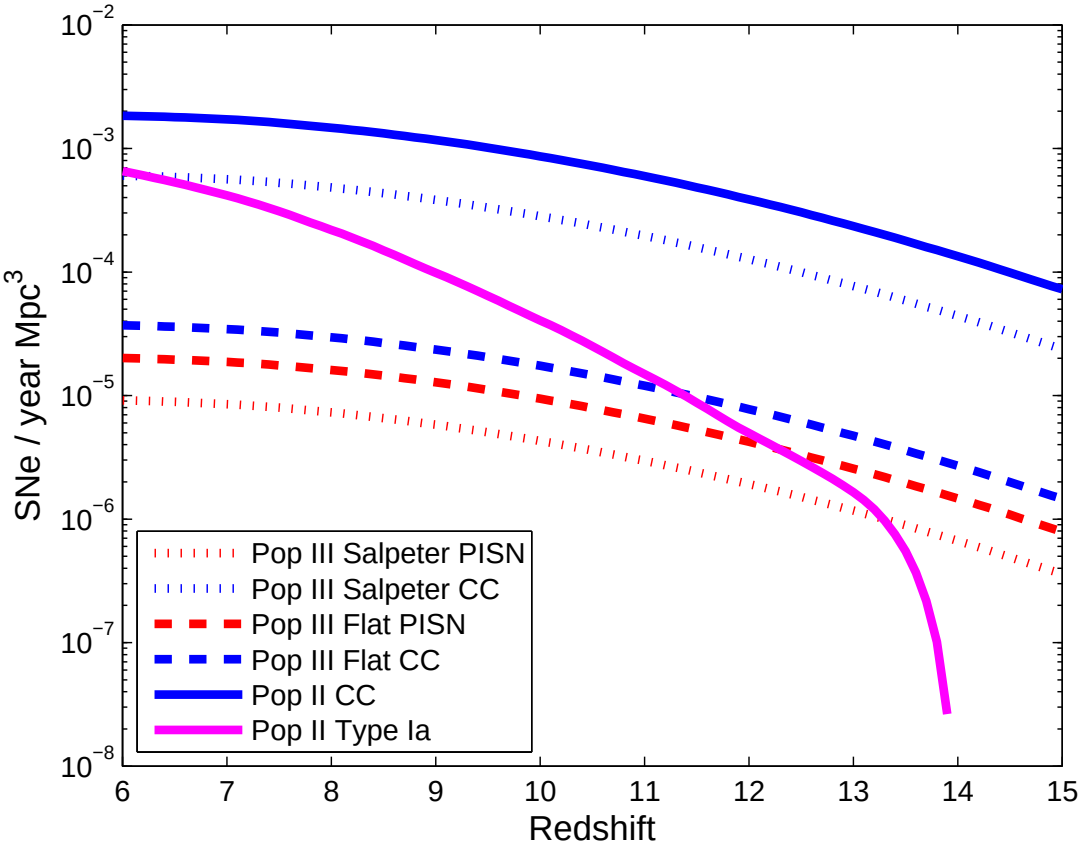

Figure 2.6.— The rate $R(z)$ of PISNe, CCSNe, and Type Ia SNe for our different IMF models for the stellar population responsible for reionization, per year per Mpc^3.

The 'snapshot rate', i.e. the total number of events (not per unit time) observed at limiting flux F is:

$$N(F;\nu) = \int_0^\infty dz\, R(z)\, t(z;F;\nu)\, \frac{dV_c}{dz}, \tag{2.7}$$

where $t(z;F;\nu)$ is the rest-frame duration over which an event will be brighter than the limiting flux F at redshift z for an observed frequency ν. We find this duration from our spectral time series calculated with SEDONA. There is an implicit $(1+z)$ factor in equation (2.7) due to the time dilation of the light curve, but that cancels with the $(1+z)^{-1}$ reduction in apparent rate. Although $t(z;F;\nu)$ of PISNe will generally be longer for more massive progenitors, the snapshot rate is not necessarily dominated by the highest mass stars, as they are less numerous, see Figures 2.7 and 2.8. For CCSNe, it is not clear how the brightness of a Type IIP SN should depend on the mass of the progenitor star; here we use light curves of a $15M_\odot$ red giant progenitor generated with SEDONA (Kasen & Woosley 2009), whose broadband light curves and spectra agree very well with observed Type IIP SNe, which are observed to be the most common, at least in the nearby universe. However, this single CCSN model means we do not capture the variation in CCSN peak flux from different progenitors, which we do so for PISNe.

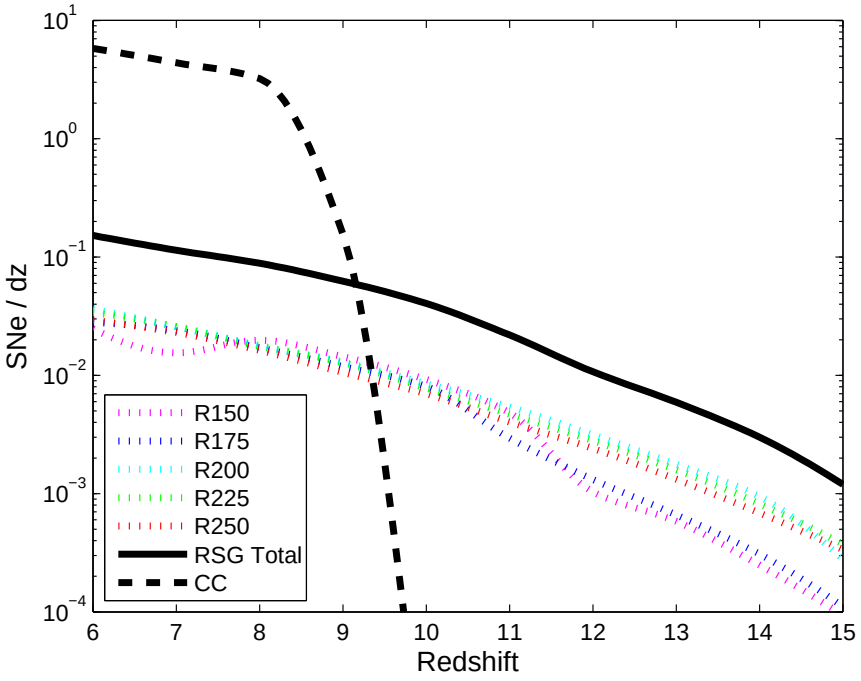

Figure 2.7.— Differential snapshot rate $\frac{dN(F;\nu)}{dz}$ for the Pop III Salpeter IMF model, in the 10 arcsec^2 field-of-view of NIRCam on JWST, calculated using the sensitivities of the F444W filter (44400 Å) with $t = 3 \times 10^4$s integration time at 5σ (a flux threshold of 2 nJy). At this sensitivity, each type of SN appears in rough proportion to their actual event rates (Figure 2.6) up to $z \sim 8$, past which the ratio of detected PISNe versus CCSNe turns over, with only the brighter PISNe staying in view. As we have not accounted for the intrinsic scatter in the luminosity of CCSNe, the actual turnover will be less sharp. A similar turnover exists for the less massive PISN models R175, R150 starting at $z \sim 11$, past which the more massive progenitors are more likely to be seen in the field of view despite being less numerous in number given the IMF. The snapshot rate of CCSNe in Figure 2.7 is less than that implied in Mesinger et al. (2006), as their assumed IMF is closer to our Pop II IMF model.

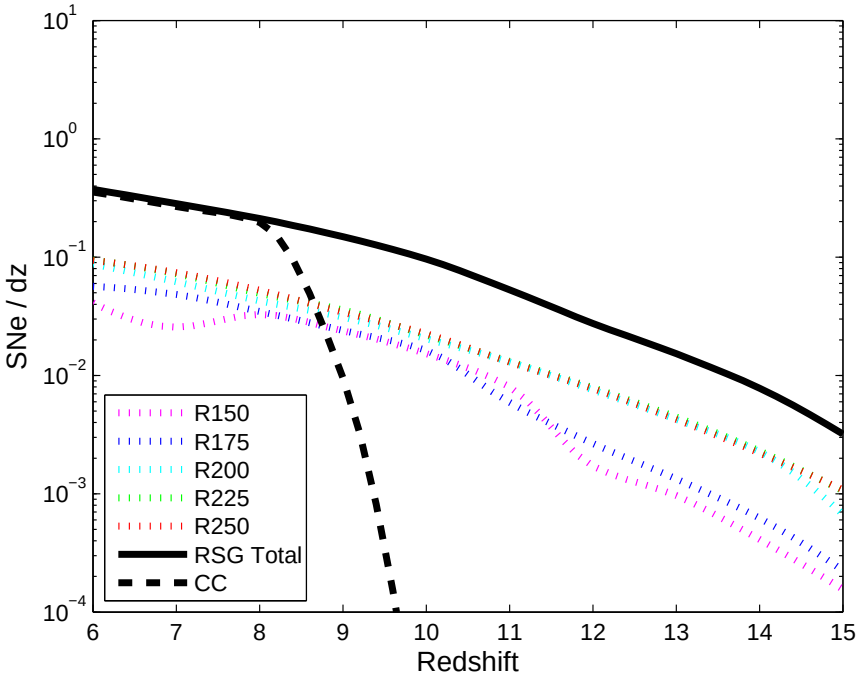

Figure 2.8.— Differential snapshot rate $\frac{dN(F;\nu)}{dz}$ for the Pop III Flat IMF model, in the 10 arcsec^2 field-of-view of NIRCam on JWST, with the same survey parameters as Figure 2.7.

Table 2.3: Snapshot rate in NIRCam's field of view (10 arcsec^2) on JWST, using the same survey parameters as Figures 2.7 and 2.8. This is the total number of PISNe and CCSNe in each NIRCam snapshot, integrated across $z \geq 6$, for the different IMF models. One can multiply the values below by 360 to get the snapshot rate per deg^2. It is not clear what fraction of PISNe explode from red supergiants (RSG) versus exposed helium cores; the rates shown in the RSG and He Core columns assume all PISN explode as that type. Here the snapshot rate of PISNe from red supergiants is higher than the helium core model due to the longer duration of the former. The snapshot rate for CCSNe in our Pop II IMF scenario is in good agreement with the high end estimate of 24 SNe per field found by Mesinger et al. (2006) under similar survey parameters.

IMF model	He Core	RSG	CC
Pop III Salpeter	0.28	0.42	10.43
Pop III Flat	0.74	1.03	0.64
Pop II	0	0	31.83

Table 2.4: Snapshot rate in MIRI's field of view (2.35 arcsec^2) on JWST, using the F770W filter (77000 Å) with 3×10^4s exposure (5σ). The resulting snapshot rate is an order of magnitude worse than NIRCam; however, these results suggest that MIRI can be used as a follow-up instrument to distinguish bright PISN events from core-collapse events. Since MIRI is much less sensitive, the brighter He core models are more readily observable, while CCSNe cannot be seen at all in this integration time.

IMF model	He Core	RSG	CC
Pop III Salpeter	0.05	0.04	0
Pop III Flat	0.15	0.12	0
Pop II	0	0	0

PISNe and CCSNe occur for stars with main-sequence masses between ∼140-260$M_\odot$ (Heger & Woosley 2002) and 8-25$M_\odot$ (Smartt 2009), respectively. The fate of stars between 25-140$M_\odot$ is uncertain; due to fallback, progenitors more massive than $\sim 40M_\odot$ may form black holes directly with no SN explosion (Fryer 1999). Notably, stars in the mass range 95-130$M_\odot$ may reach the pair production instability in the core, but the thermonuclear explosion is insufficient to unbind the star (Woosley et al. 2007), and the star undergoes pulsations of matter ejecta which may produce a very bright light curve when the shells of ejected matter collide with each other, before the star dies as a normal CCSN. The resulting pulsation pair-instability supernova can be ultra-luminous and are presumably detectable by JWST. However, we do not consider such events here.

Using a progenitor mass range of 8-25$M_\odot$ to calculate the CCSN rates is likely an underestimate; for detailed predictions on the number of CCSNe detectable by JWST at the redshifts of reionization, see Mesinger et al. (2006), who also take into account the

variation in peak magnitude of observed CCSNe and the effects of dust extinction. For a fixed progenitor mass range, we calculate the SN rate per comoving volume $R(z)$ and find the snapshot rate shown in Tables 2.3, 2.4 and Figures 2.6, 2.7, 2.8. For the latter two figures, we use each red supergiant model as a proxy for the light curves of all progenitors similar in mass, e.g. R250 represents all progenitors in mass range 226-260$M_{\odot}$.

If both Pop III and Pop II stars contributed to reionization, the actual IMF will be a mixture of the Pop III and Pop II IMF used above. By counting the number of each type of SN found in JWST snapshots, the IMF of these early stellar populations can be constrained, and the relative contribution of Pop III and Pop II stars toward reionizing the universe can be inferred. To reduce selection effects due to the different intrinsic luminosity of the SN, a sufficiently deep exposure is needed, to enable observations of both types of SNe at the peak of their light curves should they exist at the target redshift.

For the integration time assumed in Figure 2.7 and 2.8, one can directly characterize the ratio of PISNe to CCSNe before $z \sim 8$, and set existence limits on top heavy Pop III stars up to $z \sim 10$ with a survey of ~ 10 JWST fields.

2.3.4 Probing Intermediate Mass Stars with Type Ia SNe

To probe the intermediate mass range ($\sim 1 - 8M_{\odot}$) of the IMF during reionization, one may use Type Ia SN rates. Type Ia supernovae (SNe Ia) are thought to occur when a white dwarf nears the Chandrasekhar mass, resulting in a thermonuclear explosion. This requires the white dwarf to accrete mass from a binary companion. Although the physics behind SNe Ia have been widely studied using both observations and theoretical

simulations, there is still no consensus on the mechanisms that proceed the supernova. The single degenerate model proposes the companion to be a main sequence or giant star, which donates mass via Roche lobe overflow, whereas the double degenerate scenario considers the merger of two white dwarf stars; the latter may be necessary for at least some observed Type Ia SNe (Bloom et al. 2012; Schaefer & Pagnotta 2012). Either way, after stellar birth it takes the main sequence lifetime of the progenitor star plus an additional delay time for the Type Ia SN to proceed.

Hence, the rate of SNe Ia is empirically parametrized to follow the star formation rate (SFR), but shifted toward lower redshift after taking the delay time into account. The SN rate at a redshift z or cosmic time t, $R(z) = R(t)$, is given by a convolution of the SFR over delay times,

$$R(t) = \int_0^t SFR(t-\tau)\mathrm{DTD}(\tau)d\tau, \tag{2.8}$$

where $\mathrm{DTD}(\tau)$ is the delay time distribution (SNe per unit time per unit stellar mass formed), in which τ is the time elapsed between the formation of the progenitor star and the explosion of the SN Ia. Note that since the $\mathrm{DTD}(\tau)$ is normalized to the total stellar mass formed, it only indirectly reflects the physical efficiency of SNe Ia from their actual progenitors of $3 - 8M_{\odot}$ stars (Nomoto et al. 1994).

In previous reionization literature (Haiman 2009), Type Ia SNe were expected to be extremely rare at high redshifts ($z > 6$), as the delay between the formation of the progenitor and the SN event was thought to be longer than the age of the Universe at these redshifts. However, this view should be reconsidered in light of recent converging evidence for a prompt population of SNe Ia, see recent work by Maoz (2010), Graur et al. (2011), and references within.

Scannapieco & Bildsten (2005) calibrated the prompt rate via the 'B' parameter, a constant of proportionality between the SFR and the prompt SN Ia rate, equivalent to the number of prompt SNe per unit stellar mass formed. The delayed component is characterized via the parameter 'A' which is the constant of proportionality between galaxy mass and the delayed SN Ia rate. We ignore the A component as this delay exceeds the age of the universe during reionization. The value of B is calibrated at low redshifts, for example $B = 2.7 - 11 \times 10^{-3} M_{\odot}^{-1}$ in Maoz & Badenes (2010), for prompt delay times $T \in (35, 330)$ Myr; here we adopt $B = 3 \times 10^{-3} M_{\odot}^{-1}$. From B, we set a uniform DTD(τ) $= B/\Delta T$. Using the Pop II SFR and this DTD(τ), we calculate the event rate $R(t)$ of Type Ia SNe shown in Figures 2.6 and 2.9. Since the validity of these estimates depend on DTD(τ), we assume that the astrophysics involved in shaping the forming efficiency and delay time of Type Ia SNe is not very sensitive to the cosmological epoch.

As seen in Figure 2.9, in the scenario where Pop II stars dominated reionization, we expect $\sim$1 new SNe Ia every year per unit redshift at $z \sim 6-7$ in NIRCam's field of view of ≈ 10 square arcseconds. As the AB magnitude of SNe Ia during peak (Hillebrandt & Niemeyer 2000) is $M_B \sim M_V \sim -19.30$ with a dispersion of 0.3, several hours integration time on JWST will be sufficient to catch a Type Ia SN near peak flux at these redshifts.

Regardless of which population of stars dominated reionization, Type Ia SNe offers a way to probe the intermediate mass range of the reionization IMF. In addition, the $z \gtrsim 6$ sky offers an unambiguous way of isolating a prompt population of SNe Ia, as the universe was not sufficiently old in the epoch of reionization for the delayed component of Type Ia SNe to contribute any events. Therefore, Type Ia SNe at $z > 6$ could be used to test whether the delay times are indeed connected to SN Ia formation mechanisms and

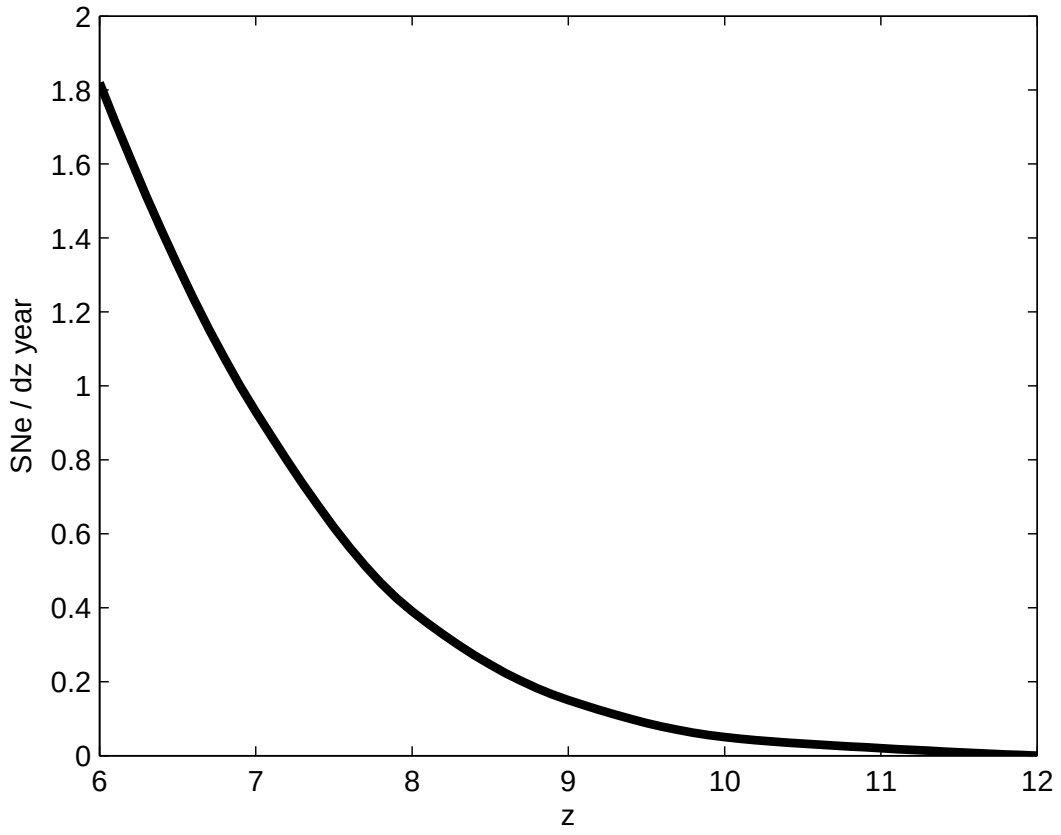

Figure 2.9.— Type Ia SNe rate in NIRCam's field of view, per year of observation per dz. For the Pop II IMF model for reionization, $\sim$1 new SNe Ia will occur every year per unit redshift at $z \sim 6-7$ in NIRCam's field of view. The 20 days around the SN Ia peak flux at that redshift is equivalent to half a year in observer frame. Every NIRCam snapshot of the sky, with sufficient integration time (e.g. 3×10^4 s to get absolute magnitude above -18 at $z = 8$ with signal-to-noise ratio of 5), will have a $\sim 50\%$ probability of finding a Type Ia SN near peak flux.

properties. Finally, the existence of standard candles during the epoch of reionization could be useful for cosmological measurements. In the Appendix, we discuss that probing reionization history with Type Ia SNe by constraining the global ionization fraction using Thomson optical depth measurements requires an unrealistic survey time for JWST.

2.3.5 Typing the Supernovae

At lower redshifts, SNe are usually typed by spectral lines. Furthermore, the smoking gun evidence for a PISN is the measurement of a large core ($> 50M_{\odot}$) composed of helium or other heavier elements. In the case of SN 2007bi, Gal-Yam et al. (2009) analyzed the nebular spectrum 16 months after peak light to infer $\sim 4M_{\odot}$ of ^{56}Ni, implying a large core mass $> 50M_{\odot}$ as in a pair-instability explosion (but see Moriya et al. (2010) for a CCSN model for SN 2007bi that ejects $6.1M_{\odot}$ of ^{56}Ni). However, spectroscopic typing of high redshift SNe seen by JWST may be unrealistic; for example, at around 3 μm on NIRSpec, achieving a signal-to-noise ratio of 5 at redshift ~ 8 would require one full day of integration time. Alternatively, in anticipation of Pan-STARRS[2] and LSST[3] increasing the number of photometrically detected SNe to a few hundred thousand in the next two decades, much work has been done in the photometric identification and classification of SNe (Kessler et al. 2010). As photometric classification of SNe matures, it could complement or replace the spectroscopic typing of high-z SNe, reducing the required JWST time.

The light curves of the more massive PISNe are very luminous (10^{43}-10^{44} erg s^{-1}) and long-lasting ($\sim$ 300 days), characteristics that do not exist for most other types of

[2]http://pan-starrs.ifa.hawaii.edu/public

[3]http://www.lsst.org/lsst/

SNe. As long as the SN redshift is known, multi-epoch observations can determine its rest-frame luminosity and duration, and identify the more massive PISNe explosions. Aside from the most energetic events, typing PISNe using their magnitude and color will be difficult. Despite their enormous kinetic energies of $\sim 10^{53}$ ergs, the peak optical luminosities of PISNe are similar to those of other SNe, even falling below the Ia and II curves for smaller mass progenitors. The majority of PISNe will actually be these dimmer events. Also, since PISNe spend most of their lives in the same temperature range as other SNe, their colors are also similar.

An extended light curve, rather than an extreme luminosity or unusual color, may therefore be the most important signature of PISNe. In particular, the distinguishing feature of PISNe is its exceptionally long rise time, $\gg 100$ days in the rest frame. Also, the detection of a slow decline rate that follows the decay rate ($\sim$0.01 mag/day) of ^{56}Co, the product of ^{56}Ni decay, would provide strong evidence that the SN synthesized significant amounts of ^{56}Ni. At $z = 8$, even with time dilation, this results in $\sim$0.4 mag variation per year, which should be within the sensitivity of a multi-year JWST survey; the decline in the bluer bands are 2-3 times larger, due to the onset of iron group line blanketing. The detection of a secondary maximum in the light curve also supports the synthesis of ^{56}Ni. However, the lack of a secondary peak does not rule out a large presence of ^{56}Ni, as strong radial mixing could smear out the two bumps (Kasen 2006).

2.3.6 Survey Strategies

The long duration of high redshift PISN light curves, prolonged by cosmological time dilation, poses a great challenge for detecting them as transients. At z$\sim$7 the light curve

of a PISN can last for over 1000 days in the observer's frame. Without spectroscopic measurements, the telltale sign of a massive progenitor PISN is an incredibly long plateau in its light curve. Therefore, instead of a threshold experiment, we suggest a search strategy that involves taking a series of 'snapshots' of a field, each snapshot separated by ~ 1 year, and searching for variations in the flux of objects in successive images. Since Pop III star formation occurs in the smallest galaxies, blank-field surveys should be the sufficient for searching for PISNe.

The total number of SNe detected in a survey of total integration time t_{surv} is

$$N_{surv} = \frac{1}{2}\frac{t_{surv}}{t_{exp}}\frac{\Delta\Omega_{FOV}}{4\pi}N_{exp}, \tag{2.9}$$

where $\Delta\Omega_{FOV}$ is the instrument's field of view, t_{surv}/t_{exp} is the number of fields which can be tiled within the survey time t_{surv}, and N_{exp} is the snapshot rate from equation (2.7), i.e. the number of SNe bright enough to be detected in an exposure of duration t_{exp} (Haiman 2009). The factor of $\frac{1}{2}$ is included to account for observations in 4 color bands (2 pairs of filters, as NIRCam observes in two bands simultaneously using a dichroic) for determining photometric redshift and typing of the SNe. To detect SNe by their variability, each field requires repeated observations, and therefore any survey should piggyback on fields that have already been observed.

In the case where several fields are already available from other JWST surveys, the snapshot rates given by Table 2.3 suggest that a dedicated, long program may not be required to detect dozens of high redshift SNe. Due to the order-of-magnitude difference in the snapshot rate of PISNe vs CCSNe for the different IMF models, more than 10 fields with followup repeated imaging should already help constrain the stellar population responsible for reionization. Cosmic variance will affect the total number of SNe for

small number of fields, but the ratio of PISNe to CCSNe would still be indicative of the IMF. For example, if Pop III (Flat IMF model) and Pop II stars had equal contribution to reionization (which means Pop II stars dominate Pop III stars by roughly 20-to-1 in total mass), one could use 20 images conducted for other programs as references and only revisit the same image twice for a total of 3 snapshots per field of view. Observing in 4 bands, for a total of 28 days integration time over 2 years, such a survey expects to see ∼10 red supergiant PISNe and ∼300 CCSNe.

To the extent that PISN spectra can be represented as a distribution of blackbodies at different temperatures, since the temperature and redshift would be degenerate, it will be impossible to acquire photometric redshifts without further information about the SN epoch. However, our simulated spectra show significant deviations from a blackbody in the UV ($l < 3500$Å) due to metal-line blanketing in the SN photosphere, providing spectral and photometric signatures that could be used as redshift indicators, depending on their strength.

2.3.7 Luminosity Function

Although the UV flux of PISNe is relatively short lived, the more massive PISNe stay bright in its rest frame visible band for over a year. Given this brightness and long intrinsic duration, coupled with the $(1 + z)$ time dilation at high redshifts, it is conceivable that PISNe could contribute to the luminosity function of all objects at high redshifts when galaxies were dim. Figure 2.10 illustrates the luminosity function of PISNe at ∼4000Å, calculated using the helium core progenitor models for PISN luminosity, and the Pop III Flat or Pop III Salpeter models for the star formation rate. Shown

for comparison are the projected galaxy luminosity functions at high redshifts, using the Bouwens et al. (2011c) best fit Schechter parameterization for the UV luminosity function, and shifting to the visible band using $U - V \approx 0.4$, 0.3 for $z = 7$, 8 respectively, measured using the Spitzer Infrared Array Camera (Labbé et al. 2010a,b). Applying this U-V shift is a crude approximation, as luminous and faint galaxies have different rest frame UV-to-optical color; however, we are most interested in the bright end of the luminosity function, where this current U-V measurement is applicable.

The luminosity function for PISNe implied by our Pop III IMF models overlaps with the galaxy luminosity function at the brightest magnitudes. If a top-heavy Pop III IMF was solely responsible for reionization, PISNe will contaminate the brightest end of the galaxy luminosity function, unless great care is taken to remove these supernovae. Since the volumetric count of the brightest galaxies and PISNe is very low, it will take a wide infrared survey to observe this effect.

2.4 Discussion

In our discussion we ignored complicating factors such as metallicity and rotation, and calculated the PISN and CCSN event rate using only the SN progenitor mass range along with the star formation rate. However, at low redshifts $z < 1$, the measured CCSN rate is a factor of ~ 2 smaller than that predicted by the analogous calculation using the measured cosmic star formation rate. The discrepancy is likely due to many intrinsically low-luminosity or obscured SNe being missed in surveys (Horiuchi et al. 2011). As this discrepancy is lower than the uncertainty in our SFR model parameters, and we already account for lower intrinsic luminosities for the lower progenitor mass PISNe, we do not

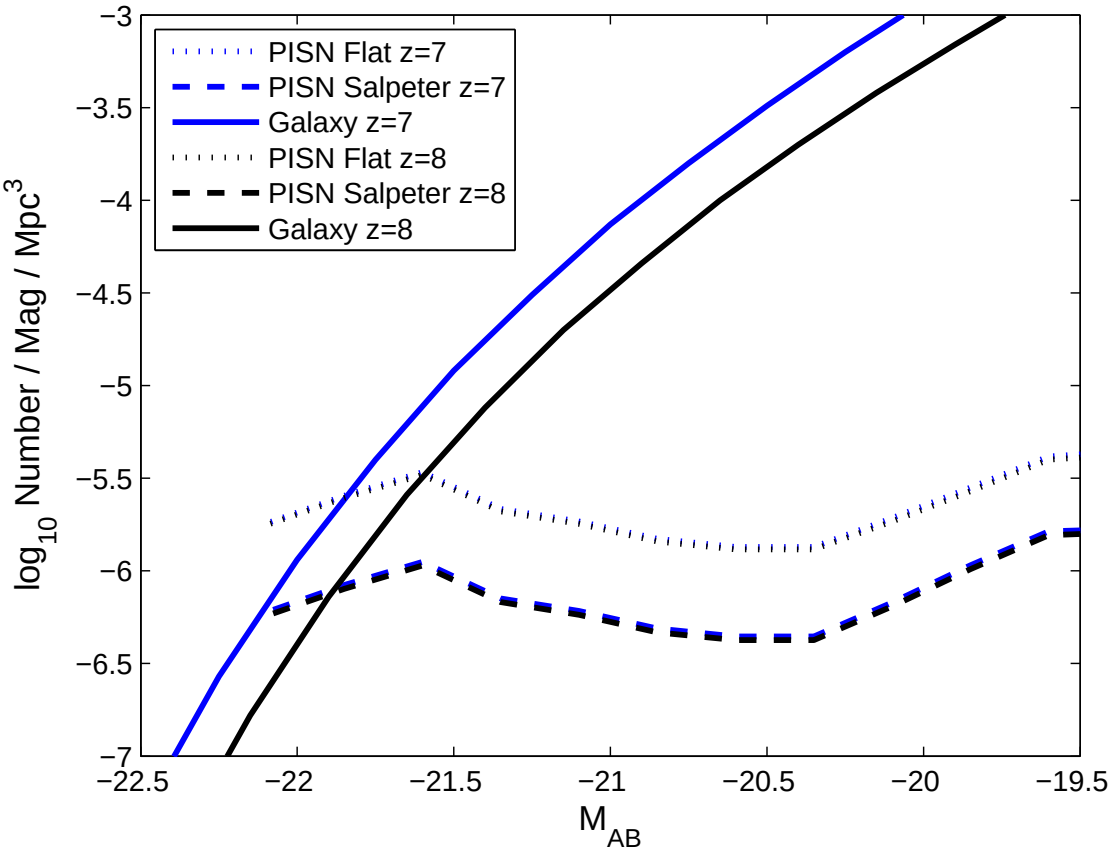

Figure 2.10.— Luminosity functions of PISNe at 4000Åfor $z = 7$ and 8, for the Pop III Flat IMF or Salpeter IMF star formation rate models, compared with the galaxy luminosity function. For the Pop III Flat model, the volumetric count of PISNe exceeds galaxies past $M_{AB} \sim -21.5$; the dominance of PISNe should become greater at higher redshifts, as galaxies decrease in luminosity while PISNe stay the same. The PISN luminosity functions at $z = 7$, 8 overlaps coincidentally because the increase in time dilation compensates for the decrease in PISN event rate.

take obscuration into account for our predictions of the SN rate as seen by JWST.

The IMF of early stellar populations responsible for reionization should also leave an imprint on the metal enrichment pattern via their SN products. So far, the abundance patterns observed to date in extremely metal-deficient stars in the Galactic halo (Beers & Christlieb 2005) are more consistent with an IMF that produced much more CCSNe instead of PISNe (Joggerst et al. 2010). However, in previous surveys, subtle selection effects might have disfavored finding PISN-enriched stars; the metal yields of PISNe are so high that the metal abundances of stars formed out of PISN ejecta (Greif et al. 2008) are already higher than the metallicity range targeted by metal-deficient star surveys (Karlsson et al. 2008).

Large carbon enhancements observed in metal-poor stars, when interpreted as the outcome of pollution by winds from binary companions that have gone through the AGB phase, suggest the existence of a large number of intermediate-mass stars ($\sim 1 - 8 M_{\odot}$) at high redshifts (Tumlinson 2007a,b). Alternatively, nucleosynthesis in faint CCSNe from higher mass stars could also explain the observed carbon enhancement in metal-poor stars (Iwamoto et al. 2005). Observing the Type Ia SN rate during the epoch of reionization will be an complementary way to test these models, and constrain the number of intermediate-mass stars at high redshifts.

The predicted initial mass range of $\sim$140 to 260 $M_{\odot}$ for PISN progenitors assumed the stars to be non-rotating (Heger & Woosley 2002). However, observations find that at very low metallicities, stars rotate faster (Martayan et al. 2007). The fast rotation of the first stars is supported by the latest hydrodynamic simulations of their formation (Stacy et al. 2011), and also by observations of anomalously high abundances of Ba and La with

respect to Fe in ancient low-mass stars (Chiappini et al. 2011), which could originate in metal-poor fast-rotating massive stars. Generally, rotation should increase the required PISN progenitor mass by increasing mass loss. Meynet et al. (2006) found that, contrary to the usual $\dot{M} \propto Z^{0.5}$ scaling relation, rotating stars at very low metallicity $Z \sim 10^{-5}$ to $10^{-8} Z_{\odot}$ show a large mass loss, up to $\sim 50\%$, mainly resulting from efficient mixing of stellar nucleosynthesis products into the stellar surface. However, Ekström et al. (2008) found that for strictly $Z = 0$ stars, the mass loss is very low, even for models that reach critical velocity in the main sequence. These results imply that, for rapidly rotating Pop III stars to die as a PISN, the required progenitor mass is extremely sensitive to whether the star is truly metal-free or not.

At much lower redshifts, PISNe have likely already been observed, most persuasively in the case of the very luminous and long duration event SN 2007bi (Gal-Yam et al. 2009). Other more recent candidates include PTF 10nmn (Gal-Yam in preparation; Yaron et al. in preparation) and PS1-11ap (Rubina Kotak et al. in preparation). As pristine gas was recently observed at redshifts after reionization (Fumagalli et al. 2011), it is possible that some low redshift PISNe have Pop III progenitors born out of surviving pockets of metal-free gas; the rates of PISNe in this scenario was considered by Scannapieco et al. (2005). However, the metallicities of the host galaxies of SN 2007bi and PTF 10nmn are well above the metallicity threshold required to form Pop III stars (Young et al. 2010). Therefore, it is plausible that PISNe can have very massive Pop II/I progenitors as well, perhaps born via the merger of stars in collision runaways in young, dense star clusters (Pan et al. 2012b).

2.5 On the Difficulty of Mapping Reionization History with Type Ia SNe

2.5.1 Constraining the Ionization Fraction

Barring some extreme evolution of the IMF, the neutral fraction of the IGM is expected to rise quickly toward high redshift, with the mean neutral fraction of the IGM expected to reach 6-12% at z=6.5, 13-27% at z=7.7 and 22-38% at z=8.8 (Cen 2010). Currently, the most stringent observational probe on the ionization history of the IGM is the total Thomson optical depth seen by WMAP, $\tau = 0.088 \pm 0.015$ (Komatsu et al. 2011). The Planck mission is projected to reduce the error bars to 0.01. However, τ cannot break degeneracies between different reionization histories; for example, both a rapid, early reionization or an extended, late reionization may have the same total Thomson optical depth. Finding $\tau(z)$ using Type Ia supernovae at high redshifts would break this degeneracy.

We set up a toy model of the global average ionization fraction $X(z)$ using the Fermi-Dirac form for the ionization fraction:

$$X(z) = \frac{1}{e^{\frac{z-z_{re}}{\Delta}} + 1}, \tag{2.10}$$

where z_{re}, Δ are model parameters that characterize the redshift and duration of reionization, respectively. Then for an luminous object at redshift z_{obs}, the Thomson electron scattering optical depth is the integral of $X(z)n_e\sigma_T$, the ionization fraction times the electron density times the Thomson cross section integrated along proper length

(Shull & Venkatesan 2008),

$$\tau(z_{obs}) = \int_0^{z_{obs}} X(z) n_e \sigma_T \frac{c}{(1+z)H(z)} dz \quad (2.11)$$

$$+ \quad \tau_{HeIII} \times \Theta(z_{obs} - z_{HeIII}). \quad (2.12)$$

Here $H(z) = H_0[\Omega_m(1+z)^3 + \Omega_\Lambda]^{1/2}$. The second term with $\tau_{HeIII} \simeq 0.002$, and Θ as the Heaviside step function, comes from the full reionization of HeII to HeIII around $z_{HeIII} \sim 3$ (Shull et al. 2004).

Using this model with hypothesized optical depth measurements, we use Bayesian methods to find the corresponding probability distribution for our reionization history model parameters z_{re}, Δ shown in Figure 2.11. These measurements along with the known optical depth to the CMB can help constrain the duration of reionization Δ.

2.5.2 Survey Feasibility with JWST

Using the Phillips relation (Phillips 1993), we can utilize Type Ia SNe as standard candles by measuring the shape of the light curve. Specifically, to characterize the light curve and find $\Delta m_{15}(B)$, i.e., the decline in the B-magnitude light curve from maximum light to the magnitude 15 days after B-maximum, we should to take a snapshot every 3 days for roughly 20 days (5 days before and 15 days after peak), which at redshift 8 means returning to the same field of view once every month due to time dilation. Note that above $z > 10$, the B band ($\sim$ 4400Å) redshifts out of NIRCam. Also, Brandt et al. (2010) found that the prompt channel Type Ia SNe are more luminous (high-stretch, slow declining), and thus have a lower $\Delta m_{15}(B)$. For NIRCam, we can see up to -18 AB magnitude at redshift ~ 8 with 3×10^4 s integration time ($\sim$ 8 hours), with a signal-to-noise ratio of 5, and fully characterize the SN light curve as long as

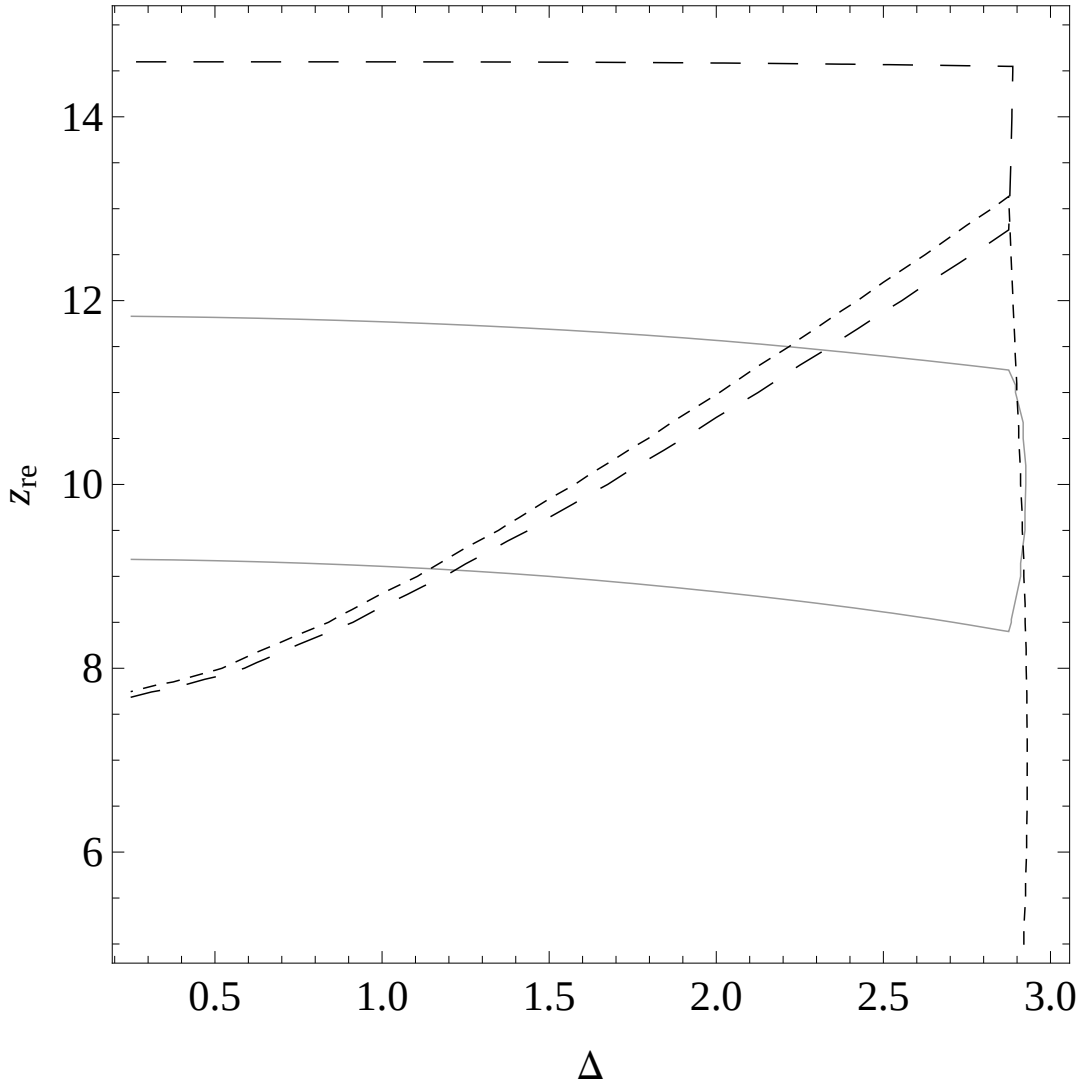

Figure 2.11.— One-sigma (68%) contours of z_{re}, Δ given measurements of $\tau(z_{obs} = 8)$ and CMB total optical depth. Flat priors of $z_{re} = 5 - 15$, $\Delta = 0.25 - 3$ are assumed for the x,y axis, respectively. The straight, long-dashed, and short-dashed line represent the contours from measurements of $\tau_{CMB} = 0.088 \pm 0.015$ (Komatsu et al. 2011), $\tau(z_{obs} = 8) = 0.07 \pm 0.01$, and $\tau(z_{obs} = 8) = 0.04 \pm 0.01$, respectively, the latter two of which are hypothetical values of optical depth we may measure from a large sample of SNe Ia.

$\Delta m_{15}(B) < 1.3$. This is roughly ∼60 hours of total integration time over half a year for each field of view with a Type Ia SN. Unrealistically assuming command of all JWST's time, the light curve of ∼150 Type Ia per year can be fully mapped out.

As seen in Figure 2.9, JWST might see ∼1 Type Ia SNe at $z = 6 - 7$ for every snapshot it takes with NIRCam. To find interesting results about reionization history, one should probe the ionization fraction before the end of reionization, at $z \sim 8$ or above. Here, the SNe are dimmer and the rate is smaller, though by only a factor of ~ 2 each. A bigger obstacle is, at this redshift, many color bands redshift out of NIRCam's range (at $z \sim 8$, only the UBV bands at the SN rest frame are still accessible). Since the calibration of Type Ia SNe magnitudes relies on multiple color bands, it is not clear the often quoted ~ 0.20 standard deviation in distance modulus can be achieved. Moreover, calibrating the intrinsic luminosity of SNe Ia down to $\Delta M \sim 0.20$ is equivalent to a variation in optical depth of $\Delta\tau \sim 0.18$. To get the Thomson optical depth to 1% precision at a fixed redshift bin, required to make meaningful constraints on reionization history, would require over 300 independent Type Ia SNe, or over two full years of JWST's integration time. This is clearly not feasible.

2.6 Conclusions

We analyzed simulated light curves and spectra of pair-instability supernovae for a variety of progenitor masses and envelope types, and found that the supernovae from the more massive progenitors are super-luminous and have extended light curves, traits that would help photometrically distinguish pair-instability supernovae from other types of supernovae using repeated snapshots. We calculated the rates and detectability of

pair-instability, core collapse, and Type Ia supernovae during the redshifts of reionization, and showed that it is possible to constrain the initial mass function of stars at that time, and identify the stellar population responsible for reionization. If Pop III stars made the dominant contribution of ionizing photons during reionization, the bright end of the galaxy luminosity function will be contaminated by pair-instability supernovae.

Acknowledgments

We thank Bob Kirshner, Kaisey Mandel, and Jonathan Pritchard for helpful discussions. TP was supported by the Hertz Foundation. This work was supported in part by NSF grant AST-0907890 and NASA grants NNX08AL43G and NNA09DB30A. This work is supported by the Director, Office of Energy Research, Office of High Energy and Nuclear Physics, Divisions of Nuclear Physics, of the U.S. Department of Energy under Contract No.DE-AC02-05CH11231. This research has been supported by the DOE SciDAC Program (DE-FC02-06ER41438). We are grateful for computer time provided by ORNL through an INCITE award and by NERSC.

Chapter 3

Pair-Instability Supernovae via Collision Runaway in Young Dense Star Clusters

Tony Pan, Abraham Loeb, and Daniel Kasen.

The Monthly Notices of the Royal Astronomical Society, Vol. 423, Issue 3, pp. 2203-2208, 2012.

Abstract

Stars with helium cores between ∼64 and 133 $M_{\odot}$ are theoretically predicted to die as pair-instability supernovae. This requires very massive progenitors, which are theoretically prohibited for Pop II/I stars within the Galactic stellar mass limit due to mass loss via line-driven winds. However, the runaway collision of stars in a dense,

young star cluster could create a merged star with sufficient mass to end its life as a pair-instability supernova, even with enhanced mass loss at non-zero metallicity. We show that the predicted rate from this mechanism is consistent with the inferred volumetric rate of roughly $\sim 2 \times 10^{-9}$ Mpc^{-3} yr^{-1} of the two observed pair-instability supernovae, SN 2007bi and PTF 10nmn, neither of which have metal-free host galaxies. Contrary to prior literature, only pair-instability supernovae at low redshifts $z < 2$ will be observable with the *Large Synoptic Survey Telescope* (LSST). We estimate the telescope will observe $\sim 10^2$ such events per year that originate from the collisional runaway mergers in clusters.

3.1 Introduction

Pair-instability supernovae (PISNe) are thought to occur for stars with helium cores between ∼64 and 133 $M_\odot$ (Heger & Woosley 2002). At zero metallicity, this corresponds to initial stellar masses between ~ 140 and 260 $M_\odot$. These enormous stellar masses may have been reached by Pop III stars, predicted to have a top-heavy mass distribution (Bromm & Larson 2004). However, at lower redshifts, as the universe was enriched, Pop III stars ceased to form once the local metallicity exceeded a critical threshold $Z_{crit} \sim 10^{-3} Z_\odot$ (Bromm & Loeb 2003). Since it is almost impossible to raise the intergalactic medium metallicity in a homogeneous way (Furlanetto & Loeb 2003; Scannapieco et al. 2003), pristine metal-free stars will still be formed past the end of the reionization epoch $z \lesssim 6$ (Trenti et al. 2009), conceivably all the way down to $z = 2.5$ (Tornatore et al. 2007). Observations have confirmed the existence of extremely metal-poor star formation at moderate redshifts of $z = 3.357$ and $z = 5.563$ (Fosbury

et al. 2003; Raiter et al. 2010). The detectability of PISNe from Pop III stars at these moderate redshifts was investigated by Scannapieco et al. (2005).

Outside these surviving pristine regions, there is a wide range of observations that support an upper limit to stellar mass at $\sim 150 M_{\odot}$ in our Galactic neighborhood(Figer 2005; Weidner et al. 2010), preventing the formation of PISNe from Pop II/I stars (but see Crowther et al. (2010) for stars determined to be above $150 M_{\odot}$ in the R136 cluster.) Nevertheless, even if very massive stars can form in metal rich regions, these radiatively supported stars are loosely bound and have strong winds driven mainly by radiation pressure through spectral lines, scaling as $\dot{M} \propto Z^{0.5\sim0.7}$ (Vink et al. 2001; Kudritzki 2002). So even Pop II/I stars with initial masses between ~ 140 and 260 $M_{\odot}$ will suffer copious mass loss during both the hydrogen and helium burning stages, and may not end their lives with enough mass remaining to die as PISNe; this prediction could be contested, as there are still large uncertainties in mass loss models from hot massive stars (Puls et al. 2008). Nevertheless, due to mass loss the possibility of PISNe is usually not considered for solar composition stars, even though the pair instability arises irrespective of the progenitor's metallicity.

Regardless, PISNe have very likely already been observed at low redshifts, most convincingly in the case of the very luminous and long duration event SN 2007bi (Gal-Yam et al. 2009). More recently, the Palomar Transient Factory observed a new presumed PISN, PTF 10nmn (Gal-Yam 2011, submitted; Yaron et al., in preparation), and another PISN candidate was reported by the Pan-STARRS1 survey, PS1-11ap (Kotak et al., in preparation.) Although it may be possible to explain bright events like SN 2007bi with alternative models (e.g. Woosley et al. (2007), Moriya et al. (2010), Kasen & Bildsten (2010)) on the whole the observations seem to favor a scenario in

which a large total mass and radioactive mass were ejected, as in a PISN explosion. The observations therefore suggest that very massive stars above the Galactic limit are formed in the local universe. The metallicities of the host galaxies of both supernovae are low but well above the maximum metallicity required to form Pop III stars (Young et al. 2010). Either pockets of pristine gas survived in the dwarf host galaxy of SN 2007bi and PTF 10nmn, or the initial mass function (IMF) of Pop II/I stars merely steepens at the very high end (instead of a hard upper limit), or there are other exotic ways to form a very massive star.

In theory, mergers of stars can form massive SN progenitors at any metallicity and circumvent the upper mass limit for Pop II/I stars at $\sim 150 M_{\odot}$. The most likely environment for such mergers is a dense, young star cluster undergoing core-collapse, in which a runaway collision product can become massive enough to die as an ultra-luminous supernova. Portegies Zwart & van den Heuvel (2007) first investigated this scenario for a collapsar, and Yungelson et al. (2008); Glebbeek et al. (2009); Vanbeveren et al. (2009) discussed the conditions under which the runaway collision product will end its life as a PISN.

In this paper, we calculate the number of the collision runaway merger products within dense young star clusters that lie in the PISN progenitor mass range, and show that the predicted event rate is roughly equal to the inferred rate of PISNe from the detection of SN 2007bi and PTF 10nmn in existing surveys, without requiring the supernova progenitor to be metal free. We further investigate the observability and rate of these events in the low redshift universe with the *Large Synoptic Survey Telescope* (LSST).

3.2 Rates from Runaway Collisions

An appreciable fraction of stars are born in clusters; Bastian (2008) found the fraction of mass that forms in clusters $> 100M_\odot$ out of the total star formation rate to be $\Gamma \sim 8 \pm 3\%$. As soon as the cluster forms, the massive stars start to sink to the cluster center due to dynamic friction, driving the cluster into a state of core collapse on a timescale of $t_{cc} \sim 0.2 t_{rh}$, where t_{rh} is the relaxation time:

$$\begin{aligned} t_{rh} &\approx 2\mathrm{Myr} \left(\frac{r}{1\mathrm{pc}}\right)^{\frac{3}{2}} \left(\frac{m}{1M_\odot}\right)^{-\frac{1}{2}} \frac{N}{\log\lambda} \\ &\approx 200\mathrm{Myr} \left(\frac{r}{1\mathrm{pc}}\right)^{\frac{3}{2}} \left(\frac{m}{10^6 M_\odot}\right)^{\frac{1}{2}} \frac{\langle m\rangle}{M_\odot}. \end{aligned} \tag{3.1}$$

Here m is the cluster mass, r is its half mass radius, N is the number of stars, $\langle m\rangle = N/m \approx 0.5 M_\odot$ is the average stellar mass, and $\log\lambda \approx \log(0.1N) \sim 10$ (Portegies Zwart et al. 2010). In sufficiently compact clusters, the formation of a dense central subsystem of massive stars may lead to a collision runaway, where multiple stellar mergers result in the formation of an unusually massive object (Gürkan et al. 2004; Freitag et al. 2006). This prescription is often invoked to form intermediate-mass black holes via the photodisintegration instability that collapses a super-massive star directly into a black hole.

For a successful collision runaway to occur, the star cluster must experience core collapse before the most massive stars explode as a SN ($\sim$3 Myr). For compact clusters ($t_{rh} \lesssim 100$ Myr), basically all massive stars sink to the cluster core during the runaway, and the final merged object's mass scales with the cluster mass, $m_r \approx 8 \times 10^{-4} m \log\lambda$ (Portegies Zwart & McMillan 2002). For clusters with longer relaxation times, only a portion of massive stars sink to the core in time and the merged object's mass scales

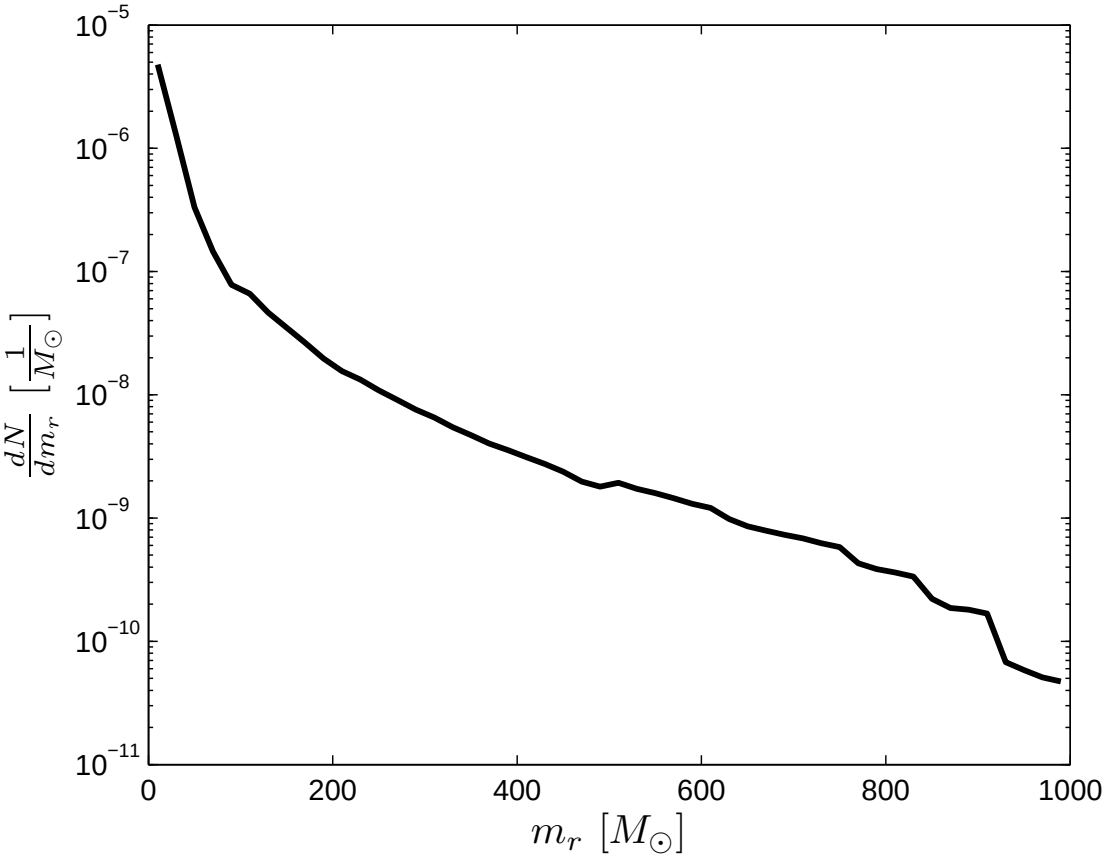

Figure 3.1.— Differential number distribution of the final runaway mass formed, *per* $1M_\odot$ *of stellar mass formed in all clusters*. The calculated distribution is not perfectly smooth owing to the finite number of samples in the observed radius distribution.

as $mt_{rh}^{-1/2}$ (McMillan & Portegies Zwart 2004). A fitting formula for combining these scalings is given by Portegies Zwart et al. (2006), calibrated by N-body simulations for Salpeter-like mass functions:

$$m_r \sim 0.01m(1 + \frac{t_{rh}}{100\mathrm{Myr}})^{-\frac{1}{2}}. \tag{3.2}$$

To get statistics on the final runaway mass m_r from equations (3.1) & (3.2), we need to specify the number distribution of clusters as a function of their mass m and radius r.

The functional form of the cluster initial mass function is well represented by a Schechter (1976) distribution,

$$\Phi(m) = \frac{dN}{dm} = Am^{-\beta}e^{-m/m_*}, \tag{3.3}$$

where observationally $\beta \sim 2$ (Zhang & Fall 1999; McCrady & Graham 2007). For Milky Way-type spiral galaxies the break mass $m_* \approx 2 \times 10^5 M_\odot$ (Gieles et al. 2006; Larsen 2009), whereas for interacting galaxies and luminous IR galaxies $m_* \gtrsim 10^6 M_\odot$ (Bastian 2008). Our results are not sensitive to the choice of m_*.

Several studies have discussed the lack of any clear correlation between the size of a cluster and its mass or luminosity (Larsen 2004; Scheepmaker et al. 2007). Lacking a functional distribution of cluster radii, we use the empirical distribution of radii for each cluster mass bin, for observed clusters younger than 5 Myr, compiled in Tables 2-4 of Portegies Zwart et al. (2010). The restriction on cluster age is important, as clusters expand considerably during the first 10 Myr of their evolution. Note that this empirical construction underestimates the number of super-massive collision runaway objects ($> 10^3 M_\odot$), as there happens to be no observed $> 10^6 M_\odot$ clusters younger than 5 Myr in the current sample, but this does not drastically affect our PISN rate estimates. With

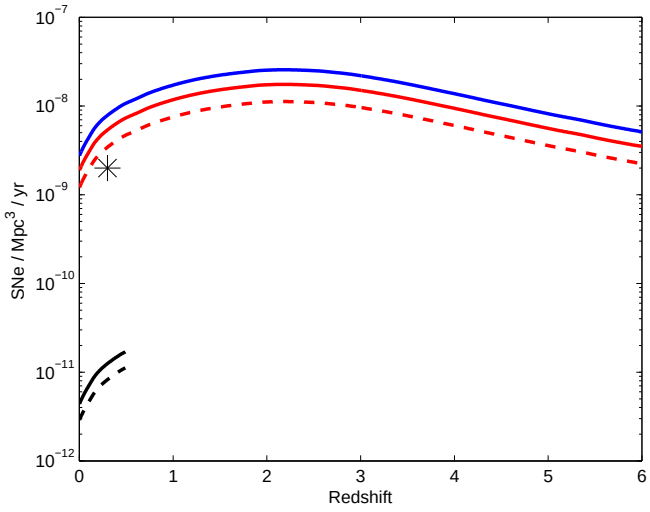

Figure 3.2.— Predicted rate of PISN events per comoving Mpc^3 per year. The pair-instability SNe progenitor mass range is a major uncertainty for non-pristine stars. Here we use 140-260 $M_\odot$ (blue line) for metal-free Pop III stars from the models of Heger & Woosley (2002), whereas the mass range of ∼250-800 $M_\odot$ (red line) is taken from Yungelson et al. (2008), who account for increased mass loss at solar metallicity. The environments of low redshift PISNe will likely lie in between these two cases. A stronger mass loss scenario is presented by Belkus et al. (2007), who found that PISNe progenitors can only be created at metallicities below 0.02 $Z_\odot$, with a mass range ∼300-1000 $M_\odot$ (black line); as the fraction of matter in $Z < 0.02\ Z_\odot$ galaxies is not well constrained past low redshifts, we do not plot this rate past $z = 0.5$. The strongest mass loss scenarios presented by Glebbeek et al. (2009) and Vanbeveren et al. (2009) predict a PISNe rate of practically zero, so we do not plot it here. The dashed lines are the PISNe rates of Yungelson et al. (2008) and Belkus et al. (2007) adjusted for mass loss from stellar collisions. The black star shows the inferred PISN rate from current surveys.

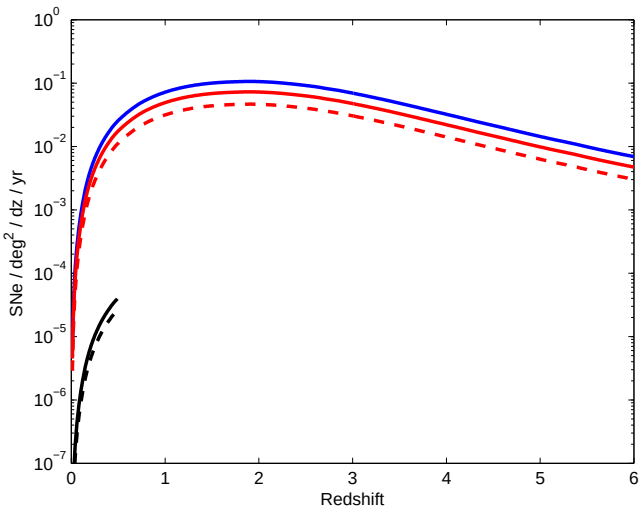

Figure 3.3.— Number of new PISNe per deg^2 per unit redshift per year, for the same models as Figure 3.2. Note that LSST is expected to cover over 20,000 deg^2 of sky.

the joint number distribution of clusters as a function of their mass and radii, we can find the number distribution of the final mass of the runaway collision merged object, see Figure 3.1.

However, as we have not taken mass loss into account in our estimate of the final runaway mass in equation (3.2), we artificially inflate the mass range for PISN progenitors required at the end of the last merger event, to compensate for the mass lost during the collision runaway merger sequence. For zero-metallicity Pop III stars, mass loss via line-driven winds should be negligible, and Heger & Woosley (2002) found the progenitor mass range to be 140-260 $M_{\odot}$; this should set the upper limit of the PISNe rate from runaway collision products.

As for Pop II/I PISNe progenitors, we caution that mass loss via stellar winds for massive stars $M > 100M_{\odot}$ is not well understood. In fact, the observations of PISNe at

low redshifts (Gal-Yam et al. 2009), and of Type IIn SNe whose progenitors are found to sometimes retain their hydrogen envelopes until shortly before their explosion (Smith et al. 2011b), suggest that most commonly-used stellar mass loss models are inaccurate for very massive stars, and likely overestimate the total mass loss, as the models do not allow such SNe to exist at the measured metallicities. Therefore, to account for this uncertainty, we present here various PISN progenitor mass range scenarios described in literature, dependent on the assumed metallicity and mass loss prescription.

Yungelson et al. (2008) studied the evolution and fate of super-massive stars with solar metallicity from the zero-age main sequence using detailed stellar structure models. However, instead of extrapolating commonly used mass loss models, e.g. de Jager et al. (1988); Vink et al. (2001); Kudritzki (2002), Yungelson et al. (2008) used an ad-hoc mass-loss prescription consistent with existing models in their relevant regimes and more consistent with the observed Hertzsprung-Russell diagram location and mass loss ranges found for young massive stars in clusters in the Milky Way and the Magellanic Clouds. Notably, their time-averaged Wolf-Rayet (WR) mass loss rate $\dot{M}_{WR}$ hardly exceeds 10^{-4} $M_{\odot}$ yr^{-1}, which better fits observations of hydrogen-rich WR stars that account for iron-line blanketing and clumping in determining $\dot{M}_{WR}$ (Hamann et al. 2006), and also agrees well with $\dot{M}_{WR}$ estimates based on radio observations (Cappa et al. 2004). On the contrary, the extrapolation of Wolf-Rayet mass loss formulas to high stellar masses given by Langer (1989), Nugis & Lamers (2000), Nelemans & van den Heuvel (2001), and De Donder & Vanbeveren (2003) overestimate the mass loss rates compared with these observations. Therefore, we use the results of Yungelson et al. (2008) as our fiducial model. They allow the creation of PISNe progenitors at $Z \sim Z_{\odot}$ in the initial mass range of ∼250-800 $M_{\odot}$; however, they do not account for the mass loss from stellar collisions.

Alternatively, by extrapolating theoretical mass-loss rates for radiation-driven wind, Belkus et al. (2007) found that when the metallicity Z is between 0.001 and 0.02 $Z_{\odot}$, one may expect PISN candidates for stars with masses from ∼300-1000 $M_{\odot}$; however, at $Z > 0.02\ Z_{\odot}$ no PISNe are expected. Using the observed galaxy luminosity-metallicity relationship (Kirby et al. 2008; Guseva et al. 2009) and the galaxy luminosity function at low redshifts $z \sim 0.1$ (Blanton et al. 2003), we find that $\sim 0.3\%$ of stellar mass is formed in $Z \lesssim 0.02\ Z_{\odot}$ galaxies, and fold this factor into the predicted PISNe rate for this scenario.

In addition, Glebbeek et al. (2009) follows the evolution of the collision product for a few merger sequences for a $m \sim 5 \times 10^5 M_{\odot}$ cluster, including mass loss along the course of the collision sequence by using the prescription of Vink et al. (2001), and found that above $Z = 0.001\ Z_{\odot}$, the collision runaway product cannot die with sufficient mass to undergo a PISN. The main sequence stellar wind mass loss rate between this work and Yungelson et al. (2008) are similar, however, Glebbeek et al. (2009) also calculates the mass loss from stellar collisions to be roughly $\sim 20\%$ of the total merger product mass before mass loss. Nevertheless, the main source of discrepancy between their conclusions is due to their very different Wolf-Rayet mass loss rates. Glebbeek et al. (2009) implements a strong Wolf-Rayet mass loss rate from Nugis & Lamers (2000) (up to $3.6 \times 10^{-3}\ M_{\odot}\ \mathrm{yr}^{-1}$ at $Z = 0.02$), bringing the collision product down to only $m_r \sim 10 M_{\odot}$ by the end of core helium-burning. Using a comparable mass loss rate, Vanbeveren et al. (2009) reaches the same conclusion that PISNe cannot occur above $Z = 0.001\ Z_{\odot}$. Note that with these mass loss rates, essentially no star in the low redshift universe below M ∼1000 $M_{\odot}$ will end their lives as a PISN, irrespective of the collision runaway mechanism.

To account for the $\sim 20\%$ mass loss due to unbound ejecta from the stellar collision, we can further increase the required PISN progenitor mass range. The new adjusted mass range for PISN progenitors would be ∼313-1000 $M_{\odot}$ in the Yungelson et al. (2008) scenario, and ∼375-1250 $M_{\odot}$ in the Belkus et al. (2007) scenario.

Combining the above, we can estimate the number of collision runaway products that have a final mass m_r in the various PISN progenitor mass range scenarios. Using the global comoving star formation rate from Reddy & Steidel (2009), we estimate the PISN rate as a function of redshift in Figures 3.2 and 3.3. If the collision runaway mechanism is indeed responsible for creating PISNe progenitors at Pop II/I environments in the local universe, we find that only the mass loss prescription described by Yungelson et al. (2008) fits the current rate of PISNe inferred from observation.

3.3 Observability with LSST

The *Large Synoptic Survey Telescope* is a planned wide-field survey telescope that should begin operations at the end of this decade. It has a very wide field of view of 9.6 deg^2, and 6 bands: u, g, r, i, z, and y, covering 320-1080 nm. For the most sensitive bands g, r, and i, a single visit will reach $M_{AB} = 25.0$, 24.7, and 24.0 (5σ) sensitivity, respectively. These bands will be visited 10, 23, and 23 times every year during the 10 years of operation, reaching a coadded depth of M_{AB} =26.3, 26.4, and 25.7 per year by stacking multiple images. Note that for objects much dimmer than ~ 22 mag/arcsec^2, or ~ 25.5 mag/pixel for LSST, the signal will be dominated by the sky background (e.g. airglow and zodiacal light), so in this regime the limiting signal flux needed to reach a fixed signal-to-noise ratio is inversely proportional to the square root of the integration time.

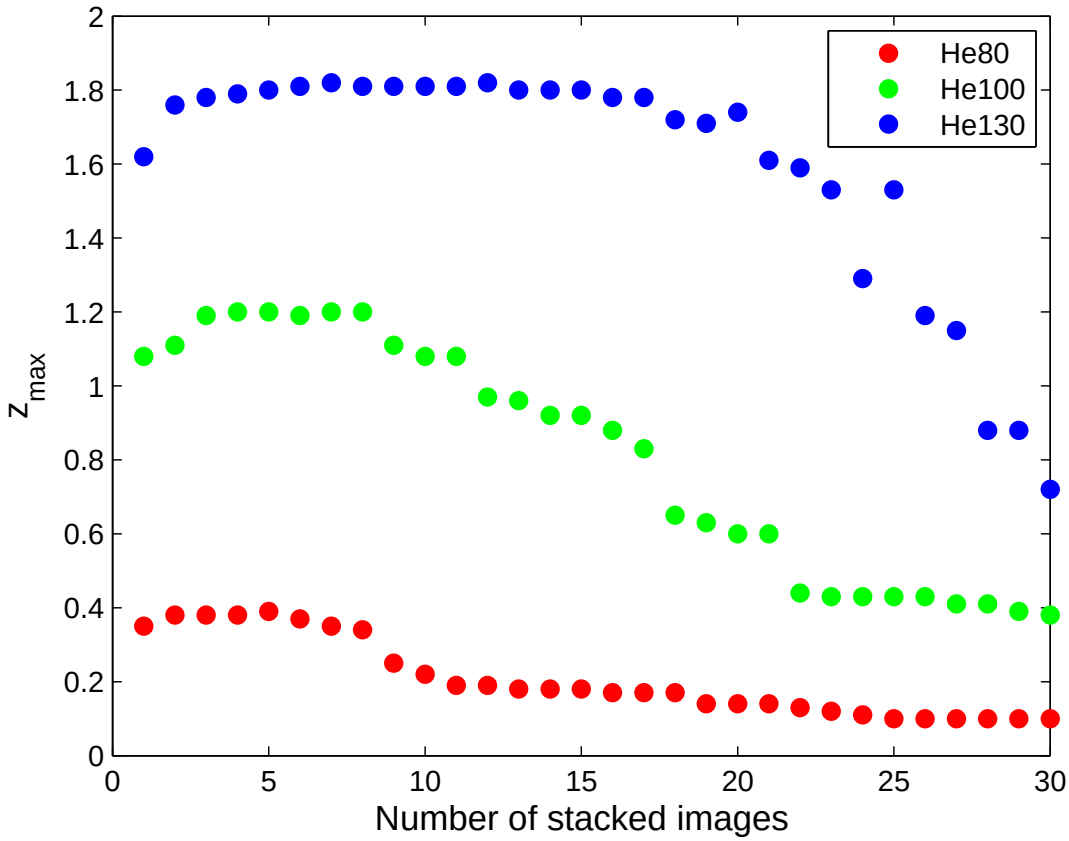

Figure 3.4.— Maximum redshift observable by LSST, as a function of the number of stacked images, for various PISN progenitor models. Here we use the co-added r band 5σ sensitivities, for which LSST will visit the same location 23 times every year, or once every $\sim$ 16 days on average. We consider a PISN at a certain redshift as observable if it stays brighter than the limiting co-added depth for a duration longer than the time it takes to observe that number of images. z_{max} eventually drops with increasing image count, as the PISN flux falls off but the sky background remains, reducing the integrated signal-to-noise. The brightest PISN will be observable with LSST out to a redshift of ~ 1.8.

We use simulated PISN light curves and spectra from Kasen et al. (2011), who improved radiative transfer calculations by using a multi-wavelength Monte Carlo code which includes detailed line opacities. In particular, we use models He130, He100, and He80, which represent pair-instability explosions of non-rotating bare helium cores with masses 130, 100, and 80 $M_{\odot}$, respectively, as non-pristine massive stars formed via runaway collision will likely lose most of their hydrogen envelope by the end of their life. The brightest helium core model He130 peaks at around $M_{AB} \sim -22$ in the rest frame r band, and stays above $M_{AB} = -21$ for half a year, and above $M_{AB} = -20$ for almost one year. Such an event in the local universe will be easily detectable; however, the rates for PISNe from both Pop III and Pop II/I progenitors is predicted to be very low at $z \sim 0$. These rates increase at higher redshifts, but since the higher wavelength z, y LSST bands are much less sensitive, the best strategy to find PISNe is to continue using the g, r, and i bands and observe at the rest frame UV and optical luminosity of the supernovae.

Using the coadded depth sensitivities, we find that using the r band is optimal for the helium core PISN models, and that we can observe the brightest He130 model out to a redshift of $z \sim 1.8$ by stacking ~ 10 images (see Figure 3.4). Below $z < 2$, the PISN is visible in the r band for over 1 year in the observer frame; however, at $z \geq 2$, the supernova will be too dim in the rest frame UV wavelengths being effectively probed, even though the $(1 + z)$ time dilation allows more stacked images. Even if one combines data from the g, r, and i bands over one year, and reaches a coadded depth of $M_{AB} \sim 27$, the supernova will still be too dim to be observable beyond $z = 3$. Alternative PISN models where the progenitors are red supergiants which retain their hydrogen envelopes have a longer plateau in their light curves, and thus stay visible slightly longer than the helium core models. However, the conclusions are similar - in terms of instrument

capability, redshifts $z < 2$ are most suitable for detecting PISNe in the normal operation mode of LSST. The smaller He100 model is only visible out to $z \sim 1.2$, while even smaller progenitors are too dim to be seen beyond $z < 0.4$. Combined with Figure 3.3, we estimate that LSST will see on the order of $\sim 10^2$ new PISNe per year that originated from the final collision runaway object in young, dense clusters.

These conclusions differ from those of Trenti et al. (2009) as well as the LSST Science Book (LSST Science Collaborations et al. 2009), which concluded that PISN at $z \sim 4$ will be within the capability of LSST. The difference arises because Trenti et al. (2009) approximated the PISN with a blackbody spectrum with $T_{eff} = 1.5 \times 10^4$K, which overestimates the rest frame UV flux compared to the spectrum obtained by the radiation hydrodynamics simulations of Kasen et al. (2011). Also, in the LSST Science Book, when calculating that hundreds of $z = 2 - 4$ PISNe will be detected by LSST (Chapter 11.14), the authors used z and y band sensitivies of ~ 26.2. This is unrealistic as $M_{AB} \sim 26.2$ can only be reached in the z band by stacking all images over the entire 10 year lifetime of the survey, but no PISN will stay bright enough that long even with time dilation; the y band is even less sensitive. Our findings suggest that, to find PISNe at $z > 2$, an instrument with better infrared capabilities such as the *James Webb Space Telescope*[1] is required.

Although stacking multiple images averages out the time variation in the supernova light curve, LSST also allows a secondary survey over a smaller area of sky, going substantially deeper in a single epoch. However, due to the steep luminosity function of PISNe, we will preferentially see only the massive PISN events beyond the local universe, so narrow, deep exposures by LSST are more useful for improving light curve coverage,

[1] http://www.jwst.nasa.gov/

instead of supernova discovery.

3.4 Discussion

Runaway collisions were explored most seriously in massive, dense clusters, so equation (3.2) may not be accurate for $m < 10^4 M_\odot$. However, only more massive clusters can make runaway masses m_r in the PISN progenitor mass range, so this does not affect the predicted PISN rate. In addition, initial mass segregation of stars within young clusters observed by de Grijs et al. (2002) and Stolte et al. (2006) will shorten the time to runaway collisions and increase m_r, but we do not take this into account.

For $z \lesssim 6$, the rate and detectability of PISN from Pop III progenitors born in surviving pockets of metal-free gas was investigated by Scannapieco et al. (2005). To model the PISN light curves, they used an implicit hydrodynamics code which only implements gray diffusive radiation transport; for spectra and colors they assumed a blackbody distribution. Depending on the intergalactic medium metal enrichment history, their predicted rates span two orders of magnitude, with their lower end roughly equal to our collision runaway rates at $z = 1 - 2$. However, a PISN with a pristine host galaxy has yet to be observed.

A pilot search done using the *Spitzer*/IRAC dark field found no candidates above the sensitivity limit of $M_{AB}(3.6\mu m) \sim 24$, placing an 95% confidence upper limit of 23 per deg^2 per year for $> 1\mu$Jy sources with plateau timescales less than $400/(1+z)$ (Frost et al. 2009), which does not contradict the predicted rate of < 0.1 PISN per deg^2 per year for our collision runaway model.

More recently, observers have discovered a class of ultra-luminous supernova, with luminosities exceeding those of the brightest pair-instability events, and rates of order $\sim 10^{-8}$ Mpc^{-3} yr^{-1}at $z \approx 0.3$. These events do not appear be standard radioactively powered PISNe, as their luminosities are too high and their light curve durations too short (e.g., Quimby et al. 2011; Chomiuk et al. 2011). Comparing the rate of those events to that of the two putative observed PISNe, Gal-Yam found that PISNe are roughly ∼5 times rarer than the Quimby et al. (2011) ultra-luminous supernovae (Gal-Yam 2011, Science, submitted). This gives a PISN rate of $\sim 2 \times 10^{-9}$ Mpc^{-3} yr^{-1} in the local universe, roughly consistent with the collision runaway rates found in Figure 3.2.

If the collision runaway of massive stars in young, massive stellar clusters do give rise to PISNe at Pop II/I metallicities, we expect to see such a young, massive cluster at the same location, after the light of the supernova has faded away. However, even a $10^5 M_\odot$ cluster only has an absolute magnitude of about -8.2 mag, so the PISN will have to occur close by ($z < 0.05$) for its host cluster to be observed with current telescopes. Also, these PISNe should follow the distribution of clusters, and appear in the luminous parts of their host galaxies, analogous to the position of long duration gamma-ray bursts. Note that due to the steep distribution of collision runaway masses (see Figure 3.1), the rates of PISNe from collision runaways will still be higher in environments with low metallicities, as long as mass loss for massive stars is proportional to metallicity.

Alternatively, if mass loss models are wrong and the Galactic stellar mass limit is violated, we need not invoke stellar mergers to create the massive progenitors required for the observed non-pristine PISNe. Langer et al. (2007) found that hydrogen-rich PISNe could occur at metallicities as high as $Z_\odot/3$, resulting in a rate of about 1 PISN per 10^3 SNe in the $z \approx 0$ universe. For a more conservative metallicity threshold of

$Z_\odot/10$, the rate would be about 1 PISN per 10^4 SNe. However, even the latter is a few times higher than the current inferred rate of PISNe.

3.5 Conclusion

We have shown that the runaway collision and merger of stars in a young, dense star cluster may form the massive progenitor of a pair-instability supernova at non-zero metallicity. The volumetric rate of such events is a few times 10^{-9} Mpc^{-3} yr^{-1} in the local universe, roughly matching the inferred rate of pair-instability supernova events SN 2007bi and PTF 10nmn in ongoing surveys, both of which have a metal-poor but not metal-free host galaxy. We expect that the primary survey of the Large Synoptic Survey Telescope would see $\sim 10^2$ such events per year.

Acknowledgments

We thank Charlie Conroy for helpful comments. TP was supported by the Hertz Foundation. This work was supported in part by NSF grant AST-0907890 and NASA grants NNX08AL43G and NNA09DB30A. DK is supported in part by the Director, Office of Energy Research, Office of High Energy and Nuclear Physics, Divisions of Nuclear Physics, of the U.S. Department of Energy under Contract No. DE-AC02-05CH11231, and by an NSF Astronomy and Astrophysics Grant NSF-AST-1109896. This research has been supported by the DOE SciDAC Program (DE-FC02-06ER41438). We are grateful for computer time provided by ORNL through an INCITE award and by NERSC.

Chapter 4

Identifying Stars of Mass $> 150 M_\odot$ from Their Eclipse by a Binary Companion

Tony Pan, Abraham Loeb.

The Monthly Notices of the Royal Astronomical Society, Vol. 425, Issue 1, pp. L91-L95, 2012.

Abstract

We examine the possibility that very massive stars greatly exceeding the commonly adopted stellar mass limit of $150 M_\odot$ may be present in young star clusters in the local universe. We identify ten candidate clusters, some of which may host stars with masses up to $600 M_\odot$ formed via runaway collisions. We estimate the probabilities of these very

massive stars being in eclipsing binaries to be $\gtrsim 30\%$. Although most of these systems cannot be resolved at present, their transits can be detected at distances of 3 Mpc even under the contamination of the background cluster light, due to the large associated luminosities $\sim 10^7 L_\odot$ and mean transit depths of $\sim 10^6 L_\odot$. Discovery of very massive eclipsing binaries would flag possible progenitors of pair-instability supernovae and intermediate-mass black holes.

4.1 Introduction

Many observations support the statistical argument that the upper limit to initial stellar masses is $\sim 150 M_\odot$ for Pop II/I stars (Figer 2005; Zinnecker & Yorke 2007). However, this common notion is challenged by the recent spectroscopic analyses of Crowther et al. (2010), in which star clusters NGC 3603 and R136 are found to host several stars with initial masses above this limit, including one star R136a1 with a current mass of $\sim 265 M_\odot$. Also, candidate pair-instability supernovae, which require progenitors with masses above $200 M_\odot$, have been observed in the low redshift universe (Gal-Yam et al. 2009). Therefore, it is worth exploring methods to confirm the existence of a very massive star (VMS), defined here as a star with a stellar mass significantly greater than the stellar mass limit, i.e. $M \gtrsim 200 M_\odot$.

Unless the VMS is very close by, it is extremely difficult to spatially resolve the VMS from stars in its vicinity. Indeed, the central component of R136 was once thought to be an extremely massive $\gtrsim 10^3 M_\odot$ star (Cassinelli et al. 1981), before Weigelt & Baier (1985) resolved it as a dense star cluster via speckle interferometry. As for spectroscopic measurements, verification of a single VMS is further complicated by the fact that

the effective temperature T_{eff} of Pop I stars above $10^2 M_\odot$ depends very weakly on mass, with $\log(T_{eff}/\mathrm{K}) \approx 4.7$–$4.8$ (Bromm et al. 2001) for stars between 10^2–$10^3 M_\odot$. Moreover, a hot evolved star with an initial mass below $10^2 M_\odot$ can nevertheless reach these temperatures in its post main-sequence evolution and mimic a VMS.

The most accurate method of constraining the stellar masses of distant stars is by measuring the radial velocity and light curves of the star in an eclipsing binary (Bonanos 2009; Torres et al. 2010). The light curve provides a wealth of information about the binary, including its orbital period, inclination, eccentricity, as well as the fractional radii and flux ratio of the binary members. The radial velocities found from a double-lined spectroscopic binary further provide the mass ratio of the binary. With the above information, the individual masses of each star in the binary can be calculated via Kepler's third law. Searches for massive eclipsing binaries in star clusters within our own Galaxy are already underway (Koumpia & Bonanos 2011), and techniques have been suggested for binary searches in other galaxies (Bonanos 2012).

In this *Letter*, we estimate the masses and properties of VMSs that may have formed via collision runaways in a number of very young, dense, and massive star clusters in the local universe. We calculate the probability of these VMSs to be in eclipsing binaries, and find their expected transit depths and observability.

4.2 Very Massive Stars

Shortly after a dense star cluster forms, its most massive constituents sink to the center via dynamic friction and form a central subsystem of massive stars. In sufficiently dense

environments, these massive stars may undergo runaway collisions and merge into a single VMS (Gürkan et al. 2004; Freitag et al. 2006), possibly up to $\sim 10^3 M_\odot$. Portegies Zwart et al. (2006) gives a fitting formula for the stellar mass m_r of the final runaway product, calibrated by N-body simulations for Salpeter-like mass functions:

$$m_r \sim 0.01\ M_C \left(1 + \frac{t_{rh}}{100\mathrm{Myr}}\right)^{-\frac{1}{2}}, \tag{4.1}$$

where t_{rh} is the relaxation time,

$$t_{rh} \approx 200\ \mathrm{Myr} \left(\frac{r_{vir}}{1\mathrm{pc}}\right)^{\frac{3}{2}} \left(\frac{M_C}{10^6 M_\odot}\right)^{\frac{1}{2}} \frac{\langle m \rangle}{M_\odot}. \tag{4.2}$$

Here M_C is the cluster mass, r_{vir} is its virial radius, and $\langle m \rangle \approx 0.5 M_\odot$ is the average stellar mass.

Using the compilation of stars clusters in the local universe and their properties from Portegies Zwart et al. (2010), we have listed in Table 4.1 several young, dense star clusters that may host a runaway collision product of mass $\gtrsim 200 M_\odot$ which may have not yet ended its life as a star. We restrict our sample to clusters with mean determined ages younger than 3.5 Myr. This may already be insufficiently selective, as stars born with masses $\gtrsim 200 M_\odot$ are expected to have lifetimes of only 2-3 Myr (Yungelson et al. 2008); however, in the runaway collision scenario, the VMS builds up its extraordinary mass via mergers over $\sim 1 - 2$ Myr, and therefore its host cluster may have an age exceeding the 2-3 Myr limit. Of course, these observed cluster properties should not be taken as certain; for example, Úbeda et al. (2007) find the ages of NGC 4214 I-A and I-B to be $\sim$ 4–5 Myr, likely too old for a VMS to be present. Conversely, there may be candidate clusters with VMSs that we have missed. The predicted runaway masses are only approximate, but give a sense of the mass range of VMSs that may lurk at the center of these very young and dense clusters.

Alternatively, if feedback effects are moderate, it may be possible for a protostar to grow without a fixed mass limit via mergers or via the accretion of extremely dense gas. In this case, the mass of the most massive star m_u formed in a molecular cloud scales with the mass of that cloud, and thus will be correlated with the mass of its eventual host cluster (Larson 1982, 2003; Weidner et al. 2010):

$$m_u \approx 1.2\, {M_C}^{0.45}. \tag{4.3}$$

If the above relationship is valid for cluster masses $> 5 \times 10^4 M_\odot$, VMSs will not be restricted to dense clusters, since a collision runaway is no longer necessary for achieving masses $\gtrsim 150 M_\odot$ (see Table 4.1).

4.3 Eclipse Probability

The fraction of massive O-type stars in binaries f_b is observed to be extremely high $> 70\%$ (Chini et al. 2012), and approaches 100% in some environments (Mason et al. 2009; Bosch et al. 2009). Although there is no related observational data on VMSs, numerical simulations indicate that the collision runaway product in young, dense star clusters is generally accompanied by a companion star (Portegies Zwart, private communication).

As the period distribution for our hypothetical VMS binaries is unknown, we assume their periods share the same cumulative distribution function (CDF) as the periods of massive binaries determined from observations. The CDF of the orbital period (p, in days) for massive binaries follows a 'broken' Öpik law, i.e. a bi-uniform distribution in $\log p$, with the break at $p = 10$ (Sana & Evans 2011). There is an overabundance of

Table 4.1: Possible very massive stars in star clusters and their eclipse probabilities. The predicted runaway collision product mass m_r is calculated from equation (4.1). Another possible VMS mass m_u is found via equation (4.3). All masses are in units of $M_\odot$, the cluster age is measured in Myr, and the virial radius r_{vir} is in units of pc. If we optimistically choose the largest mass of m_r and m_u for the primary mass M_1, we can calculate its luminosity L_1 (in $L_\odot$) and radius R_1 (in $R_\odot$) using the models of Bromm et al. (2001), assuming a characteristic stellar metallicity $(Z/Z_\odot) = 0.3$. We calculate the eclipsing probability P_e assuming that the companion is a B0 star, although the result is weakly sensitive to the companion mass. For generality, the expected transit depth $\langle\delta\rangle$ is averaged over a uniform distribution in the binary mass ratio q, up to a companion mass of $10^2 M_\odot$, assuming non-grazing orbits, i.e. $\delta \approx (R_2/R_1)^2$. For all VMS candidates below, the expected dip in luminosity from the eclipse is $\sim 10^6 L_\odot$.

Galaxy	Name	Ref	Age	$\log M_C$	r_{vir}	m_r	m_u	L_1	R_1	P_e	$\langle\delta\rangle$
Milky Way	Arches	1	2.0	4.30	0.68	**192**	103	5e6	44	39%	16%
LMC	R136	2,3,4	3.0	4.78	2.89	**406**	170	1e7	61	36%	8%
SMC	NGC 346	5	3.0	5.60	15.28	**640**	397	2e7	76	34%	5%
M33	NGC 604	6	3.5	5.00	48.21	97	**213**	6e6	46	38%	15%
NGC 1569	C	6	3.0	5.16	4.50	**672**	252	2e7	77	34%	5%
NGC 4214	I-A	6	3.5	5.44	28.69	**305**	337	1e7	56	36%	10%
NGC 4214	I-B	6	3.5	5.40	9.85	**619**	323	2e7	74	34%	6%
NGC 4214	II-C	6	2.0	4.86	23.43	129	**185**	5e6	43	39%	17%
NGC 4449	N-2	6	3.0	5.00	3.57	**565**	213	2e7	71	35%	6%
NGC 5253	IV	6	3.5	4.72	5.26	**271**	160	8e6	51	37%	12%

(1) Figer et al. (1999); (2) Hunter et al. (1995); (3) Mackey & Gilmore (2003); (4) Andersen et al. (2009); (5) Sabbi et al. (2008); (6) Maíz-Apellániz (2001).

short period binaries, with 50% to 60% of binaries having periods less than 10 days. The corresponding probability distribution function $PDF(p)$ of the orbital period is:

$$PDF(p) = \frac{1}{\ln 10} \times \begin{cases} \frac{5}{7p}, & \text{for } 10^{0.3} \leq p \leq 10 \\ \\ \frac{1}{5p}, & \text{for } 10 < p \leq 10^{3.5} \end{cases},$$

with the normalization $\int PDF(p)dp = 1$.

By integrating over uniformly distributed inclinations, it is easy to show that the eclipsing probability of a binary system at any depth is $P_e(a) = \frac{R_t}{a}$, where $R_t = R_1 + R_2$ is the sum of the radii of both components in the binary, and a is the orbital distance. From Kepler's third law, we can express the eclipsing probability as a function of p instead:

$$P_e(p) = R_t \left(\frac{2\pi}{p}\right)^{\frac{2}{3}} (GM_t)^{-\frac{1}{3}}, \tag{4.4}$$

where $M_t = M_1 + M_2$ is the total system mass. Therefore, integrating over the period distribution, the probability that a massive binary will be an eclipsing binary to an observer on Earth is

$$\begin{aligned} P_e &= \int P_e(p)\, PDF(p)\, dp \\ &\approx 0.053 \left[\frac{R_t}{R_\odot}\right] \left[\frac{M_t}{M_\odot}\right]^{-\frac{1}{3}}. \end{aligned} \tag{4.5}$$

For convenience, we ignore any effects of eccentricity; tidal evolution will rapidly circularize the orbit for binaries with periods below $p = 10$ days, which account for 88% of the above eclipsing systems. Dynamical effects would harden a wide-separation massive binary system in the core of a dense cluster on a timescale much shorter than 1 Myr. Since three-body interactions tend to eject the lightest star, the companion to the VMS will likely be a massive star, though not as massive as the runaway product.

The large radii of VMSs coupled with their high binary fraction (and short period binaries being common), imply significant eclipsing probabilities for VMSs. Using R136a1 as an example of the primary star, with a radius $\sim 35R_{\odot}$, and a secondary Sun-like star, the eclipsing probability is 29%, while for a more massive secondary star more common in the core of a young massive star cluster, e.g. a B0 star of mass $\sim 18M_{\odot}$ and radius $\sim 7R_{\odot}$, the eclipse probability is 34%. Note that the eclipsing binary probability in equation (4.5) is not sensitive to the secondary star parameters, as long as its radius is small relative to the primary.

Assuming a companion B0 star, we list the eclipsing binary probabilities for our candidate VMSs in Table 4.1, calculated from equation (4.5), except that we limit the integration over p to periods corresponding to orbital distances exceeding both the radius of the VMS and the Roche limit for the companion. This restriction reduces P_e, and leads to the larger VMSs having slightly smaller eclipsing probabilities; nevertheless, the eclipsing probabilities for all VMS candidates exceed 1/3.

4.4 Observability of Transit

VMSs have spectacular luminosities in the range of $10^7 L_{\odot}$; for example, R136a1 is observed to have $\sim 8.7 \times 10^6 L_{\odot}$. Even at a distance of 3 Mpc – roughly the distance of the farthest host galaxy in Table 4.1 – a star like R136a1 would still have an apparent bolometric magnitude of 14.8. However, VMSs with $T_{eff} \sim 5 \times 10^4$ K emit primarily in the ultraviolet, requiring bolometric corrections of $BC \sim 4.6$. Still, such a VMS will be within the V-band limiting magnitude of ground-based 1-meter telescopes. For the VMS candidates in Table 4.1, with a hypothetical B0-star companion, the transit

depth exceeds $10^5 L_\odot$ in all cases, which at 3 Mpc is just within the single-visit limiting magnitudes of future synoptic surveys such as Pan-STARRS[1] and the Large Synoptic Survey Telescope[2]. Of course, given the shortlist of host clusters in Table 4.1, one can use deep, targeted observations of the individuals clusters with existing telescopes, instead of uniform field surveys.

However, in massive binaries, the mass ratio between the primary and secondary star $q = M_2/M_1$ is observed to have a flat distribution (Sana & Evans 2011). Unlike the transit probability, the transit depth is very sensitive to the companion star radii, so using a B0 star as the companion may be overly conservative. Since only one VMS is expected to form in the collision runaway scenario, here we assume the distribution of companion star masses is uniform between 1 to 100 $M_\odot$. Using typical mass-radius relationships, we show in Table 4.1 the expected transit depth $\langle\delta\rangle$ integrated over the range of companion star radii. Figure 4.1 illustrates sample light curves for a VMS binary at 3 Mpc with different companion star masses and radii at different inclinations.

For clusters outside the Milky Way and its satellites, it is currently impossible to resolve a VMS from other massive stars in a dense cluster core. Hence, we consider the luminosity of the host cluster as a contaminating third light source to the eclipsing binary light curve. If the VMS is present, it will contribute a significant fraction of the bolometric luminosity of the cluster (at least 10% and exceeding 50% in some cases), and an even larger fraction of the UV flux. The integration time t needed to reach a target

[1]http://pan-starrs.ifa.hawaii.edu/public/

[2]http://www.lsst.org/lsst/

signal-to-noise ratio SNR for detecting a transit can be approximated as:

$$\begin{aligned} t &\approx 6\,\text{seconds} \times \left[\frac{L_C}{10^8\ L_\odot}\right]^{-1} \left[\frac{d}{3\ \text{Mpc}}\right]^2 \\ &\times \left[\frac{f_{band}}{0.2}\right]^{-1} \left[\frac{E_{band}}{10\ \text{eV}}\right] \left[\frac{A}{4\times10^4\ \text{cm}^2}\right]^{-1} \\ &\times \left[\frac{SNR}{10}\right]^2 \left[\frac{f_{VMS}}{0.1}\right]^{-2} \left[\frac{\delta}{10\%}\right]^{-2} \end{aligned} \tag{4.6}$$

where L_C is the bolometric luminosity of the cluster, d is the distance to the cluster, f_{band} is the fraction of total flux that is observed (due to the spectral energy distribution, filter bandpass, CCD response, atmospheric transmission etc.), E_{band} is the characteristic observed photon energy, A is the collecting area of the telescope, f_{VMS} is the fraction of total observed flux from the VMS primary, and again δ is the transit depth.

Note that the Hubble Space Telescope (HST) would collect $\gtrsim 10^4$ UV photons per second from a $10^7 L_\odot$ VMS even at a distance of 3 Mpc, thus detecting a $\delta \sim 10\%$ transit depth at $SNR = 10$ in tens of seconds of integration time. Obscuration by dust along the line-of-sight may reduce the observed UV flux. For V-band observations, a very young $\sim 10^5 M_\odot$ cluster can be as bright as $M_V \approx -12$, while a $300 M_\odot$ VMS will have $M_V \approx -8$, i.e. the VMS will only contribute $f_{VMS} \sim 2.5\%$ of the cluster light in the visible band. Nevertheless, a 2-meter ground-based telescope will need less than an hour of integration time to detect the transit, which is eminently feasible as the transit duration $\tau \sim p(R_1/\pi a) \propto p^{1/3}$ for a VMS eclipsing binary will be > 10 hours for all relevant orbital periods.

Other less massive eclipsing binaries in the host cluster will also contaminate the light curve, but their transit depths will likely be negligible compared to the VMS's luminosity. Non-binary random occultations of the central VMS can replicate a large

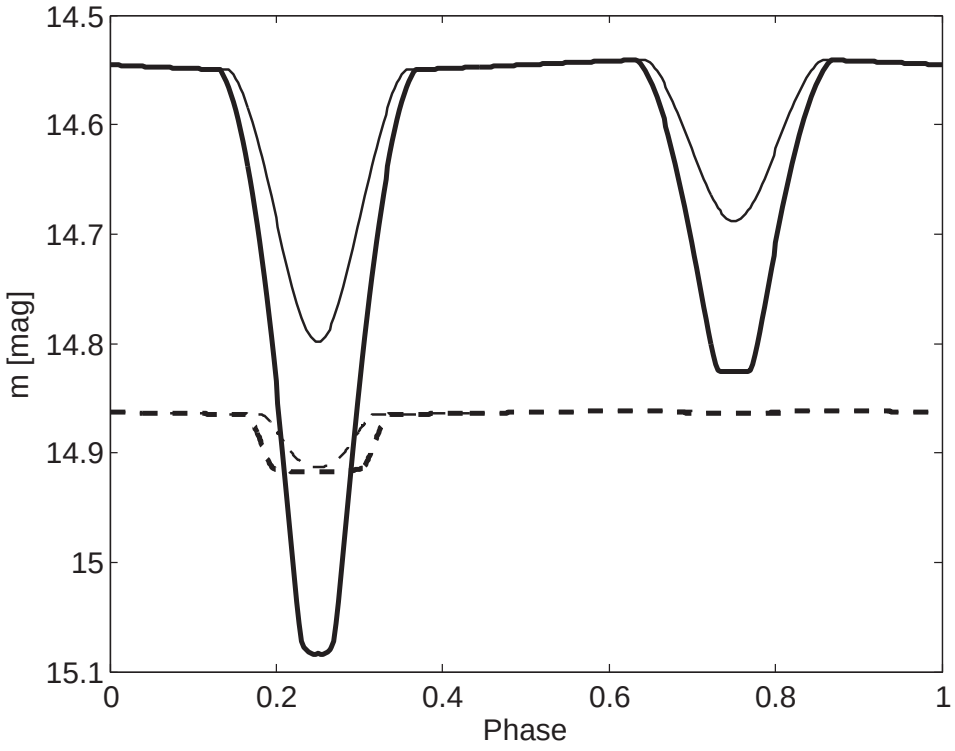

Figure 4.1.— Example light curves for a VMS eclipsing binary. The primary has parameters similar to R136a1, while the secondary is either a $18M_{\odot}$ (dashed line) or $100M_{\odot}$ (straight line) star, with appropriate radii and luminosities. The apparent magnitude m (bolometric) is plotted for these systems at 3 Mpc. The thick and thin lines correspond to inclinations of 90° and 70°, respectively; the period is 5 days in both cases. Reflections and limb-darkening using the model of Diaz-Cordoves et al. (1995) are taken into account, but ellipsoidal variation is ignored.

transit depth, but using a King model for the cluster density profile (King 1966), we find these events occur less than once every 10^6 years.

4.5 Stellar Mass Determination

The extraordinary luminosity of a VMS should allow its radial velocity to be measured. However, the mass ratio q, critical for model-independent determination of the individual masses, can only be found when the radial velocities are determined for *both* components of the binary. Such double-lined spectroscopic binaries are easily observable when the components have similar luminosities, within a factor of 5 of each other (Kallrath & Milone 2009). As the luminosity of massive stars near the Eddington limit scales with mass, this criteria roughly corresponds to $q > 0.2$, which for an uniform distribution in $q \in (0, 1)$ is quite likely to occur.

Nevertheless, if the companion is small, and only spectral lines from the VMS are detected, then the mass ratio q cannot be unambiguously obtained. Instead, the mass of the VMS can be expressed as a single function of q:

$$M_1 = \frac{(1+q)^2}{q^3} \frac{1}{\sin^3 i} f(M_1, M_2, i), \tag{4.7}$$

where $f(M_1, M_2, i)$ is the *mass function*, which can be calculated using quantities derivable from the spectroscopy of a single-lined spectroscopic binary, and the inclination i is derivable from the eclipsing binary light curve. Unfortunately, equation (4.7) varies sharply as $\propto q^{-3}$ for $q \ll 1$. Since q can be as small as ~ 0.01 for VMSs in Table 4.1, crude constraints on the mass ratio, e.g. $q < 0.2$ (when light from the secondary is not observed) cannot establish tight minimum stellar mass constraints on the VMS primary.

However, since a total eclipse $\delta \to 100\%$ is extremely unlikely given the large radii of VMSs, if the mean value $\sim 10^6 L_\odot$ dip in the light curve is in fact observed, it will immediately imply the existence of a star $\gtrsim 10^2 M_\odot$. Hence, although sophisticated light-curve fitting with stellar models would be required, eclipsing single-lined spectroscopic binaries still offer an attractive avenue for inferring the presence of a VMS greatly exceeding the 150 $M_\odot$ stellar mass limit.

4.6 Discussion

A search for periodic flux variations (as shown in Fig. 1) due to transits of the VMS candidates in Table 4.1 would be of considerable interest. Although Crowther et al. (2010) made robust arguments against R136a1 being a wide separation binary or an equal-mass binary, this source could still involve a short-period, unequal-mass binary system. The Arches cluster is observed to have no stars currently above the $150 M_\odot$ mass limit, but Crowther et al. (2010) also found with contemporary stellar and photometric results that the most luminous stars in the Arches cluster had initial masses approaching $200 M_\odot$.

The radii of VMSs are dependent on their metallicities and rotation (Langer et al. 2007). If the VMS radii in Table 4.1 were smaller by $\sim 25\%$ (e.g. at much lower metallicities), all listed eclipsing probabilities would still remain above 1/3, but the expected transit depth would increase up to $\langle \delta \rangle \sim 20\%$. As for the companion star, for most O stars, the point of unity Thomson optical depth occurs close to the hydrostatic radius, but when stellar mass loss exceeds $\sim 10^{-5} M_\odot$ yr^{-1}, the photosphere $\tau \sim 1$ occurs in the wind itself, effectively increasing the star's radius. This occurs for Wolf-Rayet

companions (Lamontagne et al. 1996) and for companions $\gtrsim 60 M_{\odot}$ (Vink et al. 2000), in which case our eclipse probabilities and transit depths are too conservative.

Binaries can be broadly classified into detached systems, where neither component fills its Roche lobe, versus semi-detached or over-contact systems, where at least one component exceeds its Roche lobe. VMSs in detached binaries have much more sharply defined eclipses, and more importantly, they do not undergo mass transfer and lose mass to their companion. To find the probability that our VMS candidates in Table 4.1 are detached eclipsing binaries, we limit the integration in equation (4.5) to periods $p \gtrsim 5$ days, corresponding to orbital distances where the Roche lobe of the VMS is always greater than its radius (Eggleton 1983). For our VMS candidates, the detached eclipsing binary probability is $\approx 17\%$, i.e. roughly half of all eclipsing systems.

However, non-pristine massive stars can also lose mass via strong winds driven by radiation pressure, with a mass loss rate increasing with metallicity. Post main-sequence VMSs can also lose mass eruptively or via pulsational instabilities, although mass loss near the end of the star's life (e.g. the pulsational pair-instability) is not likely to change the observability of our VMS candidates. Under extraordinary mass loss via winds, Glebbeek et al. (2009) found the highest mass attained by a collision runaway product to be $\sim 400 M_{\odot}$, although the star remained at this mass range for only ~ 0.2 Myr. On the contrary, Suzuki et al. (2007) found that stellar mass loss does not inhibit the formation of a VMS of $\sim 10^3 M_{\odot}$. These uncertainties in mass loss may be the weakest point in our arguments for the existence of VMSs in the candidate clusters of Table 4.1.

If VMSs do in fact form via collision runaways in young, dense star clusters, and retain sufficient masses at the end of their lives, they may explode as pair-instability

supernovae (PISNe) (Yungelson et al. 2008). The creation rate of runaway products is in fact consistent with the current observed PISN rate (Pan et al. 2012b). However, the most massive VMSs may collapse directly into an intermediate mass black hole (IMBH) via the photodisintegration instability (Woosley et al. 2002). Tentative evidence has been claimed for IMBHs at the center of old globular clusters (Lou & Wu 2012), and extragalactic ultraluminous x-rays sources associated with young star clusters (Ebisuzaki et al. 2001; Farrell et al. 2009). The identification of VMSs that can serve as the progenitors of PISNe and IMBHs will help move these extreme astrophysical objects from the realm of speculation into reality.

Acknowledgments

We thank Paul Crowther, Dave Latham, Philip Myers, Guillermo Torres, and Simon Portegies Zwart for helpful discussions. We thank Eran Ofek for his eclipsing binary scripts[3], which we built upon to generate our example light curves. TP was supported by the Hertz Foundation. This work was supported in part by NSF grant AST-0907890 and NASA grants NNX08AL43G and NNA09DB30A.

[3]http://wise-obs.tau.ac.il/ eran/matlab.html

Chapter 5

Finding Core Collapse Supernova from the Epoch of Reionization Behind Cluster Lenses

Tony Pan, Abraham Loeb.

arXiv:1303.6960

Submitted to *The Monthly Notices of the Royal Astronomical Society.*

Abstract

Current surveys are underway to utilize gravitational lensing by galaxy clusters with Einstein radii $> 35''$ in the search for the highest redshift galaxies. Associated supernova from the epoch of reionization would have their fluxes boosted above the detection threshold, extending their duration of visibility. We predict that the James Webb Space

Telescope (JWST) will be able to discover lensed core-collapse supernovae at redshifts exceeding $z = 7$–8.

5.1 Introduction

Clusters of galaxies act as gravitational lenses, focusing light-rays from sources behind them and magnifying their images. As this effect enables observers to probe higher redshifts than ever probed before, surveys are being conducted with the Hubble Space Telescope (HST) to obtain deep images of the sky through massive galaxy clusters. One such ongoing program is the Cluster Lensing and Supernova survey (CLASH), which is imaging 25 clusters each to a depth of 20 orbits (Postman et al. 2012). The 5 clusters selected for this program have large Einstein radii of $35''$ to $55''$, maximizing their potential for discovering ultra-high redshift galaxies. Indeed, three candidate galaxies at redshifts $z \approx 9$–10 and another candidate galaxy at $z \approx 11$ have already been found in the CLASH fields (Bouwens et al. 2012; Coe et al. 2013). Similarly, the planned HST Frontier Fields[1] program will target 6 strong lensing galaxy clusters to reveal yet higher redshifts galaxies.

The James Webb Space Telescope (JWST), the successor to HST scheduled for launch in 2018, is likely to have analogous observational programs with comparable integration times on a similar number of lensing clusters. Although the CLASH survey does aim to detect Type Ia supernova (SN) out to redshifts of $z \sim 2.5$, the current HST cluster observations are unlikely to detect gravitationally lensed SN from the epoch of reionization at $z > 6$. Indeed, transient science was not identified as a science

[1] http://www.stsci.edu/hst/campaigns/frontier-fields/

priority for the Frontier Fields program, which will not revisit the same field twice. The greater sensitivity of JWST and its optimization for observations in the infrared could potentially allow it to find lensed supernova from the cosmic dawn in these same cluster fields.

In this *Letter*, we estimate the cosmic star formation rate during the epoch of reionization by requiring that enough Pop II stars were formed to ionize the universe. Using model spectral time series for Type II SN, as well as a simple isothermal sphere model for lensing, we calculate in §2-5 the required magnification and duration of detectability of such SN at $z > 6$ for different JWST bands and integration times. Combining the above, we derive the snapshot rate, i.e. the expected number of gravitationally lensed core collapse SNe detected in the field-of-view of JWST around these high magnification clusters.

5.2 Star Formation & Supernova Rate

We infer the volumetric supernova rate $R_{SN}(z)$ as a function of redshift by relating it to the cosmic star formation rate density (SFRD) $\dot{\rho}_\star(z)$:

$$R_{SN}(z) = \dot{\rho}_\star(z)\eta_{SN} \approx \dot{\rho}_\star(z)\frac{\int_{M_{\rm min}}^{M_{\rm max}} \psi(M)\, dM}{0.7\int_{0.1}^{150} M\, \psi(M)\, dM}, \tag{5.1}$$

where we use a Salpeter initial mass function (IMF), $\psi(M) \propto M^{-2.35}$, and include a factor of 0.7 in the mass integral to account for the shallower slope at $M \lesssim 0.5M_\odot$ in a realistic IMF (Fukugita et al. 1998). For the stellar mass range between $M_{\rm min} = 8M_\odot$ and $M_{\rm max} = 40M_\odot$ appropriate for optically-luminous core-collapse supernova, the conversion coefficient between the star formation rate and the supernova rate is $\eta_{SN} \sim 0.0097M_\odot^{-1}$.

We require that enough massive stars were formed by the end of reionization so as to produce sufficient ionizing UV radiation to ionize the intergalactic medium by $z_{\rm end} = 6$. This follows the approach used in Pan et al. (2012a), albeit with different parameters to bring our estimates closer to other inferences in literature, as detailed below. The star formation rate during reionization peaks at late times, when metals expelled from a prior generation of star formation enriched the interstellar gas, so we assume that early Pop II stars ($Z = 0.02 Z_{\odot}$) with a present-day IMF dominated the ionizing photon budget. Using the stellar ionizing fluxes of Schaerer (2002), we find the average number of ionizing photons produced per baryon incorporated into a Pop II star was $\bar{\eta}_{\gamma} = 5761$. Thus, the mass in stars per comoving volume $\rho_{\star}(z)$ should satisfy

$$\rho_{\star}(z_{end})\, \bar{\eta}_{\gamma}\, f_{esc} = C\, \rho_b, \tag{5.2}$$

where C is the number of ionizing photons necessary to ionize each baryon after accounting for recombinations, ρ_b is the cosmic baryon density, and f_{esc} is the average escape fraction of ionizing photons from their host galaxies into the intergalactic medium. Also, we can relate the mass in stars per volume $\rho_{\star}(z)$ to the mass in virialized halos per volume via a star formation efficiency $f_{\star}$:

$$\rho_{\star}(z) = f_{\star} \frac{\Omega_b}{\Omega_M} \int_{M_{\rm min}}^{\infty} M\, \frac{dn(z)}{dM}\, dM, \tag{5.3}$$

where we use the Sheth-Tormen mass function of halos for dn/dM (Sheth & Tormen 1999), and $M_{\rm min} \sim 10^8 M_{\odot}$ is the minimum halo mass with atomic hydrogen cooling. The cosmological parameters, such as the matter and baryon densities Ω_M, Ω_b, were taken from Planck Collaboration et al. (2013). Assuming $f_{\star}$ is constant, we can calibrate $f_{\star}$ via equations (5.2), (5.3), and then evaluate $\rho_{\star}(z)$ at any redshift. The star formation rate is simply, $d\rho_{\star}(z)/dt$.

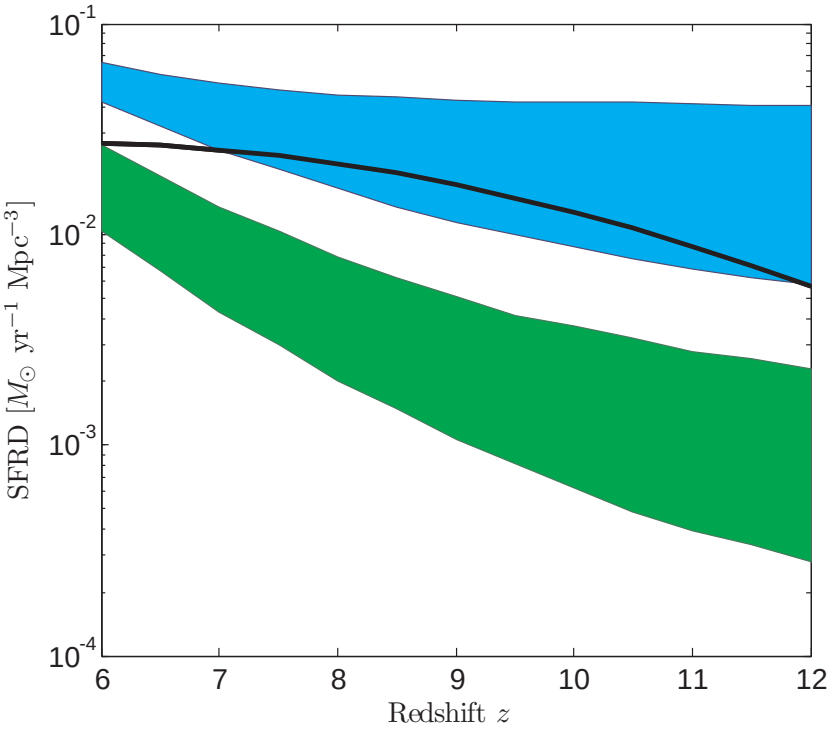

Figure 5.1.— Star formation rate density (SFRD) at high redshift. The black line shows our fiducial SFRD model used in later calculations. For comparison, the blue and green regions are taken from Robertson & Ellis (2012). The blue region (top) spans the high and low values for parametrized star formation histories consistent with GRB-derived star formation rates, whereas the green region (bottom) denotes the SFRD histories derived from UV galaxy luminosity densities observed at high redshift, integrated down to the observation magnitude limit of $M_{AB} \approx -18$. Note that the latter SFRD is likely to be significantly lower than the true cosmic SFRD, as the steep faint-end slope of lower luminosity galaxies (possibly down to $M_{AB} \lesssim -10$) are omitted (Robertson et al. 2013; Ellis et al. 2013), while the GRB-derived SFRD is much less flux limited and likely more accurate. Our SFRD parameters ($C = 3$ and $f_{esc} = 0.2$) were chosen conservatively to be consistent with the low end of the GRB-derived SFRD.

Figure 5.1 shows our estimated SFRD, with $C = 3$ and $f_{esc} = 0.2$, resulting in a SFRD $\approx 2 \times 10^{-2} M_{\odot}$ yr^{-1} Mpc^{-3} (comoving) between redshifts of $z = 6$ to 8. This corresponds to volumetric rates of approximately 2×10^{-4} yr^{-1} Mpc^{-3} for core-collapse supernova. Our simple SFRD model and the resulting SN rates linearly scale with C and f_{esc}^{-1}, so the JWST snapshot rates calculated later can be easily scaled for different parameter choices of the SFRD.

5.3 Light Curves

We adopt the spectral time series of a Type II plateau SN from a red giant progenitor with an initial mass $15 M_{\odot}$, computed by Kasen & Woosley (2009) using a code that solves the full multi-wavelength time-dependent radiative transfer problem. We plot the SN light curves in the observer frame for the best possible HST and JWST filters in Figures 5.2 – 5.4. Note that Type II SN are diverse transients with peak luminosities that can vary by more than an order of magnitude, and the relationship between the progenitor mass and the brightness of the supernova is uncertain; we adopt a single characteristic model to represent all core collapse SNe for the sake of simplicity. Type IIP SNe are the most common events, and the model light curves and spectra used here agree very well with observed SNe of average luminosities.

We verified that HST is incapable in practice of detecting a core-collapse SNe from the epoch of reionization. The sensitivity of the HST 1.6μm filter is only a factor of 2 worse than the JWST F444W filter, but its overwhelming drawback is its waveband, which can only probe the SN rest-frame UV flux at $z \geq 4$. Although the JWST F356W is more sensitive, the F444W band will be optimal for detecting the highest redshift SN

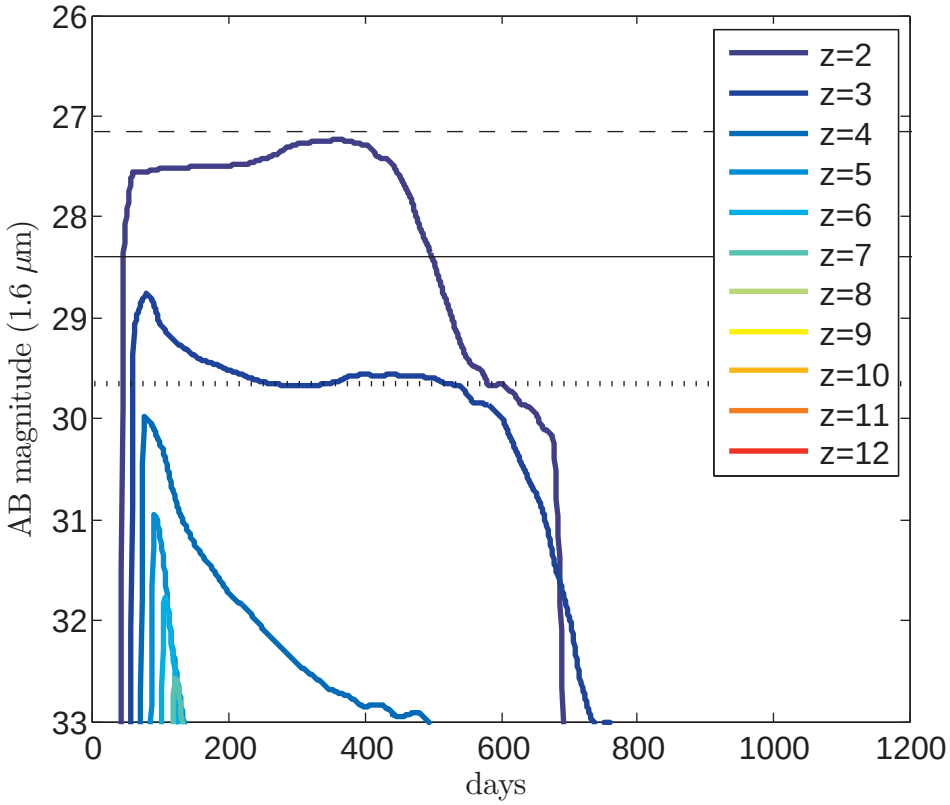

Figure 5.2.— Observer frame light curves for a Type IIP supernova from a $15M_{\odot}$ red giant progenitor, for the HST Wide Field Camera-3 1.6μm filter. The dashed, full, and dotted horizontal lines denote the AB magnitude limits for a 10σ detection with 10^4, 10^5, and 10^6s integration times, respectively. Even a Hubble Deep Field measurement has no hope of seeing a regular Type II SN at $z \geq 6$.

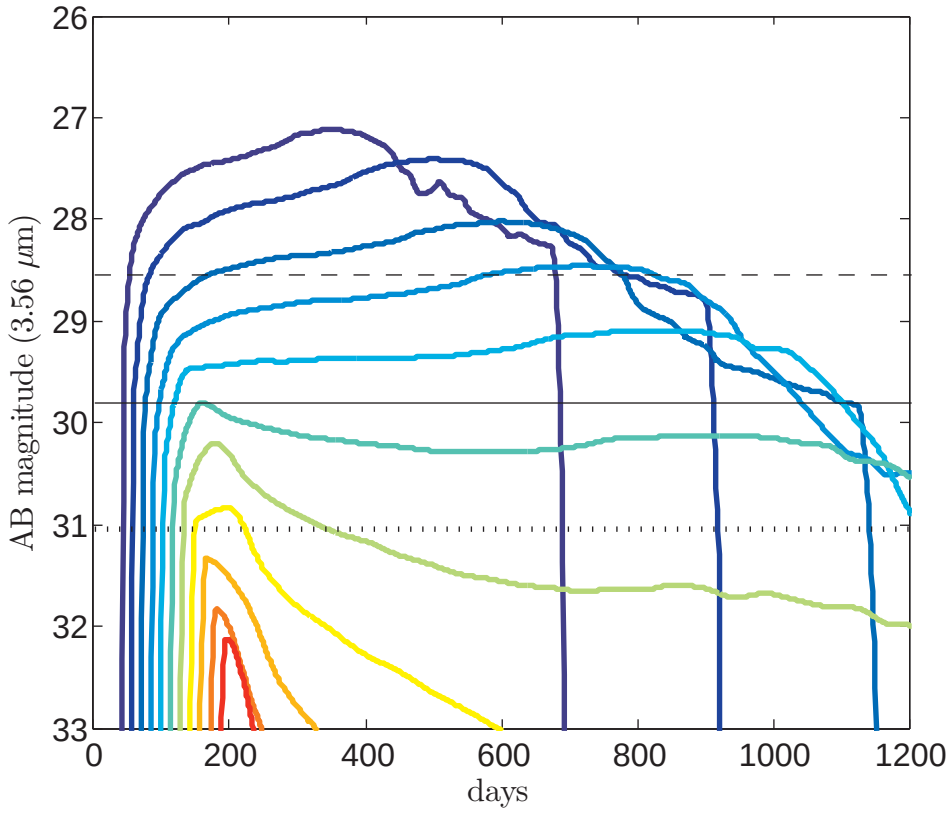

Figure 5.3.— Observer frame light curves for a Type IIP supernova from a $15M_{\odot}$ red giant progenitor, for the JWST Near Infrared Camera (NIRCam) F356W wideband filter at 3.56μm. Note that the HST 1.6μm filter and the JWST F356W and F444W filters have flux limits of 50, 13.8, 24.5 nJy, respectively, for 10^4s exposures.

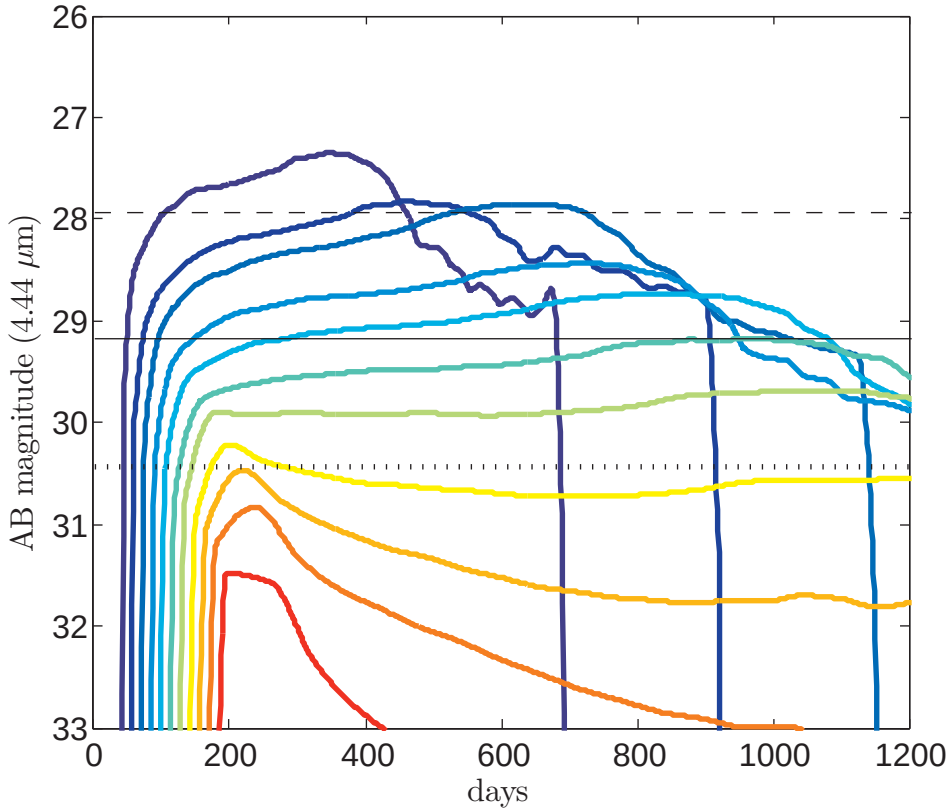

Figure 5.4.— Observer frame light curves for a Type IIP supernova from a $15M_{\odot}$ red giant progenitor, for the JWST Near Infrared Camera (NIRCam) F444W wideband filters at 4.44μm. A 10^5s exposure with JWST can detect a $z = 6$ supernova without magnification. Gravitational lensing would extend its reach to higher redshifts and, more importantly, extend the duration for which the supernova remains above the telescope detection threshold.

that gravitational lensing could provide. Figure 5.5 shows the magnification necessary to detect Type II supernova at high redshifts for different integration times. Even with a 10^5s exposure, a large magnification factor of $\mu \geq 10$ will be necessary for detecting Type IIP SNe at $z > 10$ with JWST.

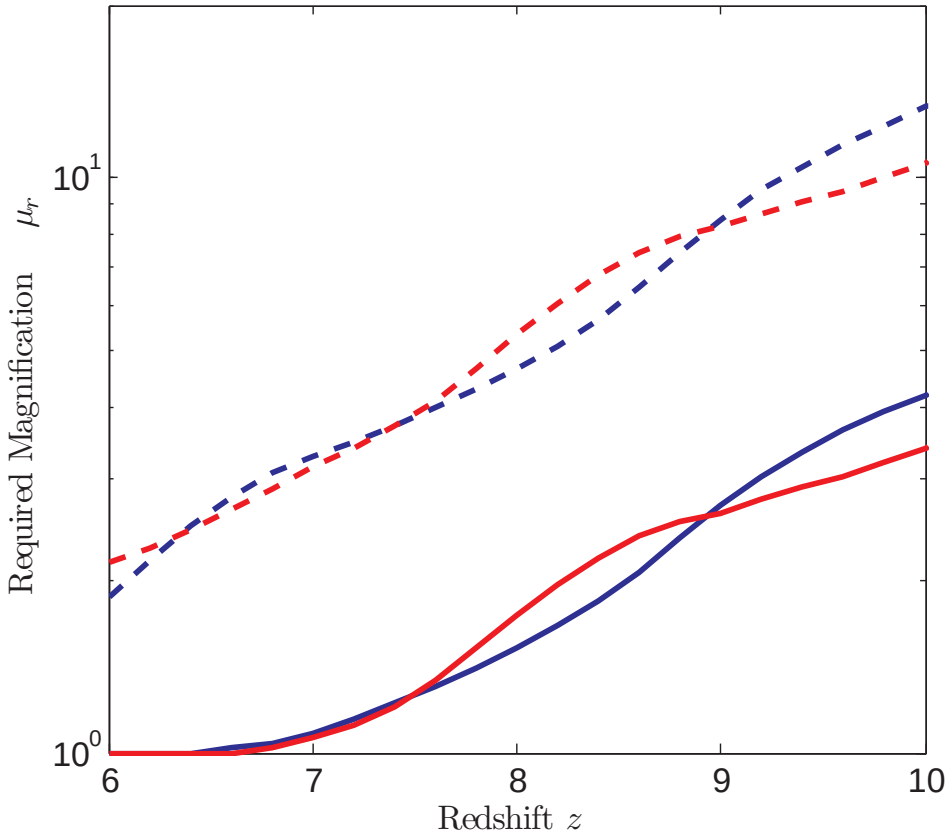

Figure 5.5.— Required magnifications μ_r for detecting Type IIP supernovae with JWST at high redshifts. The blue and red lines denote the results for the F356W and F444W JWST bands, respectively, while the dashed and solid lines correspond to integration times of 10^4s and 10^5s. The latter integration time is similar to that used in CLASH.

5.4 Lensing Magnification

For simplicity, we adopt a *singular isothermal sphere (SIS)* model for the mass distribution of the lensing cluster, within which the magnification properties are uniquely specified by the Einstein radius θ_E (Schneider et al. 1992). We denote the angular separations of the source and the image from the center axis of the lens as β and θ, respectively. If the source lies within the Einstein radius $\beta < \theta_E$, two images are created at locations $\theta_\pm = \beta \pm \theta_E$, with magnifications $\mu_\pm = 1 \pm \theta_E/\beta$. Note that μ_- has negative magnification, that is, the image is flipped compared to the source. If the source lies outside the Einstein radius $\beta > \theta_E$, there is only one image at $\theta = \theta_+$ with magnification $1 < \mu_+ < 2$. We conservatively consider only the higher-magnification image at θ_+, for which the source angle $\beta = \theta_E/(\mu - 1)$.

Then, the differential source volume (comoving) of magnified events as a function of magnification and redshift is:

$$dV(z, \mu) = dA(z, \mu)\, dD_C \tag{5.4}$$

where the differential comoving distance $dD_C(z)$ is

$$dD_C = \frac{c}{H_0} \frac{1}{E(z)} dz, \tag{5.5}$$

with $E(z) \approx \sqrt{\Omega_M (1+z)^3 + \Omega_\Lambda}$, and the differential source area is

$$\begin{aligned} dA(z, \mu) &= (\, 2\pi\, D_A(z) \beta\, D_A(z) d\beta\,)\, (1+z)^2 \\ &= \left(2\pi \frac{\theta_E^2}{(\mu-1)^3} d\mu \right) D_A(z)^2 (1+z)^2. \end{aligned} \tag{5.6}$$

Here $D_A(z)$ is the angular diameter distance, and the extra $(1+z)^2$ is to adjust the area to comoving units. In Figure 5.6, we plot the source volume for a range of Einstein

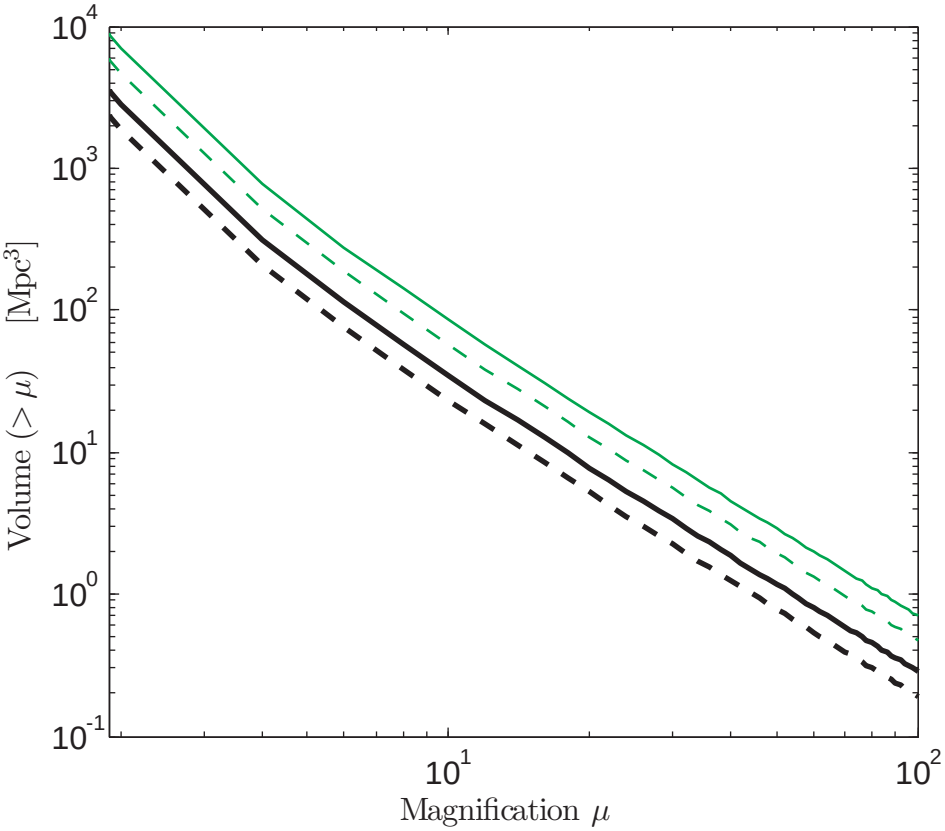

Figure 5.6.— Comoving source volume as a function of magnification μ and redshift z over a redshift interval of $\Delta z = 1$ for a SIS lens. The black and green lines denote Einstein radii of $35''$ and $55''$, respectively, while the solid and dashed lines denote $z = 6$ and $z = 10$, respectively. The results are in general agreement with more realistic estimates of the search areas per magnification factor for the magnification maps of the lensing clusters in the CLASH survey (Bouwens et al. 2012).

radii typical of high-magnification clusters. Given core-collapse SN rates of $\sim 10^{-3}$ yr^{-1} Mpc^{-3}, capturing SN with high magnifications within source volumes $< 10^2$ Mpc^3 is unlikely. Hence, we expect most lensed supernova detected to have their fluxes moderately boosted with $\mu \lesssim 5$; the benefit of lensing is to probe somewhat deeper redshifts, and to greatly extend the duration of visibility. Also, since high-redshift observations are background-limited, for a target signal-to-noise ratio, the limiting flux is proportional to $t^{-1/2}$, so even a modest magnification of $\mu \sim 3$ can reduce the required integration time by an order-of-magnitude.

This volume limitation of lensing also justifies our focus on core-collapse SNe, which have the highest volumetric rates. Although Type Ia SNe are brighter, their volumetric rate is a factor of 4 smaller than the core collapse rate at $z \approx 7$ (Pan et al. 2012a), with the difference drastically increasing with redshift due to the long delay times needed between star formation and explosion for some Type Ia events (Maoz et al. 2012). Pair-instability SNe from Pop III stars have volumetric rates at least two orders of magnitude lower.

5.5 Snapshot Rate

The snapshot 'rate' is the total number of events observed at a limiting flux within a given field (not per unit time). The differential snapshot rate can be calculated from equations (5.1) and (5.4) via

$$N(z, \mu)\, dz\, d\mu = R_{SN}(z)\, t(F_\nu, \mu, z)\, dV(z, \mu), \tag{5.7}$$

where $t(F_\nu, \mu, z)$ is the rest-frame duration over which an event with magnification μ will be brighter than the limiting flux F_ν at redshift z, for the observation wavelength ν under consideration. We find $t(F_\nu, \mu, z)$ using our spectral time-series for the Type IIP SN model described in §5.3. As we care about the apparent SN rate for observers, there is an implicit factor of $(1+z)^{-1}$ in front of the intrinsic volumetric supernova rate $R_{SN}(z)$, but that cancels with a $(1+z)$ factor for $t(F_\nu, \mu, z)$ due to cosmic time dilation.

In Figure 5.7, we plot the expected snapshot rate of magnified core-collapse SN detected by JWST above target redshifts, calculated by integrating equation (5.7) over μ and partially over z. Since NIRCam has two modules each with a 2.2×2.2 arcmin^2 field-of-view, we limit the source area in equation (5.4) to images that lie within this field-of-view.

We find that a 10^5s JWST snapshot with the F444W filter is expected to detect ~ 1 magnified core collapse SN at $z > 7$ around each cluster, and ~ 0.1 SNe at $z > 8$. Using ~ 5 clusters with $\theta_E \geq 35''$, the prospects for detecting a few non-superluminous SNe at high redshifts via lensing are high. If the other ~ 20 galaxy clusters in the CLASH survey with smaller Einstein radii of $\theta_E \sim 15''$–$30''$ are also included, the expected number of gravitationally lensed high-z SNe detected should double.

5.6 Discussion

At $z > 6$, the observed duration of gravitationally-lensed core-collapse SNe can reach $\gtrsim 1$ year, lending their detection to a search strategy of taking images separated by $\sim 0.5 - 1$ year, and looking for flux differences between consecutive snapshots. Ideally,

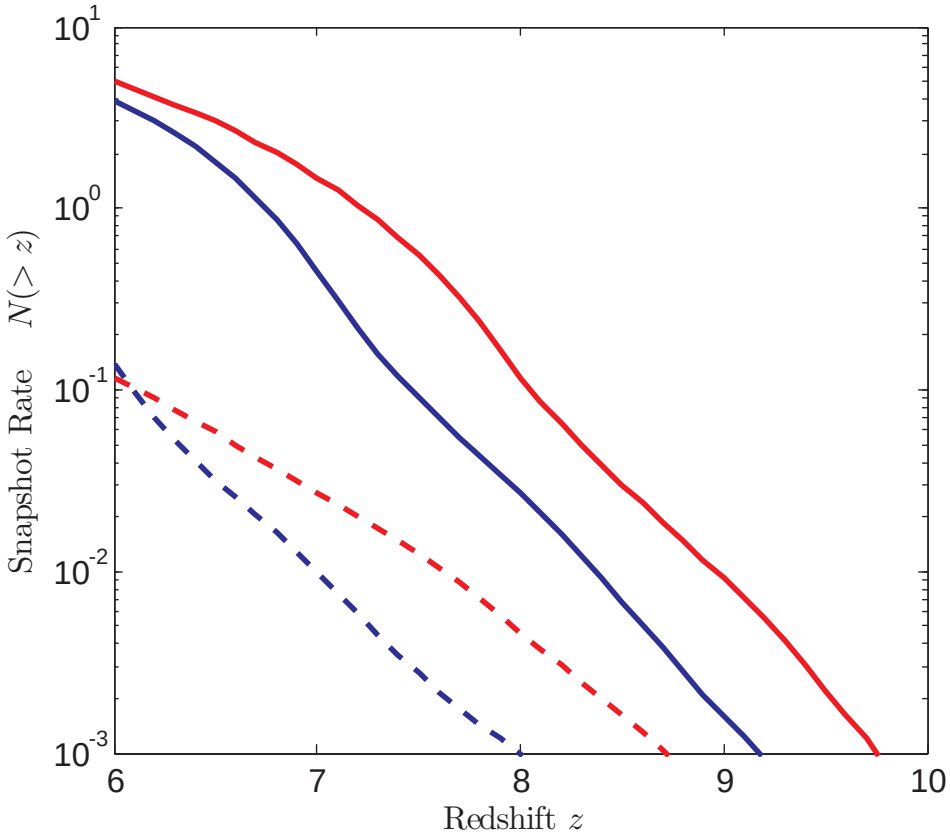

Figure 5.7.— The snapshot rate of gravitationally lensed core collapse SNe with JWST, for a *single* SIS lens with an Einstein radius $\theta_E = 35''$. Despite the higher sensitivity of the F356W band, the F444W band is better for finding lensed SNe at $z > 6$, as the SNe remain above the flux limit for a longer time. Note that 5–6 high-magnification galaxy clusters with $35'' \leq \theta_E \leq 55''$ are targeted in strong lensing surveys such as CLASH and HST Frontier Fields.

the cluster survey should cover most of the critical curve area, and not just known locations of magnified images of high-z galaxies, as the lensed SN may appear in currently 'dark' critical curve areas, and serve as a flag for its fainter host galaxy. The spectral energy distribution of Type II SNe is sufficiently different from blackbody to allow for photometric redshift determination, however, typing the SNe accurately may require time-consuming spectroscopy.

Our quantitative results improve upon previous calculations of the frequency of lensed SNe. For example, Marri et al. (2000) first explored the effects of gravitational lensing on high-z Type II SNe by intervening cosmological mass for different cosmologies, but the predicted detection rates were unrealistically high because of optimistic assumptions about JWST capabilities. Gunnarsson & Goobar (2003) explored the lensing by massive clusters of distant Type Ia and Type II SNe observed at wavelengths of 0.8-1.25 microns, but found the discovery rate tapered off at $z \sim 3$. Also, gravitational lensing is not required per se to detect Type II SNe from the epoch of reionization. A moderate JWST blank-field survey can obtain similar snapshot rates, albeit trading off the highest redshift events for more lower redshift ones compared to a lensing survey. For example, Mesinger et al. (2006) found that a 10^5s exposure with JWST can detect 4-24 SNe per field at $z > 5$, although the assumed SFRD $\sim 0.1 M_\odot$ yr^{-1} Mpc^{-3} was an order-of-magnitude higher than our estimates here, and the current specifications for JWST NIRCam filter sensitivities are now ~ 3 times worse than the values assumed at that time.

For more luminous SNe, Whalen et al. (2012) found that core collapse SNe from Pop III progenitors in the earliest galaxies could be visible with the deepest JWST surveys (reaching $M_{AB} = 32$) even at $z > 10$, as these SNe are bluer and almost

an order-of-magnitude brighter than the average Type II SNe considered in this paper. Whalen et al. (2013) also found that superluminous Type IIn SNe powered by circumstellar interactions from Pop III stars could be visible out to $z \sim 20$. Truly massive Pop III stars with masses $M \gtrsim 200 M_{\odot}$ can also die as extremely bright pair-instability supernova, detectable with JWST at $z > 15$ (Pan et al. 2012a; Hummel et al. 2012); indeed, the current record for the highest-redshift supernova ever observed is likely a pair-instability or pulsational pair-instability event at $z = 3.90$ (Cooke et al. 2012). However, the small volumetric density of Pop III stars makes it unlikely that these events will be strongly lensed. Finally, there is growing evidence of a prompt population of Type Ia SNe, so their volumetric rates during the later stages of reionization may not be negligible. With the fiducial SFRD model in this *Letter*, we estimate $\gtrsim 1$ gravitationally lensed Type Ia SNe could be discovered at $z > 7$ in the snapshots across the ~ 5 high-magnification clusters at any given time.

At lower redshifts, the measured core collapse SN rate is a factor of ~ 2 lower than that predicted from the cosmic star formation rate (Horiuchi et al. 2011); the most likely explanation is that some SN are dim, whether intrinsically faint or due to dust obscuration. This will reduce our predicted snapshot rate. However, we ignored the contribution of multiple lensing images in our analysis. Due to the gravitational lens time delay, which could be $\sim 1 - 100$ years for strong lensing around the clusters of interest (Coe et al. 2013), multiple images arriving at different times can increase the expected snapshot detection rate of separate SN within the same field-of-view. Although our SIS lens model can produce a maximum of only 2 magnified images, substructure and ellipticity in actual galaxy clusters will likely increase both the number of images and their magnifications.

Acknowledgments

We are grateful to Dan Kasen for providing the spectral time series data for the Type IIP SN model used in this letter. TP was supported by the Hertz Foundation and the National Science Foundation via a graduate research fellowship. This work was supported in part by NSF grant AST-0907890 and NASA grants NNX08AL43G and NNA09DB30A.

Chapter 6

Super-luminous X-ray emission from the interaction of supernova ejecta with dense circumstellar shells

Tony Pan, Dan Patnaude, Abraham Loeb.

arXiv:1303.6958

Accepted by *The Monthly Notices of the Royal Astronomical Society.*

Abstract

For supernova powered by the conversion of kinetic energy into radiation due to the interactions of the ejecta with a dense circumstellar shell, we show that there could be X-ray analogues of optically super-luminous SNe with comparable luminosities and energetics. We consider X-ray emission from the forward shock of SNe ejecta colliding

into an optically-thin CSM shell, derive simple expressions for the X-ray luminosity as a function of the circumstellar shell characteristics, and discuss the different regimes in which the shock will be radiative or adiabatic, and whether the emission will be dominated by free-free radiation or line-cooling. We find that even with normal supernova explosion energies of 10^{51} erg, there exists CSM shell configurations that can liberate a large fraction of the explosion energy in X-rays, producing unabsorbed X-ray luminosities approaching 10^{44} erg s^{-1} events lasting a few months, or even 10^{45} erg s^{-1} flashes lasting days. Although the large column density of the circumstellar shell can absorb most of the flux from the initial shock, the most luminous events produce hard X-rays that are less susceptible to photoelectric absorption, and can counteract such losses by completely ionizing the intervening material. Regardless, once the shock traverses the entire circumstellar shell, the full luminosity could be available to observers.

6.1 Introduction

An interesting question is whether there could be X-ray counterparts to super-luminous supernova, with comparable luminosities and/or total energy emitted. Excluding the energy emitted by neutrinos, most core collapse supernova (SN) have explosion energies of order 10^{51} ergs, but usually only 10^{49} ergs of that energy is released as optical radiation during the supernova, with typical peak luminosities not exceeding $\sim 10^{43}$ erg s^{-1}. However, numerous super-luminous supernovae with luminosities $\gtrsim 10^{44}$ erg s^{-1} were discovered over the past decade (Gal-Yam 2012), some of which had total radiated energies $\sim 10^{51}$ ergs, e.g. SN 2003ma (Rest et al. 2011) and SN 2006tf (Smith et al. 2008). Although a few of these events may be powered via radioactive decay, e.g. SN

2007bi (Gal-Yam et al. 2009), a distinct majority of super-luminous supernova require some other mechanism to power their radiative output.

One of the main mechanisms[1] invoked to convert a larger fraction of the large explosion energies into optical emission is via the strong interaction between the expanding supernova ejecta and massive circumstellar material (CSM) previously expelled by the star (Smith & McCray 2007). Similarly to Type IIn supernova, the bulk kinetic energy of the ejecta is converted back into radiation via strong shocks (Chevalier & Fransson 1994). The energetics of this process can be understood via the following toy model: if two objects of mass M_a, M_b with velocities v_a, v_b collide and stick together, conservation of energy and momentum dictates that the kinetic energy lost from the inelastic collision will be:

$$\Delta E_{kinetic} = \frac{1}{2}\frac{M_a M_b}{M_a + M_b}\left(v_a - v_b\right)^2 \tag{6.1}$$

If $v_a \gg v_b$, and the lost kinetic energy is converted to radiation with efficiency α, then the total radiated energy will be:

$$E_{rad} \approx \alpha \frac{M_b}{M_a + M_b} E_a, \tag{6.2}$$

where E_a is the kinetic energy of mass M_a.

For the CSM interaction scenario, where M_a is the supernova ejecta, and M_b is the circumstellar shell, this approximation is valid since a supernova ejecta's velocity typically reaches 10^4 km/s while mass previously ejected by stars have velocities ranging from $\sim 10^1$ to 10^3 km/s. Also, $E_a \sim 10^{51}$ ergs is approximately the total energy of the supernova, as adiabatic expansion quickly converts the initial deposited energy of

[1]The other main mechanism is the outward diffusion of deposited shock energy in optically thick CSM, i.e. the shock breakout, which can also produce X-rays; see Section 6.6.

the supernova into kinetic form. The radiative conversion efficiency is typically high, $\alpha \gtrsim 0.5$, at least for optical radiation from thermalized shock material (Moriya et al. 2013). Thus from equation (6.2), for a given total system mass and explosion energy, the energy radiated away is linearly proportional to the CSM mass M_b. So although most supernova only radiate 1% of their total kinetic energy, a large circumstellar mass M_b can substantially recover the supernova energy lost by adiabatic expansion. Notably, in this toy model, the total radiated energy does *not* depend on the location of the circumstellar mass M_b.

Several mechanisms may eject a large mass from the star prior to its death as a supernova. For example, luminous blue variables (LBVs) are evolved, unstable massive stars, and giant eruptions from LBVs result in dramatically increased mass loss and luminosity, some of which are so extreme that they are initially mistaken for supernova. These *supernova impostors* are powerful but non-terminal eruptions (i.e. not core collapse), however, there is direct evidence linking at least some LBVs and supernova impostors to actual supernova[2], e.g. SN 2006jc (Foley et al. 2007), in which the progenitor star is observed to violently erupt only 2 years before its terminal explosion; other examples include SN 2005gl (Gal-Yam et al. 2007; Gal-Yam & Leonard 2009) and possibly SN 2009ip (Mauerhan et al. 2012). Alternatively, some of the most massive stars with helium core masses between ~ 40 to 60 $M_\odot$ encounter core instability from the softening of the equation-of-state due to production of electron-positron pairs, which results in explosive burning that is insufficient to fully unbind the star, but can

[2]Despite the observational evidence associating some LBVs to supernova explosions, current theories of stellar evolution prohibit LBVs from directly exploding, as they are supposed to evolve into Wolf-Rayet stars first; this contradiction has not yet been resolved.

result in a sequence of supernova-like eruptions of shells of matter shortly before the star dies. The collision of subsequent shells of ejecta can also produce a superluminous supernova, i.e. the pulsational pair-instability SNe (Heger & Woosley 2002; Woosley et al. 2007; Chatzopoulos & Wheeler 2012). Also, the tunneling of wave energy from the core (driven by fusion-luminosity induced convection) into the stellar envelope can lead to extremely large stellar mass loss rates a few years prior to core-collapse (Quataert & Shiode 2012). Alternatively, the collective action of winds at different evolutionary stages of the progenitor star can form wind-blown cavities, bordered by a thin, dense, cold shell constituting material swept-up by the winds; the emission of SNe in these wind-blown bubbles have been examined (Chevalier & Liang 1989; Dwarkadas 2005).

Now, for CSM-interaction powered supernova, the generation of optical emission requires that high densities are still maintained when the SNe ejecta collides with the circumstellar material, usually implying the CSM is relatively near to the star ($\lesssim 10^{15}$ cm). However, the physical mechanism behind LBV outbursts is not yet known, so there is little theoretical constraint on the timing between the outburst and the supernova afterward; observational constraints so far set the lower limit to 40 days (Ofek et al. 2013a), but the delay can be years to decades or longer (Davidson & Humphreys 2012). As for the pulsational pair-instability mechanism, the interval between pulses can be anywhere from ~ 1 week to > 1000 years (Woosley et al. 2007). As longer delay times between eruptions imply that subsequent ejecta take longer to catch up to previous ejecta, it is quite possible that the collision between ejecta can occur at larger radii. As for the CSM shells bordering wind-blown bubbles, they are naturally placed by the duration of winds during late stellar evolutionary stages (e.g. Wolf-Rayet) at least 10^{19} to 10^{20} cm away from the star.

So, if instead the SNe ejecta encounters a massive CSM shell at larger radii $> 10^{15}$ cm, the shell material is spread thinner, and depending on the CSM shell mass, the resulting shock can be *optically thin*, albeit still dense enough to drive strong emission. Such an event could still radiate extreme amounts of energy, perhaps comparable to the currently observed superluminous SNe, but the actual optical emission could be quite modest, with the bulk of the radiation instead emitted in X-rays.

Moreover, in this scenario the bulk of the X-ray emission may come from the forward shock, i.e. from the shocked CSM shell. This has an important advantage compared with most cases of X-ray emission from young SNe (without a CSM shell), in which the reverse shock is usually denser, and the observed emission is usually attribute to line-cooling emission from the reverse shock running in the SNe ejecta, especially at later times (Chevalier & Fransson 2003). An important detriment of the cooling is that the intervening cooled, dense post-shock gas may photoelectrically absorb most of the emission from the reverse shock. However, even if the forward shock is radiative, and a cool, dense shell forms, this post-forward-shock cool gas will be *behind* the newly shocked CSM with respect to an observer on Earth – in contrast to the opposite arrangement for the reverse shock. Thus, for forward shock emission from SN & CSM shell interactions, only absorption and scattering by the pre-shock CSM is important, and even these go away once the forward shock runs through the CSM shell.

Chugai (1993) proposed an analogous scenario for the X-ray emission from SN 1986J, in which the emission originates from the forward shock front moving into dense wind clumps, and Chugai & Chevalier (2006) modeled the luminous X-ray emission $\sim 10^{41}$ erg s^{-1} of SN 2001em as interaction of normal SNe ejecta with a dense, massive CSM shell, albeit attributing the observed luminosity to a non-radiative reverse shock.

The evolution of SNe ejecta expanding into a power-law density CSM have been well studied (Chevalier 1982a,b), and simple formulas for its dynamics and emission exist in terms of self-similar solutions; however, these are not applicable for a CSM shell.

In this paper, we consider the forward shock emission from SN ejecta colliding into a CSM shell, and derive simple, general formulas for: (i) the regimes in which the shock will be radiative versus non-radiative, and whether the X-ray luminosity will be powered by free-free emission or line-cooling, and (ii) the approximate luminosity and total energy emitted as a function of the CSM shell mass, distance from the progenitor, and thickness, as well as the SN explosion energy. We give examples of possible extremely luminous or energetic emission events.

6.2 CSM Shell Characteristics

For the range of masses expelled in LBV eruptions, there have only been two outbursts where we can directly measure the ejected mass – around 10 $M_\odot$ for η Car, but only 0.1 $M_\odot$ for P Cygni (Smith et al. 2011a). As for pulsational pair-instability events, most pulses eject ~ 1 $M_\odot$ shells, but the full range also spans from ~ 0.1 to 10 $M_\odot$. Note that we make a distinction here between eruptive mass loss and wind-driven mass loss, which also occur for LBV-like progenitors of Type IIn SNe. Model-inferred wind-driven mass loss rates of Type II SNe progenitors are found to range from a few 10^{-2} to $10^{-1} M_\odot$ yr^{-1} (Kiewe et al. 2012), but smooth winds will result in a r^{-2} density distribution instead of a shell, unless the wind experiences dramatic changes in its mass loss rate or velocity right before stellar demise. Here we consider the range of masses M_{CS} of the CSM shell in between $10^{-2} M_\odot < M_{CS} < 10 M_\odot$, and define the dimensionless CSM shell mass

$M_1 \equiv (M_{CS}/1M_\odot)$.

For the range of locations for the CSM shell, we consider scenarios where the previously ejected shell of material is at a radius R_s of at least 10^{15} to 10^{17} cm, which means that even at supernova ejecta velocities of 10^4 km s^{-1}, the interaction event woould not happen until at least several months to several years after the progenitor star's explosion. Here we consider the radius R_{CS} of the CSM shell in the range of 10^{15} cm $< R_{CS} < 10^{19}$ cm, and define the dimensionless CSM shell radius $R_{17} \equiv (R_{CS}/10^{17}\mathrm{cm})$.

The thickness of the CSM shell is affected by the duration of the mass loss episode. For many models of episodic mass loss from massive stars, these eruptions occur for 1-10 years every 10^{3-4} years, and lose a total of $0.1 - 10M_\odot$ per episode. Note that if the mass loss is smooth during the episode, as in the Super-Eddington stead-state continuum driven wind through a porous medium (Shaviv 2000; Owocki et al. 2004), then if the heightened mass loss lasts 1 to 10 years with speed 100 km s^{-1}, the shell thickness is 3×10^{14} to 3×10^{15} cm. Alternatively, for explosive expulsions of mass, e.g. via the pulsational pair-instability, due to the spread in velocities of the expelled material, the thickness of the CSM shell may be substantial compared to the radius, $\Delta R_{CS}/R_{CS} \sim 1$. Conversely, for the dense shells bordering wind-blown bubbles, the shells are typically thin $\Delta R_{CS}/R_{CS} \sim 10^{-2}$. Here we consider the range of thicknesses ΔR_{CS} of the CSM shell in between 10^{13} cm $< \Delta R_{CS} < 10^{17}$ cm, and define the dimensionless CSM shell thickness $\Delta R_{15} \equiv (\Delta R_{CS}/10^{15}\mathrm{cm})$.

Assuming the CSM shell is spherically symmetric with uniform density, the surface density of the CSM shell is given by $\Sigma = M_{CS}/4\pi R_{CS}^2$:

$$\Sigma_{CS} = 1.6 \times 10^{-2}\, M_1\, R_{17}^{-2} \quad \mathrm{g\ cm^{-2}}. \tag{6.3}$$

The density of the CSM shell will depend on the thickness of the shell, $\rho_{CS} = \Sigma_{CS}/\Delta R_{CS}$, and so we define the electron number density of the CSM shell as

$$n_7 = \frac{n_{CS}}{10^7 \mathrm{cm}^{-3}} = 0.95\, M_1\, R_{17}^{-2}\, \Delta R_{15}^{-1}. \tag{6.4}$$

Note that $n_{CS} \approx 10^7$ cm^{-3} corresponds to a mass density of $\rho_{CS} \approx 1.7 \times 10^{-17}$ g cm^{-3}. In reality, the CSM shell may be clumpy, but the clumps could be completely crushed and then mixed within the forward shock, making okay the smooth shell approximation at least for the calculation of post-shock dynamics and its X-ray emission (Chugai & Chevalier 2006).

We only consider regimes where the CSM shell is optically thin, i.e. the optical depth of the CSM shell for electron scattering $\tau = \kappa_{es}\Sigma_{CS}$ is less than unity:

$$\tau = 5.4 \times 10^{-3}\, M_1\, R_{17}^{-2} < 1. \tag{6.5}$$

Note that this line-of-sight optical depth does not change even if the post-shock material is compressed and the density rises. Here we adopt the electron scattering opacity, $\kappa_{es} \approx 0.34$ cm^2 g^{-1} at solar abundances. Once the supernova ejecta collides with the CSM shell, the shock will heat up the shell material, and the temperature right behind the forward shock could reach $10^7 - 10^9$ K, generating $1 - 100$ keV photons. But unlike other superluminous Type IIn supernova, in the scenarios considered in this paper, as the shocked material cools and emits free-free radiation, such radiation will generally **not** be re-processed and thermalized by the circumstellar material (to $T \sim 5,000 - 20,000$ K blackbodies temperatures, resulting in optical emission), but instead immediately leak away as X-rays.

6.3 Theory: Simple Formulas

6.3.1 Shock Velocity, Temperature, and Cooling Mechanism

We assume the pre-shock CSM shell is effectively stationary, i.e. the shock velocity v_s is much greater than the original velocity of the CSM shell. To find the shock velocity v_s of the forward shock traveling through the CSM shell, we can write the force equation for the shocked CSM shell:

$$\frac{d}{dt}\Sigma_s v_s = P_s(t) \tag{6.6}$$

where $P_s(t)$ is the pressure interior to the CSM shell *after* the SN shock hits the shell, and

$$\Sigma_s = \int_0^{x_s} \rho_{CS}\, dx \tag{6.7}$$

is the surface density of matter in the shocked CSM shell, and x_s is the distance that the shock has propagated into the CSM shell. If we make the approximation that the shock velocity is constant, at least within the CSM shell, then we can derive from equations (6.6) and (6.7) that $\rho_{CS}\, v_s^2 = P_s$; that is, the ram pressure pushing back on the shocked CSM shell moving at velocity v_s (thin shell approximation) into the external, stationary CSM equals the post-shock pressure interior to the shocked CSM shell. Therefore,

$$v_s = \left(\frac{P_s}{\rho_{CS}}\right)^{1/2}. \tag{6.8}$$

Now, we can approximate the pressure exerted by the SN ejecta immediately before the shock hits the CSM shell as $P_{SN} = (\gamma - 1)E_{SN}/V_{SN} = E_{SN}/2\pi R_{CS}^3$; here V_{SN} is the volume interior to the shell, and we assume a $\gamma = 5/3$ gas in this paper. This assumes the supernova energy is thermalized, which is generally true if the CSM shell mass is

comparable to the SN ejecta mass. For convenience, we define the dimensionless SN explosion energy $E_{51} \equiv (E_{SN}/10^{51}\mathrm{erg})$.

However, once the shock hits the CSM shell, the kinetic energy of the flow is converted into thermal energy, and the pressure rises above P_{SN}. By solving the one-dimensional non-radiative gas dynamics of a plane-parallel shock impinging on a density discontinuity, it can be shown that the immediate post-transmitted shock pressure is a factor β greater than the pre-transmitted shock pressure, where β is a function of the density ratio ρ_{CS}/ρ_0 across the density discontinuity at the CSM shell, and ρ_0 is the density of material interior to the CSM shell (Sgro 1975):

$$\begin{aligned} \frac{\rho_{CS}}{\rho_0} &= \frac{3A_r(4A_r-1)}{\{(3A_r(4-A_r))^{1/2}-5^{1/2}(A_r-1)\}^2}, \\ \beta &= \frac{4A_r-1}{4-A_r}. \end{aligned} \tag{6.9}$$

Instead of expressing subsequent equations as a complicated function of ρ_0, we use the shock pressure increase factor β to parametrize the severity of increase in density at the CSM shell; β monotonically increases from 1 to 6, as ρ_{CS}/ρ_0 increases from 1 (no obstacle) to ∞ (solid wall), with $\beta = 2.6$, 4.4, 5.4, and 5.8 for $\rho_{CS}/\rho_0 = 10$, 10^2, 10^3, and 10^4. The large values of β are transitory, and apply when the shock first propagates into the denser region. Also note the immediate post-shock density n_s increases by a factor of $(\gamma+1)/(\gamma-1) = 4$ over the pre-shock density n_{CS}. Hence,

$$v_s = \left(\frac{\beta\, P_{SN}}{\rho_{CS}}\right)^{1/2}. \tag{6.10}$$

Note that this is approximately equal to another formula in literature, i.e. $v_s \approx v_{SN}\sqrt{\rho_{SN}/\rho_{CS}}$ (Chugai 1993), where v_{SN} is the SN ejecta velocity. In this paper, we only consider the forward shock propagating in the CSM shell; but note that after the

forward shock overruns the dense CSM shell, the shock will accelerate as it encounters sparser material, and can be modeled using the formalism of Dwarkadas (2005).

Thus, we can derive the dimensionless shock velocity $v_8 \equiv (v_s/10^8 \mathrm{cm\,s^{-1}})$ as:

$$v_8 = 1.00\,\beta^{0.5}\,E_{51}^{0.5}\,M_1^{-0.5}\,R_{17}^{-0.5}\,\Delta R_{15}^{0.5}. \tag{6.11}$$

For a strong shock with an infinite Mach number, the conservation of mass, energy, and momentum dictate that the temperature right behind the shock can be related to the shock velocity v_s via $kT = 2[(\gamma-1)/(\gamma+1)]\,m_i\,v_s^2$, where k is Boltzmann's constant, γ is the adiabatic index, and T_i, m_i are the temperatures and ion masses of each plasma species. Note that if an electron-proton plasma is maximally out of thermal equilibrium, then $T_e/T_p \sim m_e/m_p \sim 1/1836$; clearly, whether electron-ion energy equipartition has been reached has great consequence to the electron temperature and thus the observational signature. If the plasma is in full thermal equilibrium, we can use a single temperature T to describe it, with

$$T \approx 1.36 \times 10^7\,v_8^2 \quad \mathrm{K} \tag{6.12}$$

Here we have assumed a mean atomic weight $\mu \approx 0.6$ for a fully ionized plasma of solar abundance.

The timescale for electrons and ions to reach equipartition is $t_{eq} \approx 8.4\,T^{3/2}\,n^{-1}$ in cgs units (Spitzer 1962), implying

$$t_{eq} \lesssim 10^4\,v_s^3\,n_7^{-1} \quad \mathrm{s} \tag{6.13}$$

where the inequality originates from the fact the post-shock density $n_s \geq 4n_{CS}$ depending on whether the shocked gas further cools and compresses. As we shall see, for most high

luminosity cases, energy equipartition will be reached in a lot less than a day, with t_{eq} being far less than the cooling time t_{cool} or the shock traversal time through the CSM shell t_{flow}, and it is mostly safe to assume the electron temperature is the same as the temperature of the ions.

The subsequent luminosity of the shocked hot gas is driven by their mechanism of radiative cooling, captured by the cooling function Λ. Even at solar metallicity, the cooling function is a complicated function of temperature. For simplicity, we approximate its behavior into two regimes (Chevalier & Fransson 1994): When $T > 4 \times 10^7$ K, free-free emission dominates, and $\Lambda \approx 2.5 \times 10^{-27} T^{0.5}$ erg cm^3 s^{-1}, whereas when 10^5 K $< T \lesssim 4 \times 10^7$ K, line emission increases, and $\Lambda \approx 6.2 \times 10^{-19} T^{-0.6}$ erg cm^3 s^{-1}; these are rough fits to the cooling curves calculated by Raymond et al. (1976). Hence, we can define a dimensionless cooling function $\Lambda_{-23} = \Lambda(T)/10^{-23}$erg cm^3 s^{-1}:

$$\Lambda_{-23} = \begin{cases} 0.92\, v_8 & \text{if } v_8 > 1.7 \text{ (free-free)} \\ 3.25\, v_8^{-1.2} & \text{if } v_8 < 1.7 \text{ (line-cooling)} \end{cases} \tag{6.14}$$

In reality, the cooling function Λ is a function of the emitted photon frequency μ as well, and a detailed $\Lambda(T, \mu)$ would provide us with an emission spectrum. We utilize this more involved approach to simulations in §6.5.

6.3.2 Radiative vs Non-radiative Shock

A radiative shock typically forms when the density of the ambient medium is high enough, such that the emitted radiation affects the dynamics of the gas behind the shock; this occurs when the cooling time t_{cool} is shorter than the hydrodynamical time

$t_{flow} \approx \Delta R_{CS}/v_s$:

$$t_{flow} = 0.32\,\Delta R_{15}\,v_8^{-1} \quad \text{yr} \tag{6.15}$$

The cooling time of a gas element in a shock can be calculated as the ratio between the thermal energy density $\epsilon = 3/2 n_s kT$ and the cooling rate per unit volume $\hat{\Lambda} = n_s^2 \Lambda$ (Franco et al. 1993):

$$t_{cool} = \frac{\epsilon}{\hat{\Lambda}} \approx \frac{3kT}{2n_s \Lambda(T)}, \tag{6.16}$$

where n_s is the immediate post-shock density. Thus, depending on the shock temperature,

$$t_{cool} = \begin{cases} 0.24\,v_8\,n_7^{-1} & \text{yr} \quad \text{if } v_8 > 1.7 \text{ (free-free)} \\ 0.07\,v_8^{3.2}\,n_7^{-1} & \text{yr} \quad \text{if } v_8 < 1.7 \text{ (line-cooling)} \end{cases} \tag{6.17}$$

Thus, the condition for a radiative shock $t_{cool} < t_{flow}$ can be expressed as:

$$\begin{cases} v_8^2 & < 1.31\,n_7\,\Delta R_{15} \quad \text{if } v_8 > 1.7 \text{ (free-free)} \\ v_8^{4.2} & < 4.61\,n_7\,\Delta R_{15} \quad \text{if } v_8 < 1.7 \text{ (line-cooling)} \end{cases} \tag{6.18}$$

We plot the dependence of these different regimes on the CSM shell mass M_1, radius R_{17}, and thickness ΔR_{15} in Figures 6.1 – 6.6, noting that the transition between regimes is much smoother than depicted.

6.3.3 Luminosity and Total Energy Emitted

Non-radiative shock

The X-ray luminosity of a non-radiative shock heated plasma can be calculated as $L = \text{EM} \times \Lambda$, where EM is the emission measure, and Λ is the cooling function. The emission measure for the fully shocked CSM shell can be calculated as the emission volume $V_{CS}/4$, which is the CSM shell volume $V_{CS} = 4\pi R_{CS}^2 \Delta R_{CS}$ compressed by the

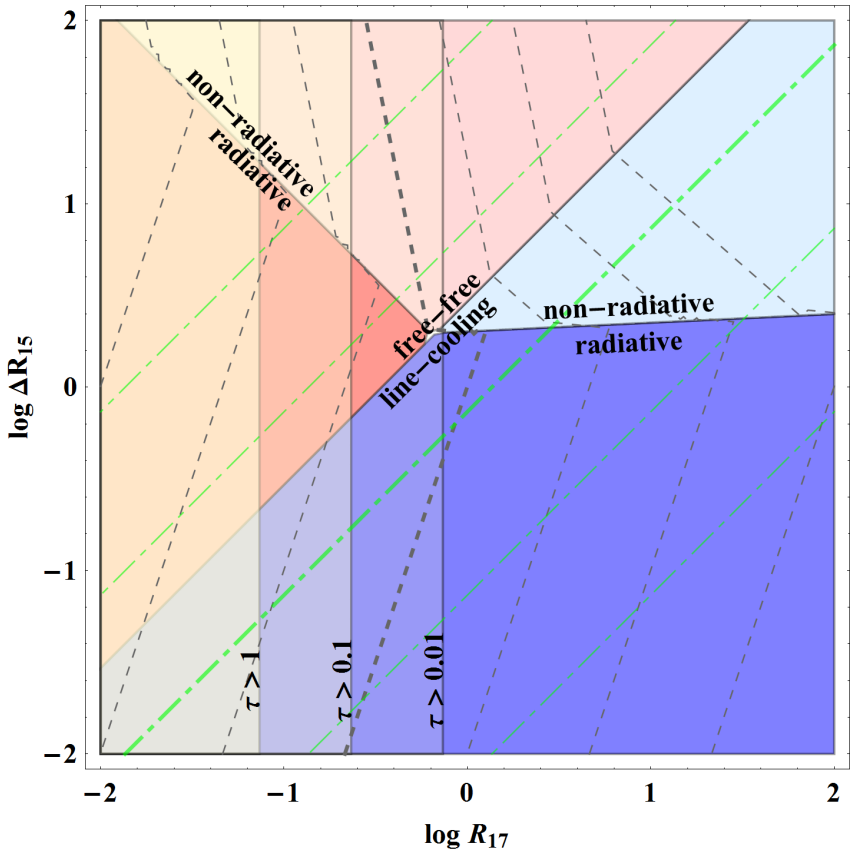

Figure 6.1.— Emission properties of the shock in the CSM shell, varying the shell radius $R_{17} \equiv (R_{CS}/10^{17}\mathrm{cm})$ and thickness $\Delta R_{15} \equiv (\Delta R_{CS}/10^{15}\mathrm{cm})$, with $E_{51} = 1$, $M_1 = 1$, $\beta = 1$. The following series of figures show other different choices for the SN explosion energy $E_{51} \equiv (E_{SN}/10^{51}\mathrm{erg})$, shell mass $M_1 \equiv (M_{CS}/1M_\odot)$, and the shock pressure increase factor β (equation (6.9)). The red and blue regions cover where the shock is dominated by free-free emission or line-cooling, respectively, in which the darker red and blue regions depict where the shock is radiative. The overlapping yellow regions show where the electron scattering optical depth along the line of sight is greater than $\tau >$ 0.01, 0.1, and 1, respectively.

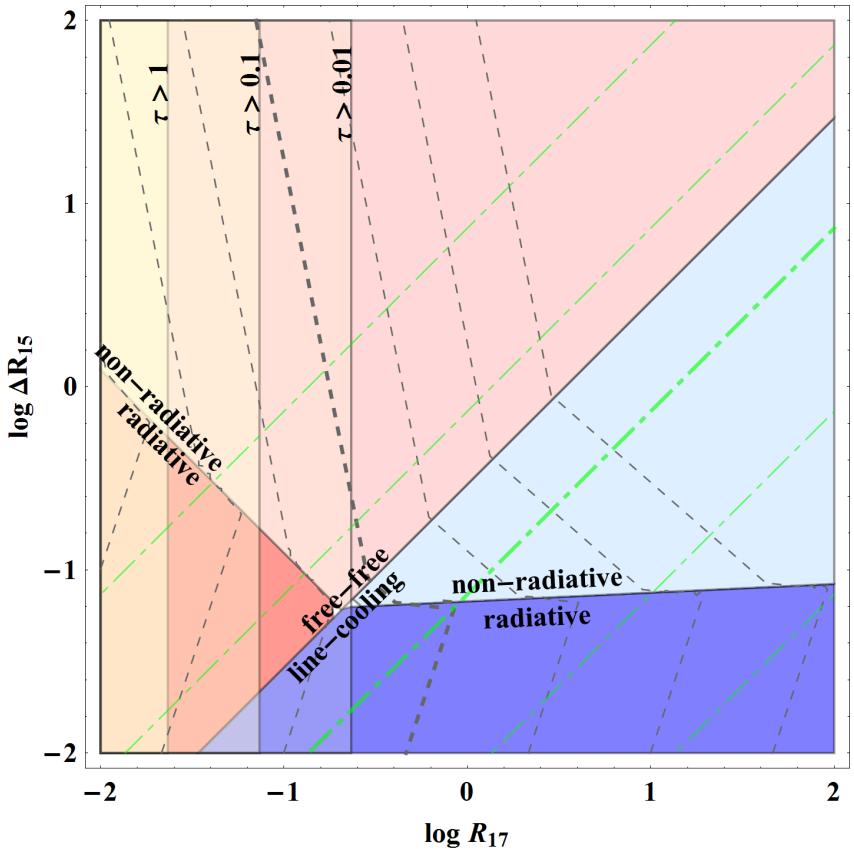

Figure 6.2.— Emission properties of the shock in the CSM shell, varying the shell radius R_{17} and thickness ΔR_{15}, with $E_{51} = 1$, $M_1 = 0.1$, $\beta = 1$. The color and dashed-line notation is the same as Figure 6.1; the dashed gray lines depict contours of constant X-ray luminosity, with the thicker line indicating where $L_{42} \equiv (L/10^{42}\mathrm{erg\,s^{-1}}) = 1$; each adjacent line toward the left is more luminous by a factor of 10. The luminosity roughly increases with τ, but at $\tau > 1$ the X-rays start being reprocessed into optical emission instead; hence 10^{44} to 10^{45} erg s^{-1} is the maximum X-ray luminosity possible. Similarly, the dot-dashed green lines depict contours of constant shock temperature, with the thicker line indicating where $T = 10^7$ K; each adjacent line in the direction of the red region is hotter by a factor of 10.

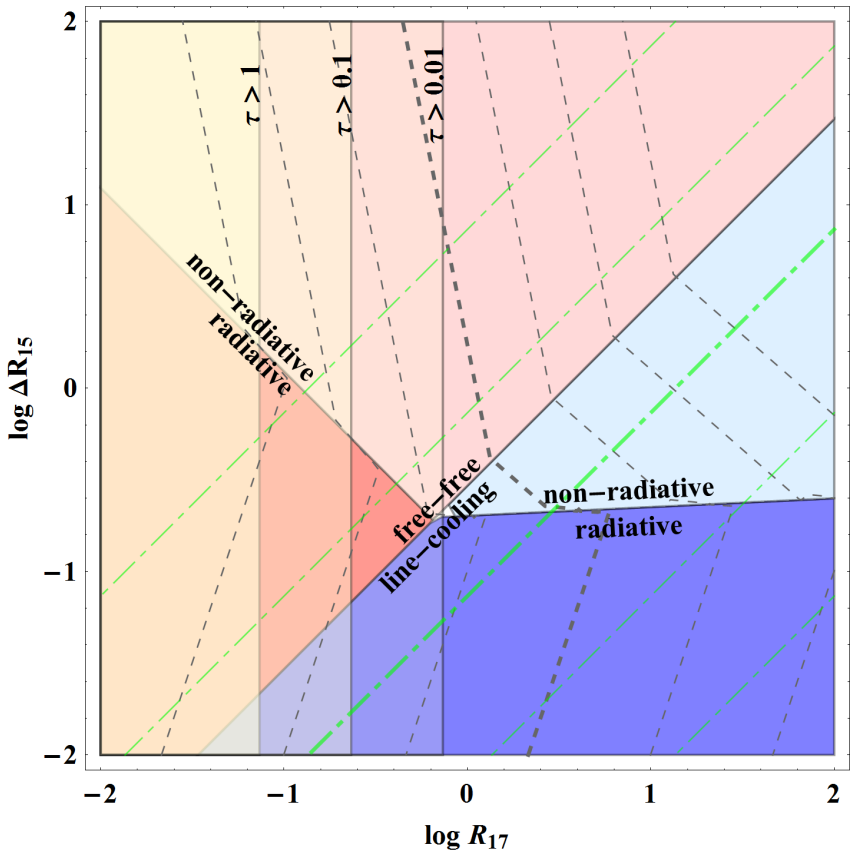

Figure 6.3.— Emission properties of the shock in the CSM shell, varying the shell radius R_{17} and thickness ΔR_{15}, with $E_{51} = 10$, $M_1 = 1$, $\beta = 1$. The color and dashed-line notation is the same as Figure 6.1. Although luminosities up to a few 10^{44} erg s^{-1} are possible at $\tau \lesssim 1$, photoelectric absorption is severe (equation (6.27)), and so except for high temperature shocks $T \sim 10^9$ K emitting many $\gtrsim 20$ eV photons, the full luminosity won't be observable until the shock runs through the entire CSM shell. Similarly, for 10^{43} erg s^{-1} pre-absorption luminosities, the early shock emission will be completed obscured unless the temperature reaches $T \gtrsim 10^8$ K. For the same optical depth (i.e. column density), the highest luminosities are best reached via radiative shocks dominated by free-free emission.

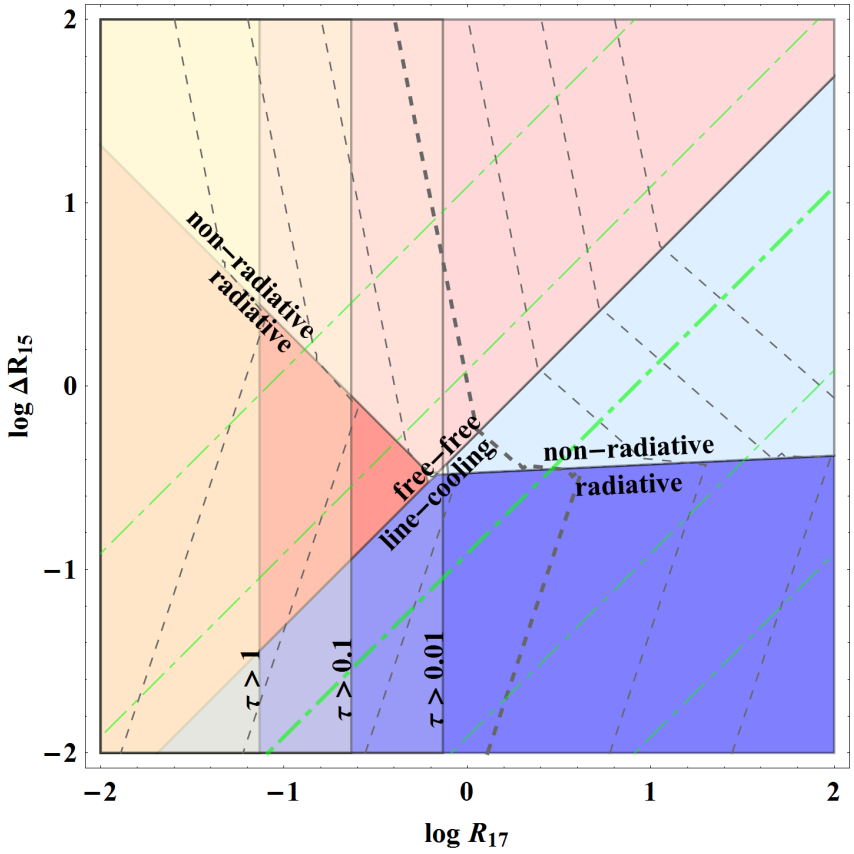

Figure 6.4.— Emission properties of the shock in the CSM shell, varying the shell radius R_{17} and thickness ΔR_{15}, with $E_{51} = 1$, $M_1 = 1$, $\beta = 6$. The color and dashed-line notation is the same as Figure 6.1.

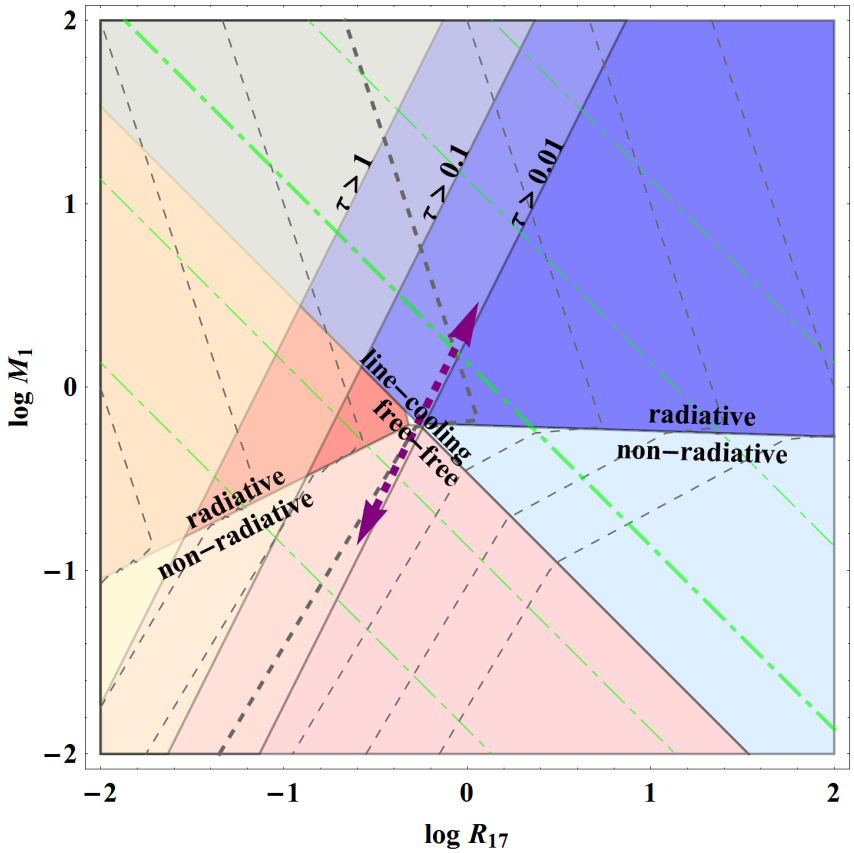

Figure 6.5.— Emission properties of the shock in the CSM shell, varying the shell radius R_{17} and mass M_1, with $E_{51} = 1$, $\Delta R_{15} = 1$, $\beta = 1$. The color and dashed-line notation is the same as Figure 6.1. Note that the intersection point (R'_{17}, M'_1) between the free-free vs line-cooling boundary and the radiative vs non-radiative boundary behaves as $R'_{17} \propto \Delta R_{15}^{1/3} E_1^{1/3}$ and $M'_1 \propto \Delta R_{15}^{2/3} E_1^{2/3}$, so that changing ΔR_{15} or E_1 would simply move the intersection point along the purple arrow. Therefore, the intersection point will always lie around where optical depth $\tau = 0.01$ (as τ is independent of ΔR_{15} and E_1), thus the free-free & radiative regime will always have $\tau > 0.01$, with a pre-shock CSM shell column density $N_H > 1.8 \times 10^{22}$ cm^{-2}.

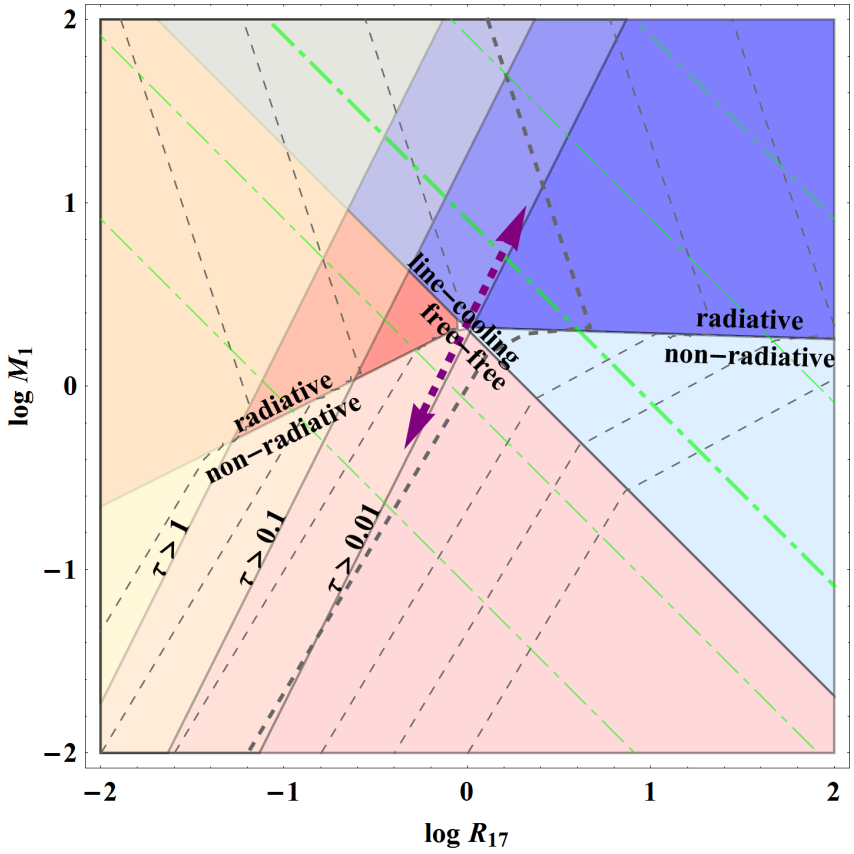

Figure 6.6.— Emission properties of the shock in the CSM shell, varying the shell radius R_{17} and mass M_1, with $E_{51} = 1$, $\Delta R_{15} = 1$, $\beta = 6$. The color and dashed-line notation is the same as Figure 6.5.

shock, multiplied by the square of the post-shock density $n_s = 4n_{CS}$, assuming that the density is uniform throughout. Thus,

$$\mathrm{EM} = 4.50 \times 10^{64}\, M_1^2\, R_{17}^{-2}\, \Delta R_{15}^{-1} \quad \mathrm{cm}^{-3}. \tag{6.19}$$

Combined with the cooling rate at different shock velocities/temperatures in equation (6.14), we can find the non-radiative luminosity as a function of system parameters, expressed in terms of a dimensionless X-ray luminosity $L_{42} \equiv (L/10^{42}\mathrm{erg\,s^{-1}})$ as follows.

When $v_8 > 1.7$, the luminosity of the non-radiative shock set by free-free emission (thermal bremsstrahlung) is

$$L_{42} = 0.42\, \beta^{0.5}\, E_{51}^{0.5}\, M_1^{1.5}\, R_{17}^{-2.5}\, \Delta R_{15}^{-1.5}. \tag{6.20}$$

When $v_8 < 1.7$, the luminosity of the non-radiative shock set by line-cooling is

$$L_{42} = 1.46\, \beta^{-0.6}\, E_{51}^{-0.6}\, M_1^{2.6}\, R_{17}^{-1.4}\, \Delta R_{15}^{-1.6}. \tag{6.21}$$

Assuming no other energy loss mechanism, we can naively estimate the total energy emitted as $L_X t_{cool}$; however, since non-radiative shocks can have extremely long cooling times, expansion of the shocked CSM shell can convert its thermal energy back into bulk kinetic form, instead of eventually emitting the energy as radiation. The shocked CSM shell expansion time scale is roughly:

$$t_{exp} = 31.7\, R_{17}\, v_8^{-1} \quad \mathrm{yr}. \tag{6.22}$$

This is the time it takes the shocked shell to double in radius, and lose half its energy via PdV work. Therefore, we estimate the total energy released via:

$$E_X = L \times \min(t_{cool}, t_{exp}). \tag{6.23}$$

Radiative shock

An important difference between a radiative shock and a non-radiative shock is that the former can increase the density drastically by a factor of $f_n \gg 4$. Immediately downstream from the shock, the Rankine-Hugoniot jump conditions are still valid, and the density has been compressed by only a factor of 4. However, as the shocked gas radiates energy away further downstream, its temperature drops precipitously, and its density increases to compensate and keep the total pressure constant. At approximately a cooling length $L_{cool} = v_s t_{cool}$ away, the shocked gas condenses into a cold, dense shell; the density increase is usually limited to a factor of ~ 100 by magnetic pressure.

Therefore, in calculating the luminosity of a radiative shock, the emission measure will never reflect the entire shocked CSM shell volume, as material one cooling length L_{cool} downstream from the shock will have cooled 'completely' and no longer contribute X-ray emission. The emission measure can thus be approximated as the emission volume $4\pi R_{CS}^2 L_{cool}/f_n$ (accounting for compression) multiplied by the post-shock density squared $n_s^2 = f_n^2 n_{CS}^2$. Using equation (6.16), and noting that the average kinetic energy $3/2kT \approx 1/2 m_p v_s^2$ per particle, we find that the kinetic energy of the explosion is converted to radiation at a rate:

$$\begin{aligned} L &= 2\pi\, R_{CS}^2\, \rho_{CS}\, v_s^3 \\ &= 0.99 \times 10^{42} M_1\, \Delta R_{15}^{-1}\, v_8^3 \quad \mathrm{erg\,s^{-1}}, \end{aligned} \tag{6.24}$$

where ρ_{CS} is the pre-shock density. Hence, the luminosity of a radiative shock is

$$L_{42} = 0.99\, \beta^{1.5}\, E_{51}^{1.5}\, M_1^{-0.5}\, R_{17}^{-1.5}\, \Delta R_{15}^{1.5}. \tag{6.25}$$

Note that because of occultation by the interior SN ejecta, only half of the above

X-ray luminosity typically escapes to the observer. However, since the X-ray emission from the radiative forward shock will emit in all directions, i.e. both toward the observer, and backward into the cooled material behind the forward shock front, the latter cold dense material could reprocess the X-ray, resulting in concurrent optical emission.

The total energy released in X-rays can be approximated as $E_X \approx L \times t_{flow}$. However, if photoelectric absorption is severe (see next subsection), and none of the emitted X-rays escape until the shock front reaches the end of the CSM shell, the total energy emitted observable in X-rays may only be $E_X \approx L \times t_{cool}$.

6.3.4 Scattering and absorption with the pre-shock CSM shell

We first emphasize that, after the shock runs through and superheats the entire CSM shell, many effects that decrease the transmitted X-ray flux become irrelevant, as there is no intervening material left from the initially cold CSM shell to absorb or scatter X-ray photons. This is implicitly assumed in our luminosity formula for non-radiative shocks in equations (6.20) and (6.21), which consider the entire volume of the shocked CSM shell in the emission measure. However, it is useful to understand photon interactions with the pre-shock CSM, to characterize the observable emission of the forward shock at early times as it just begins to propagate through the CSM shell.

The pre-shock column density $N_H \approx \Sigma/m_p$ of the CSM shell is given by

$$\begin{aligned} N_H &\approx 9.5 \times 10^{21}\, M_1\, R_{17}^{-2} \quad \mathrm{cm}^{-2} \\ &\leftrightarrow 1.8 \times 10^{24}\, \tau \quad \mathrm{cm}^{-2}. \end{aligned} \tag{6.26}$$

In the second equation, we express N_H as a function of the electron scattering optical

depth τ (from equation (6.5)) from an equivalent but fully *ionized* column, for ease of comparison via the constant τ contours in Figures 6.1 to 6.6, even though N_H refers to neutral material. The effective cross-section for photoelectric absorption is $\sigma(\lambda) \approx 2.2 \times 10^{-25} \lambda^{8/3}$ cm^2 for a solar composition gas, where λ is the X-ray photon wavelength in units of Å. This implies the threshold photon energy for photoelectric absorption is

$$E(\tau_{pe} = 1) \approx 1.2 \left[\frac{N_H}{10^{22} \mathrm{cm}^{-2}} \right]^{3/8} \quad \mathrm{keV}, \tag{6.27}$$

below which we can assume the observed spectrum is suppressed (Chevalier & Fransson 2003). Note that the dense CSM shell is likely to be fragmented and clumpy, due to Rayleigh-Taylor instabilities. For a fixed shell mass, a non-uniform, clumpy shell will typically result in less overall absorption compared with the uniform density shell we have assumed in this paper; so our inferences regarding photoelectric absorption are somewhat pessimistic. In any case, for column densities $N_H \geq 10^{24}$ cm^{-2}, X-rays < 10 keV are absorbed, and one needs to observe the source at 10-100 keV. If the column density increases to $N_H \approx 10^{25}$ cm^{-2}, primary X-rays up to several tens of keV are absorbed. So in order to observe high X-ray luminosities before the shock has passed through the CSM shell, simply requiring the optical depth $\tau \lesssim 1$ of the ionized CSM shell is grossly insufficient, unless the shock temperature is high $T \sim 10^9$ K ($v_8 \sim 10$), or that the shock luminosity itself can ionize the CSM shell.

Assuming that photoionization is determined by the current X-ray luminosity, we can define an ionization parameter $\xi = L/nR^2$ in cgs units (Tarter et al. 1969):

$$\xi = 10 \, L_{42} \, M_1^{-1} \, \Delta R_{15}, \tag{6.28}$$

which determines the ratio of photon flux to particle number density for a fixed

temperature of the X-ray source. Typically, for shock temperatures around $T \sim 10^8$ K, the intermediate elements (such as C, N, O) are fully ionized when $\xi > 10^2$, but ionizing the heavier elements such as Fe require $\xi \geq 10^3$. The medium is completely ionized once $\xi \sim 10^4$ (Chevalier & Irwin 2012), and there is no photoelectric absorption regardless of high column densities. These conditions are slightly modified for higher energy photons from $T \sim 10^9$ K shocks, as they are more effective at ionizing atoms with higher atomic numbers.

Also, Compton scattering can affect the escape of high-energy photons, as the inelastic scattering of photons transfers energy from the photon away to the scattered electron, increasing the photon wavelength by $\sim h/m_e c$ and thus decreasing the photon energy by $\Delta E \sim E^2/m_e c^2$. Since the number of scatterings is $\sim \tau_{es}^2$, above a cutoff energy $E_{max} = \Delta E \tau_{es}^2$ the photon energy will be entirely depleted via Comptonization. Therefore, the cutoff energy can be approximated via $E_{max} \sim m_e c^2/\tau_{es}^2$. But since the pre-shock optical depth $\tau_{es} < 1$ for the scenarios considered in this paper, most of our X-ray emission at photon energies $\ll 0.5$ MeV will not suffer Compton degradation.

6.4 Possible Luminous Events

Next, we discuss possible configurations of the CSM shell that give rise to luminous X-ray emission $\gg 10^{42}$ erg s^{-1}, i.e. more luminous than any X-ray transient observed so far attributed to SN ejecta interactions with the CSM. Conservatively, we use only typical SN explosion energies of 10^{51} erg (despite the fact that many optically superluminous SNe have been inferred to have $> 10^{52}$ erg explosion energies), and we also assume that the post-transmitted shock pressure does not increase substantially, i.e. $\beta \approx 1$. In

actuality, the density jump from the CSM shell interior to the shell itself can be very large, and $\beta \approx 5$ - 6 is quite possible, at least when the shock first enters the dense CSM shell; therefore, our estimates may have underestimated the maximum shock velocity by a factor of $\beta^{0.5}$, the maximum shock temperature by a factor of β, and the peak luminosity of radiative shocks by a factor of $\beta^{1.5} \sim 10$!

Generally, in our parameter space, CSM shells that give rise to the most luminous X-rays $L \gtrsim 10^{44}$ erg s^{-1} have radii $R_{CS} \leq 10^{16}$ cm; this is because higher luminosities are reached at higher shell densities, with the largest luminosities being reached when the Thomson scattering optical depth τ is very close to 1 but not greater. Luminosities above 10^{43} erg s^{-1} are generally dominated by free-free emission. We give specific examples below, and briefly discuss their observational signature. Note that our models assume spherical symmetry, but when the CSM shell is narrow i.e. $\Delta R_{CS}/R_{CS} \ll 1$, or when photoelectric absorption limits detectable X-ray emission to the edge of the CSM shell, the breaking of spherical symmetry can severely reduce the luminosity calculated via our models. Fortunately, the super-luminous long duration events described in Section 6.4.1 can be found either for radiative shocks in moderately thick shells, or non-radiative shocks with very large emission volumes, for which $\Delta R_{CS}/R_{CS}$ is not small.

6.4.1 Long duration events

Super-luminous & energetic free-free emission

In this example, the CSM shell has a mass of $1 M_{\odot}$, radius of 10^{16} cm, and thickness of 10^{16} cm, reaching a pre-shock density of 10^{8} cm^{-3}. Electron-ion energy equipartition is reached in $t_{eq} \sim 10$ days or less, and the unabsorbed luminosity from the radiative shock

attains $\sim 10^{44}$ erg s^{-1} for about 100 days, liberating a majority of the SN explosion energy; this is our X-ray analogue of optically super-luminous SN! In this extreme case, the shock is essentially trapped in the CSM shell; the kinetic energy of the SN ejecta will be radiated away, and this infant supernova remnant, less than one year of age, will go directly to the radiative phase, avoiding the Sedov phase.

The initial column density is a staggering 10^{24} cm^{-2}, which if neutral can absorb all X-rays below ~ 7 keV. However, not only does the fast $v_s \sim 10^4$ km s^{-1} shock emit photons $\gtrsim 20$ keV, but the large ionization parameter $\xi \sim 10^4$ implies that the early shock luminosity will quickly and completely ionize the remaining unshocked CSM shell material, warding off photoelectric absorption. Therefore, the $\sim 10^{44}$ erg s^{-1} intrinsic luminosity will be observable for most of this event's 3 month duration.

Non-radiative shocks can generate luminous events too. For example, for a shell mass of $0.2M_{\odot}$, radius of 5×10^{15} cm, and thickness of 2×10^{15} cm, when the shock escapes the shell, a peak X-ray luminosity of 5×10^{43} erg s^{-1} is attained, after which the entire shocked CS emits and cools for 1 month. These adiabatic shocks can have long equipartition times; here $t_{eq} \sim 9$ days is not an issue, but other luminous, non-radiative shocks could have equipartition times significantly exceeding the cooling time.

Regardless of whether the shock is radiative or not, we find that almost all super-luminous (i.e. $> 10^{43}$ erg s^{-1}) and long-duration (i.e. $\gg 1$ day) events have fast, hot shocks dominated by free-free emission. Less luminous versions have already been seen, e.g. SN 2010jl (Chandra et al. 2012a), and a candidate super-luminous X-ray event, SCP 06F6, was reported after this paper was submitted (Levan et al. 2013), see Section 6.6.

Luminous line-emission from radiative shocks

We consider a massive $5M_{\odot}$ CSM shell with a radius of 2×10^{16} cm, and thickness of 2×10^{15} cm. The pre-shock density is quite high, $n_{CS} = 6 \times 10^{8}$ cm^{-3}, but due to the large radius, the pressure from the supernova is spread over a larger area, so that the shock velocity is only 1,400 km s^{-1}, and thus the shock temperature $T \sim 3 \times 10^{7}$ K is much cooler than the previous super-luminous examples, resulting in softer X-ray photons of a few keV. The resulting radiative shock produces a respectable pre-absorption luminosity of roughly 7×10^{42} erg s^{-1} for half a year, converting 10% of the SN explosion energy into radiation. However, the column density is 10^{24} cm^{-2} like before, but now the ionization parameter is only $\xi \sim 30$, and can only partially ionize the intermediate elements. Therefore, during most of the 160 days it takes for the radiative shock to traverse the CSM shell, the X-ray flux will suffer heavy photoelectric absorption, and we will not see a rise in luminosity until the shock nears the end of the shell, after which the shock will cool in a matter of days.

Hence, these intrinsically luminous radiative shocks dominated by line-emission may have long underlying durations, but their actual observable durations are typically short.

Modest line-emission from non-radiative shocks

In this example, the CSM shell has a mass of $0.5M_{\odot}$, radius of 2×10^{17} cm, and thickness of 10^{15} cm, reaching a pre-shock density of 10^{6} cm^{-3}. The optical depth is only $\tau = 7 \times 10^{-4}$, i.e. the column density is 10^{21} cm^{-2}; this is much less than the previous examples, but the shock temperature here is only 1.4×10^{7} K, so the X-ray emission is soft, and much of it will still be absorbed. Therefore, the peak luminosity of 9×10^{40} erg

s^{-1} will not be observable until the shock traverses the entire shell. However, it takes the shocked shell material over half a year to cool, so the shocked CSM shell will emit for this length of time even after the shock has left the shell, making it easily observable.

6.4.2 Short duration events

Super-luminous flares?

If the CSM shell has a mass of $0.05M_{\odot}$, radius of 2×10^{15} cm, and thickness of 10^{14} cm, reaching a pre-shock density of 10^{10} cm^{-3}, the X-ray luminosity from the resulting shock reaches a staggering 5×10^{44} erg s^{-1}, but only lasts for 1 day, liberating $\sim 5\%$ of the SN explosion energy. The shock velocity reaches 10^4 km s^{-1}, and t_{eq} is only 1/10 the duration of this event, so electron temperatures of 10^9 K will be reached rapidly; this proposed class of events will generally produce extremely hard X-rays with a Bremsstrahlung spectrum.

In reality, the spherical symmetry of the CSM shell is likely to be broken. For instance, if the radii of the CSM shell at different locations varies by a factor of 2, the emission would be spread over a month, reaching less extreme luminosities of $\sim 10^{43}$ erg s^{-1}.

Luminous cool flares?

It is possible for a radiative shock to generate a luminous X-ray flare powered by line-emission, albeit at lower luminosities than before. For example, consider a CSM shell with mass $0.2M_{\odot}$, radius 2×10^{16} cm, and thickness 10^{14} cm; the pre-shock

density is still high 10^9 cm^{-3}, but the shock velocity is only 1,600 km s^{-1}, resulting in a characteristic photon energy of only ~ 3 keV. The luminosity reached for these events can be $\sim 10^{43}$ erg s^{-1}, however, the column density is typically large $\gtrsim 5 \times 10^{22}$ cm^{-2}, with the ionization parameter $\xi < 10^2$ insufficient to ionize the unshocked shell material. Hence, the full luminosity can be observed for only a few days, when the shock reaches the end of the CSM shell.

6.5 Simulation

To investigate the time evolution of the supernova shock interacting with the ejected circumstellar shell, we performed hydrodynamical simulations including a time dependent ionization calculation. The simulated systems were chosen to have luminous, adiabatic shocks in the CSM shell, where strong radiative cooling is not important for the hydrodynamics. We employed the numerical hydrodynamics code VH-1 (e.g. Blondin & Lundqvist 1993) using the nonequilibrium ionization calculation similar to that discussed in Patnaude et al. (2009) but without the diffusive shock acceleration calculation.

The supernova ejecta is modeled as a powerlaw in velocity ($\rho_{\rm ej} \propto v^{-n_{ej}}$) with a flat inner density profile (Truelove & McKee 1999), which interacts with a circumstellar wind within the CSM shell. Except for one model, the supernova ejecta mass is set at 4M$_\odot$, the explosion energy is $2{\times}10^{51}$ erg, the ejecta powerlaw index is $n_{ej} = 10$, and the CSM shells span a range of masses (0.1 – 1.0M$_\odot$) and thicknesses (10^{14} – 10^{15} cm), with a fixed CSM shell radius of 10^{16} cm. The circumstellar wind is derived from a progenitor mass-loss rate of $\dot{M} = 2{\times}10^{-5}$ M$_\odot$ yr^{-1} with a wind velocity of 10 km s^{-1}. Shells at distances much greater than 10^{16} cm would produce X-ray emission at later times than

considered here. The simulation models the interaction between 10 days and 0.8 yr after the supernova. The upper limit on the timescale allows for the shock to fully traverse the CSM shell.

We compute the 0.5 – 30.0 keV thermal X-ray emission as a function of time to compare against the results depicted in Figures 6.1 to 6.6, as well as some of the adiabatic shock scenarios described in Section 6.4. We plot the unabsorbed and absorbed luminosity versus time for several models in Figure 6.7. Models where the total radiated X-ray luminosity exceeds the supernova kinetic energy were discarded; these models have strong radiative shocks, outside the regime of validity for our simulation code.

The luminosities seen in Figure 6.7 are in general agreement with the predictions from the simple theory of Section 6.3, although the peak luminosity of the simulations can exceed the predicted luminosity by a factor of ~ 5. The discrepancy is most likely due to the fact that the CSM shell mass in these simulations were small compared with the SN ejecta mass, and so the supernova energy may not be thermalized inside the CSM shell at the time of impact, but thermalization is assumed in our simple analytical models of Section 6.3. The shock velocity in the shell declines slowly with time in the numerical simulations, which support the assumption of constant shock velocity in our analytical model. As shown in Figure 6.7, luminous X-ray emission with $L_X \approx 10^{42-44}$ erg s^{-1} is attained once the blastwave hits the shell. Most models show a fast rise in emission once the blastwave impacts the shell, followed by a slow decline.

The super-luminous non-radiative shock discussed in the 3rd paragraph of Section 6.4.1 is also plotted in Figure 6.7. Compared with the other simulated systems, here a lower mass CSM shell is placed closer to the star, but the shell is thicker. This results in

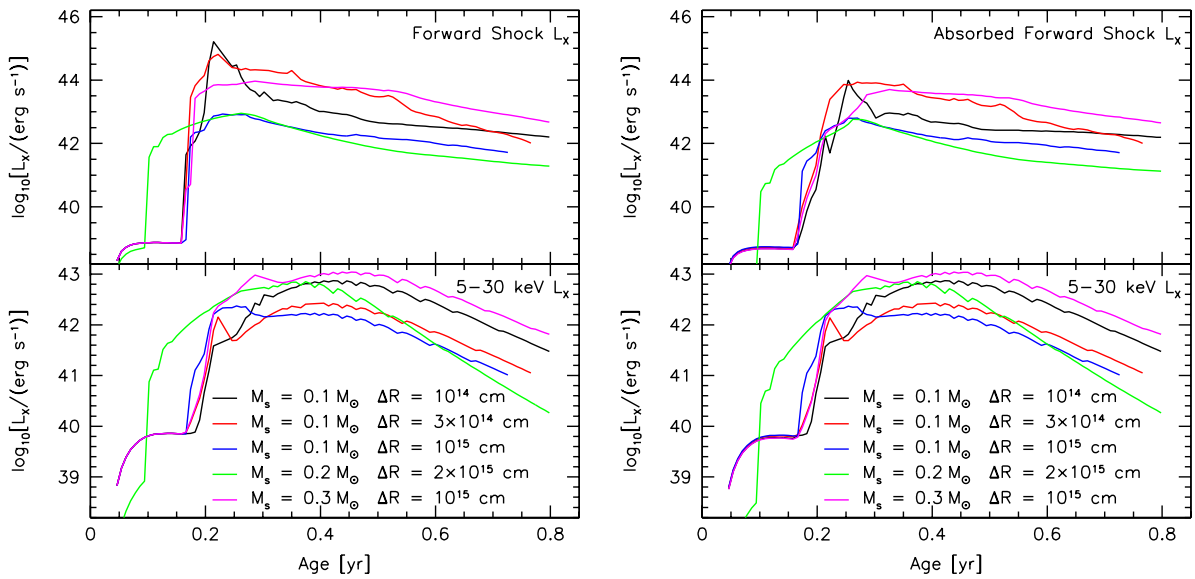

Figure 6.7.— *Left*: In the upper panel, we show the X-ray emission (0.5–30 keV) as a function of time from material swept up by the supernova forward shock. In the lower panel, we plot the 5–30 keV emission as a function of time. This includes contributions from the forward shock as well as a negligible contribution from reverse-shocked ejecta. *Right*: The same as in the left panel, except that we include photoelectric absorption from unshocked circumstellar material, including the unshocked CSM shell.

a longer rise time in emission (once the blastwave hits the shell, at around 0.15 yr). This model also contains half the explosion energy as the other models, and the blastwave transits across the shell for a longer period of time.

Our model also computes the detailed thermal X-ray emission out to 30 keV. In Figure 6.8, we show the X-ray emission at the point when the shocks break out of the circumstellar shells. The overall normalization, spectral lines, and line ratios differ significantly between these two models. The shape of the underlying continua also show differences, particularly above 10 keV where the model with the thicker shell shows a steeper spectrum at high energies (though appears flatter than the model with the thin shell at low energies). While the spectral resolution and throughput of current X-ray observatories may not be able to discriminate between these models, high spectral resolution missions such as *Astro-H* may be able to.

6.6 Discussion

Our simple formulas are in rough agreement with other predictions in literature. Adapting our formulas with a filling factor for clouds in the wind-blown CSM of SN 1986J (Chugai 1993), we arrive at similar luminosities and shock temperatures as observed. For SN 1987A, our model agrees exactly with the luminosity $L = 4 \times 10^{38}$ erg s^{-1} predicted by Chevalier & Liang (1989) for the collision of the SN 1987A's ejecta with its circumstellar ring (with $M_1 = 0.1$, R_{17}=5, $\Delta R_{15} = 1.6$); but only $L \sim 10^{35}$ erg s^{-1} was actually observed (Burrows et al. 2000), probably due to the drastic difference between the spherical geometry of our models versus the shape of the ring. As for possible super-luminous X-rays from SN CSM interactions, Terlevich et al. (1992) studied

the interaction of supernova with a uniform circumstellar medium of $n \sim 10^7$ cm^{-3} as the basis of a starburst model for active galactic nuclei, and found that the supernova quickly becomes strongly radiative, with most of the X-ray emission coming from the forward shock, which may reach a bolometric luminosity of 10^{43} erg s^{-1}, consistent with our findings for CSM shells.

Among the most luminous X-ray SNe ever detected includes SN 2010jl, which was inferred to have an unabsorbed luminosity of $L_X \sim 7 \times 10^{41}$ erg s^{-1}, most likely from the forward shock front at $\sim 10^{15}$ cm (Chandra et al. 2012b). However, the actual observed luminosity was initially only 20% of the unabsorbed luminosity, at least during an early epoch, as the column density was immense: $\sim 10^{24}$ cm^{-2}. Several other SNe have been observed to have X-ray luminosities of a few 10^{41} erg s^{-1} more than a year post explosion, for example SN 2008iy (Miller et al. 2010), SN 1995N (Fox et al. 2000), and SN 1988Z (Aretxaga et al. 1999); in particular, SN 1988Z may have radiated $\sim 50\%$ of its total explosion energy in X-rays in just 10 years, confirming that a dense CSM can convert a large fraction of the kinetic energy of a SN into X-ray radiation. Indeed, the X-ray light curves of all observed X-ray SNe found in literature had peak luminosities ranging from 10^{37} to almost 10^{42} erg s^{-1} (Dwarkadas & Gruszko 2012), which may be puzzling given our calculation that 10^{43} to 10^{44} erg s^{-1} X-ray luminosities with durations of several months are theoretically allowed even with modest explosion energies of 10^{51} erg, albeit contingent on the existence of a CSM shell and some fine-tuning of the shell parameters. But, almost all of these X-ray SNe were observed below 10 keV, whereas most luminous X-ray events proposed here are driven by fast forward shocks that can reach temperatures of $T \sim 10^9$ K, so before the shock escapes the CSM shell, many unabsorbed X-ray photons from the early emission will have energies > 10 keV.

Therefore, the newly launched NuSTAR space telescope, which can observe up to 80 keV, may be better suited for capturing super-luminous X-ray SNe during early CSM interactions compared with previous satellites. Although the Burst Alert Telescope on Swift can also observe up to 150 keV, its poor sensitivity allows it to see 10^{44} erg s^{-1} objects only out to $\sim$10 Mpc.

Moreover, the event rate of our proposed super-luminous X-ray SNe should be comparable to the rate of optically super-luminous SNe powered by strong shocks from ejecta-CSM interactions, i.e. $\lesssim 10^{-8}$ Mpc^{-3} yr^{-1}; given their scarcity, we were not disconcerted by the lack of reported detections in literature. However, after we submitted our paper and posted it on ArXiv, Levan et al. (2013) revealed analysis of X-ray observations of SCP 06F6 that showed it is likely the brightest X-ray supernova ever observed, with $L_X \sim 10^{45}$ erg s^{-1}. It is plausible the super-luminous X-ray emission from SCP 06F6 may be powered by converting a significant fraction of $\sim 10^{52}$ erg of explosion energy via the interaction of SN ejecta with a dense CSM, consistent with the fact that SCP 06F6 was also an optically super-luminous SN.

If the supernova ejecta collides with a dense CSM shell, the shell acts as a wall, resulting in a high reverse shock velocity of $\approx v_{SN} - v_s$. When the energy initially transmitted into the shell is small, the solutions for the reverse shock have a self-similar nature, and were first solved by Chevalier & Liang (1989). As the CSM shells in our super-luminous scenarios tend to be much denser than the cavity within (even if the SN ejecta mass is included and averaged over the cavity), it is likely the luminosity of the forward shock running in the CSM shell will dominate the reverse shock retreating into the cavity; furthermore, the reverse shock emission is subject to heavy absorption from the cold, dense shell that condenses between the forward and reverse shocks.

Optical and X-ray emission, interpreted as generated from interactions between SNe ejecta and CS material (or between two ejected shells) have already been used to provide indirect evidence for the explosive ejection of massive CSM shells a few years prior to the supernova, e.g. SN 1994W (Chugai et al. 2004; Dessart et al. 2009). Several observed SNe have a CSM density that seemed to increase with distance from the progenitor: SN 2008iy (Miller et al. 2010), SN 1996cr (Bauer et al. 2008), SN 2001em (Chugai & Chevalier 2006; Schinzel et al. 2009), and SN 2011ja (Chakraborti et al. 2013), suggesting that at least at certain radii, the CSM may be better modeled as a CSM shell rather than a smooth r^{-2} wind (Fox et al. 2013). Also, some of the ultra-luminous X-ray (ULX) sources with luminosities up to $\sim 10^{41}$ erg s^{-1}, especially the ones with a thermal spectrum and slow variability, may be due to supernova interacting with massive cirumstellar shells (Swartz et al. 2004).

Aside from converting the kinetic energy of expanding ejecta into radiation upon collision with a massive CSM shell, there is another main mechanism invoked to power super-luminous supernova. In this mechanism, the SNe explosion launches a shock wave from the center of the star, with the shock heating the material it crosses as the shock travels outward, until the shock escapes at a radius where the material is no longer optically thick to radiation. More specifically, this *shock breakout* occurs when the photon diffusion timescale becomes shorter than the dynamical timescale of the shock, corresponding to an optical depth of $\tau \simeq c/v_s$ (Weaver 1976); for super-luminous supernova, this edge is at least an order-of-magnitude greater than the edge of the gravitationally-bound progenitor star. Then, the thermal energy deposited by the shock is gradually emitted as photons diffuse out, analogous to regular Type II-P SNe (Gal-Yam 2012).

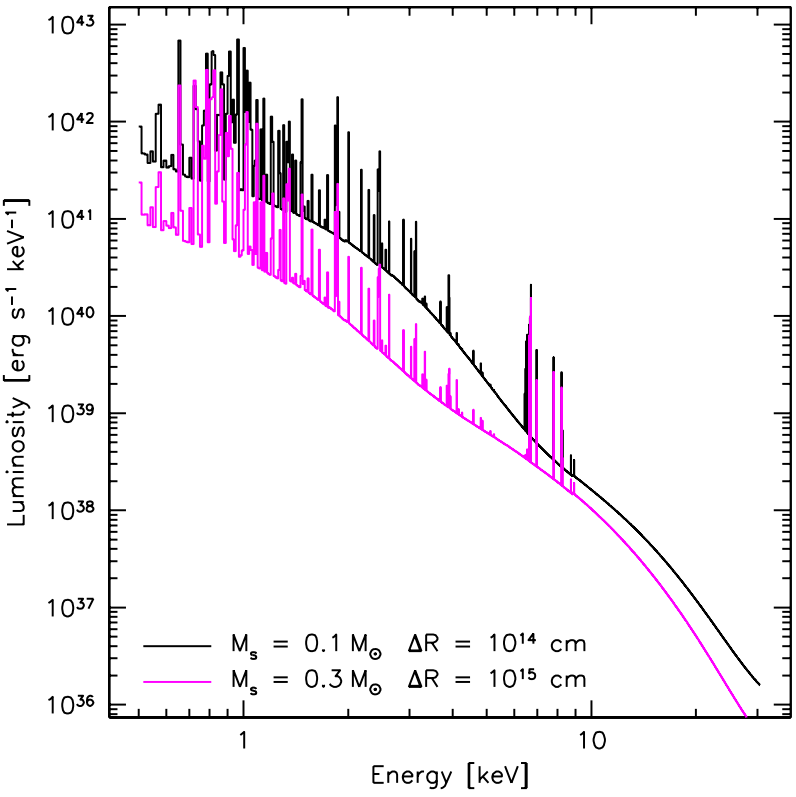

Figure 6.8.— 0.5–30 keV thermal X-ray emission for two models shown in Figure 6.7, when the shocks break out of the CSM shells at approximately 0.4 and 0.55 yr, respectively. The black curve corresponds to the model with $M_s = 0.1 M_\odot$ and $\Delta R_s = 10^{14}$ cm, while the magenta curve corresponds to the model with $M_s = 0.3 M_\odot$ and $\Delta R_s = 10^{15}$ cm.

Many ways have been proposed to explain the large effective radii required for superluminous light curves powered via shock breakout, including massive & optically-thick stellar winds (Ofek et al. 2010; Chevalier & Irwin 2011; Moriya & Tominaga 2012; Moriya et al. 2013), or massive & optically-thick shells ejected in prior eruptions (Smith & McCray 2007; Miller et al. 2009) – assuming that the circumstellar material is optically thick all the way to the CSM shell. A shock breakout in such environments could also produce X-ray emission (Balberg & Loeb 2011; Katz et al. 2011; Chevalier & Irwin 2012; Svirski et al. 2012), and searches for such events have been conducted (Ofek et al. 2013b). The unabsorbed X-ray emission from these shock breakouts can also reach incredible luminosities $\sim 10^{44}$ erg s^{-1}, however, the luminosity after shock breakout tends to decline quickly with time, whereas the X-ray emission from optically-thin CSM shell interactions can increase for an extended period of time as the shock runs through and superheats more of the shell. The collision of SN ejecta with massive CSM shells can also emit much larger total energies in X-rays. Furthermore, the delay between the optical SN and the X-ray emission is much shorter for shock breakouts.

A non-thermal power-law population of relativistic electrons may be accelerated by the shock. These could inverse-Compton scatter soft photons and also emit in optical and UV up to X-rays and high energy γ-rays. The X-rays from this inverse-Compton component is likely negligible compared to the luminous X-ray emission from the forward shock running through a dense CSM shell considered in this paper, as the former scales with density while the latter scales with density squared; Chevalier & Fransson (2006) found that during the plateau phase of a Type IIP SN, when the optical flux of the supernova is still $\sim 10^{42}$ erg s^{-1}, the inverse Compton X-ray emission is less than 10^{37} erg s^{-1}, and will further decrease with time as the soft photon flux diminishes. We should

also mention the possibility that the collision of SNe ejecta with massive CSM shells can serve as potential cosmic-ray accelerators (Murase et al. 2011).

Acknowledgments

We thank Sayan Chakraborti, Manos Chatzopoulos, Raffaella Margutti, Takashi Moriya, John Raymond, and Randall Smith for useful discussions. TP was supported by the Hertz Foundation and the National Science Foundation via a graduate research fellowship. This work was supported in part by NSF grant AST-0907890 and NASA grants NNX08AL43G and NNA09DB30A.

Chapter 7

Conclusions and Future Directions

What are the near term prospects for actually verifying or falsifying the predictions in this thesis with observations?

A preliminary search for very massive stars (VMS) of mass $150M_{\odot}$ to $600M_{\odot}$ in young, dense star clusters, via their eclipse by a binary companion, was conducted by the scientists at the Palomar Transient Factory (PTF). About half of our proposed clusters had already been visited by PTF; cluster host galaxies NGC 4214 and NGC 4449 had already been observed ~ 100 times each, while star cluster NGC 604 in M33 had been visited over 700 times. We especially thank Dr. Frank Masci for performing most of the photometry and light curve analysis with his image differencing pipeline; we are grateful to Profs. Tom Prince and Shri Kulkarni for their insights, and thank David Levitan for setting up the collaboration. Unfortunately, although the existing temporal coverage from PTF for some of our target clusters was promising, no evidence for transits were seen above and beyond that expected from residuals in the instrumental calibration and point-spread-function matching of the survey images.

One anticipated issue was that the optical flux from a VMS is a small fraction of its total bolometric flux, since the VMS is incredibly hot (T$\sim$ 50,000 K) – so extracting a transit signal is more difficult at the red wavebands used in these PTF observations. Even if we ignored all the systematic noise, and only considered the contaminating cluster background light, with only 60 second exposures on a 1.2 m telescope used by PTF, it is difficult to get enough signal-to-noise (e.g. 5σ) to detect eclipses depths that are smaller than $\sim$25%. So given the short integration time, we needed a particularly massive secondary star to transit the VMS primary, e.g. an $\sim 100 M_{\odot}$ companion, instead of a more typical $\sim 15 M_{\odot}$ B-star companion, but the odds of the former were far less favorable. Future attempts at finding a VMS via transits could be conducted with targeted observations, e.g. 30 minute exposures per cluster every day over 10 days with a 2-meter ground telescope; future wide-field synoptic surveys such as Pan-STARRS and the Large Synoptic Survey Telescope may find our proposed signal automatically.

Since the publication of our paper on pair-instability supernovae (PISNe) from the collision runaway merger product in young, dense star clusters, other low redshift PISNe and pulsational-PISN candidates have been identified, e.g. PTF 11hrq (private communication with Ofer Yaron), SN 2010hy (Vinko et al. 2010), possibly SN 2009ip (Fraser et al. 2013), and also the two most distant supernova ever discovered at $z = 2.05$ and $z = 3.90$ (Cooke et al. 2012). The observed PISN event rates at low redshifts are so far consistent with our predictions, however, the implied PISN rate from the two high redshift events observed by Cooke et al. (2012) is a factor of $\sim$ 10 times greater than that expected from progenitors formed by multiple stellar collisions in young star clusters. This discrepancy hints that at $z > 2$, the most massive end of the stellar initial mass function is growing, perhaps due to pockets of pristine gas still left over from the

Big Bang to form Pop III stars, which are thought to have a top-heavy mass function. So Cooke et al. (2012) might have seen the first ever supernova associated with the hypothesized first generation of stars!

Without techniques such as our proposed eclipsing binary method, a VMS is extremely difficult to identify. Unresolved multiple systems have often been confused with a single VMS due to their large luminosities and crowded environments (Sana & Evans 2011). Also, as the effective brightness temperature of stars above 100 $M_{\odot}$ stays constant (Bromm et al. 2001; Schaerer 2002), it is difficult to spectroscopically distinguish a VMS from smaller candidates. However, the progenitors of PISNe must have a minimum mass of $140M_{\odot}$ in pristine environments (Heger & Woosley 2002), or well above 250 $M_{\odot}$ in enriched environments (Yungelson et al. 2008). Therefore, PISNe offer a rare opportunity to unambiguously identify very massive stars and their immediate environments. An accurate localization of PISNe within their often small and faint host galaxies will enable future missions with deeper imaging capabilities to characterize the specific environment of the SN, and test predictions such as our theorized association of low redshift PISNe with dense star clusters. Once the SN fades, super star clusters with $M_{AB} \approx -10$ are detectable with ultra-deep fields with the Hubble Space Telescope (HST) even at $z \sim 0.1$, and more modest clusters considered in Chapter 3 are observable with the James Webb Space Telescope (JWST) due for launch in 2018.

However, PISNe are the rarest type of SNe known, with volumetric rates of $\sim 10^{-9}$ Mpc^{-3} yr^{-1}, and only $\lesssim 1$ new event is discovered every year. So to amass an useful sample of PISNe, we need to localize targets ***now***, before these SNe fade away, and well before future missions with deeper imaging capabilities are launched. To this end, under the leadership of Dr. Ofer Yaron, we are co-investigators for the approved HST Cycle 20

proposal to conduct late-time photometry of the pair-instability supernova PTF 10nmn, in order to characterize its host properties, and record its precise location. We are also co-investigators on a similar HST Cycle 21 proposal for the candidate PISN event PTF 11hrq. Hopefully these will be fruitful investments of HST's survey time.

As for our predictions regarding the rates and detectability of supernova from the Epoch of Reionization – from the intrinsically brightest events such as PISNe to the dimmest core-collapse supernovae magnified via gravitational lensing, and their utility as cosmological probes – these predictions require the launch of JWST before they can be tested.

More immediately, for our prediction of super-luminous X-ray transients associated with supernova, powered by the interaction of SN ejecta with dense circumstellar shells, the advent of wide-field transient surveys already established today such as PTF and Pan-STARRS1 have greatly increased the number of supernovae detected, some of which have been shown to take place in dense and uneven circumstellar environments via multi-wavelength supernova forensics. Most importantly, after we submitted our paper and posted it on ArXiv, Levan et al. (2013) revealed analysis of X-ray observations of SCP 06F6, showing it is likely the first super-luminous X-ray supernova ever observed, with $L_X \sim 10^{45}$ erg s^{-1}, possibly confirming our prediction. With the recent launch of the Nuclear Spectroscopic Telescope Array in 2012, which is well suited for the hard X-ray emission predicted for these super-luminous events, the prospect of detecting more events in this new class of transients in the near future is promising.

References

Andersen, M., Zinnecker, H., Moneti, A., McCaughrean, M. J., Brandl, B., Brandner, W., Meylan, G., & Hunter, D. 2009, ApJ, 707, 1347

Aretxaga, I., Benetti, S., Terlevich, R. J., Fabian, A. C., Cappellaro, E., Turatto, M., & della Valle, M. 1999, MNRAS, 309, 343

Balberg, S., & Loeb, A. 2011, MNRAS, 414, 1715

Barkat, Z., Rakavy, G., & Sack, N. 1967, Physical Review Letters, 18, 379

Bastian, N. 2008, MNRAS, 390, 759

Bauer, F. E., Dwarkadas, V. V., Brandt, W. N., Immler, S., Smartt, S., Bartel, N., & Bietenholz, M. F. 2008, ApJ, 688, 1210

Beers, T. C., & Christlieb, N. 2005, ARA&A, 43, 531

Belkus, H., Van Bever, J., & Vanbeveren, D. 2007, ApJ, 659, 1576

Blanton, M. R., et al. 2003, ApJ, 592, 819

Blondin, J. M., & Lundqvist, P. 1993, ApJ, 405, 337

Bloom, J. S., et al. 2012, ApJ, 744, L17

Bonanos, A. Z. 2009, ApJ, 691, 407

Bonanos, A. Z. 2012, in IAU Symposium, Vol. 282, IAU Symposium, 27–32

Bosch, G., Terlevich, E., & Terlevich, R. 2009, AJ, 137, 3437

Bouwens, R., et al. 2012, ArXiv e-prints

Bouwens, R. J., et al. 2011a, Nature, 469, 504

—. 2011b, ArXiv e-prints

—. 2011c, ApJ, 737, 90

Brandt, T. D., Tojeiro, R., Aubourg, É., Heavens, A., Jimenez, R., & Strauss, M. A. 2010, AJ, 140, 804

Bromm, V., Kudritzki, R. P., & Loeb, A. 2001, ApJ, 552, 464

Bromm, V., & Larson, R. B. 2004, ARA&A, 42, 79

Bromm, V., & Loeb, A. 2003, Nature, 425, 812

Burrows, D. N., et al. 2000, ApJ, 543, L149

Cappa, C., Goss, W. M., & van der Hucht, K. A. 2004, AJ, 127, 2885

Cassinelli, J. P., Mathis, J. S., & Savage, B. D. 1981, Science, 212, 1497

Cen, R. 2010, ApJ, 725, 115

Chakraborti, S., et al. 2013, ArXiv e-prints

Chandra, P., Chevalier, R. A., Chugai, N., Fransson, C., Irwin, C. M., Soderberg, A. M., Chakraborti, S., & Immler, S. 2012a, ApJ, 755, 110

Chandra, P., Chevalier, R. A., Irwin, C. M., Chugai, N., Fransson, C., & Soderberg, A. M. 2012b, ApJ, 750, L2

Chatzopoulos, E., & Wheeler, J. C. 2012, ApJ, 760, 154

Chen, K., Heger, A., & Almgren, A. S. 2011, Computer Physics Communications, 182, 254

Chevalier, R. A. 1982a, ApJ, 258, 790

—. 1982b, ApJ, 259, 302

Chevalier, R. A., & Fransson, C. 1994, ApJ, 420, 268

Chevalier, R. A., & Fransson, C. 2003, in Lecture Notes in Physics, Berlin Springer Verlag, Vol. 598, Supernovae and Gamma-Ray Bursters, ed. K. Weiler, 171–194

—. 2006, ApJ, 651, 381

Chevalier, R. A., & Irwin, C. M. 2011, ApJ, 729, L6

—. 2012, ApJ, 747, L17

Chevalier, R. A., & Liang, E. P. 1989, ApJ, 344, 332

Chiappini, C., Frischknecht, U., Meynet, G., Hirschi, R., Barbuy, B., Pignatari, M., Decressin, T., & Maeder, A. 2011, Nature, 472, 454

Chini, R., Hoffmeister, V. H., Nasseri, A., Stahl, O., & Zinnecker, H. 2012, ArXiv e-prints

Chomiuk, L., et al. 2011, ApJ, 743, 114

Chugai, N. N. 1993, ApJ, 414, L101

Chugai, N. N., & Chevalier, R. A. 2006, ApJ, 641, 1051

Chugai, N. N., et al. 2004, MNRAS, 352, 1213

Clark, P. C., Glover, S. C. O., Klessen, R. S., & Bromm, V. 2011, ApJ, 727, 110

Coe, D., et al. 2013, ApJ, 762, 32

Cooke, J., et al. 2012, Nature, 491, 228

Cooke, R., Pettini, M., Steidel, C. C., Rudie, G. C., & Jorgenson, R. A. 2011, MNRAS, 412, 1047

Crowther, P. A., Schnurr, O., Hirschi, R., Yusof, N., Parker, R. J., Goodwin, S. P., & Kassim, H. A. 2010, MNRAS, 408, 731

Davidson, K., & Humphreys, R. M., eds. 2012, Astrophysics and Space Science Library, Vol. 384, Eta Carinae and the Supernova Impostors

De Donder, E., & Vanbeveren, D. 2003, New Astronomy, 8, 415

de Grijs, R., Gilmore, G. F., Mackey, A. D., Wilkinson, M. I., Beaulieu, S. F., Johnson, R. A., & Santiago, B. X. 2002, MNRAS, 337, 597

de Jager, C., Nieuwenhuijzen, H., & van der Hucht, K. A. 1988, A&AS, 72, 259

Dessart, L., Hillier, D. J., Gezari, S., Basa, S., & Matheson, T. 2009, MNRAS, 394, 21

Diaz-Cordoves, J., Claret, A., & Gimenez, A. 1995, A&AS, 110, 329

Dwarkadas, V. V. 2005, ApJ, 630, 892

Dwarkadas, V. V., & Gruszko, J. 2012, MNRAS, 419, 1515

Ebisuzaki, T., et al. 2001, ApJ, 562, L19

Eggleton, P. P. 1983, ApJ, 268, 368

Ekström, S., Meynet, G., Chiappini, C., Hirschi, R., & Maeder, A. 2008, A&A, 489, 685

Ellis, R. S., et al. 2013, ApJ, 763, L7

Fan, X., et al. 2006, AJ, 132, 117

Farrell, S. A., Webb, N. A., Barret, D., Godet, O., & Rodrigues, J. M. 2009, Nature, 460, 73

Figer, D. F. 2005, Nature, 434, 192

Figer, D. F., McLean, I. S., & Morris, M. 1999, ApJ, 514, 202

Foley, R. J., Smith, N., Ganeshalingam, M., Li, W., Chornock, R., & Filippenko, A. V. 2007, ApJ, 657, L105

Fosbury, R. A. E., et al. 2003, ApJ, 596, 797

Fox, D. W., et al. 2000, MNRAS, 319, 1154

Fox, O. D., Filippenko, A. V., Skrutskie, M. F., Silverman, J. M., Ganeshalingam, M., Cenko, S. B., & Clubb, K. I. 2013, ArXiv e-prints

Franco, J., Melnick, J., Terlevich, R., Tenorio-Tagle, G., & Rozyczka, M. 1993, in Star Formation, Galaxies and the Interstellar Medium, ed. J. Franco, F. Ferrini, & G. Tenorio-Tagle, 149

Fraser, M., et al. 2013, ArXiv e-prints

Freitag, M., Gürkan, M. A., & Rasio, F. A. 2006, MNRAS, 368, 141

Frost, M. I., Surace, J., Moustakas, L. A., & Krick, J. 2009, ApJ, 698, L68

Fryer, C. L. 1999, ApJ, 522, 413

Fukugita, M., Hogan, C. J., & Peebles, P. J. E. 1998, ApJ, 503, 518

Fumagalli, M., O'Meara, J., & Prochaska, J. 2011, Science, 334, 1245

Furlanetto, S. R., & Loeb, A. 2003, ApJ, 588, 18

Gal-Yam, A. 2012, Science, 337, 927

Gal-Yam, A., & Leonard, D. C. 2009, Nature, 458, 865

Gal-Yam, A., et al. 2007, ApJ, 656, 372

—. 2009, Nature, 462, 624

Gieles, M., Larsen, S. S., Scheepmaker, R. A., Bastian, N., Haas, M. R., & Lamers, H. J. G. L. M. 2006, A&A, 446, L9

Glebbeek, E., Gaburov, E., de Mink, S. E., Pols, O. R., & Portegies Zwart, S. F. 2009, A&A, 497, 255

Graur, O., et al. 2011, MNRAS, 417, 916

Greif, T., Springel, V., White, S., Glover, S., Clark, P., Smith, R., Klessen, R., & Bromm, V. 2011, ArXiv e-prints

Greif, T. H., Johnson, J. L., Klessen, R. S., & Bromm, V. 2008, MNRAS, 387, 1021

Gunnarsson, C., & Goobar, A. 2003, A&A, 405, 859

Gürkan, M. A., Freitag, M., & Rasio, F. A. 2004, ApJ, 604, 632

Guseva, N. G., Papaderos, P., Meyer, H. T., Izotov, Y. I., & Fricke, K. J. 2009, A&A, 505, 63

Haiman, Z. 2009, Observing the First Stars and Black Holes, ed. Thronson, H. A., Stiavelli, M., & Tielens, A., 385–+

Hamann, W.-R., Gräfener, G., & Liermann, A. 2006, A&A, 457, 1015

Heger, A., & Woosley, S. E. 2002, ApJ, 567, 532

Hillebrandt, W., & Niemeyer, J. C. 2000, ARA&A, 38, 191

Horiuchi, S., Beacom, J. F., Kochanek, C. S., Prieto, J. L., Stanek, K. Z., & Thompson, T. A. 2011, ApJ, 738, 154

Hosokawa, T., Omukai, K., Yoshida, N., & Yorke, H. 2011, Science, 334, 1250

Hummel, J. A., Pawlik, A. H., Milosavljević, M., & Bromm, V. 2012, ApJ, 755, 72

Hunter, D. A., Shaya, E. J., Holtzman, J. A., Light, R. M., O'Neil, Jr., E. J., & Lynds, R. 1995, ApJ, 448, 179

Iwamoto, N., Umeda, H., Tominaga, N., Nomoto, K., & Maeda, K. 2005, Science, 309, 451

Joggerst, C. C., Almgren, A., Bell, J., Heger, A., Whalen, D., & Woosley, S. E. 2010, ApJ, 709, 11

Joggerst, C. C., & Whalen, D. J. 2011, ApJ, 728, 129

Kallrath, J., & Milone, E. F. 2009, Eclipsing Binary Stars: Modeling and Analysis

Karlsson, T., Johnson, J. L., & Bromm, V. 2008, ApJ, 679, 6

Kasen, D. 2006, ApJ, 649, 939

Kasen, D., & Bildsten, L. 2010, ApJ, 717, 245

Kasen, D., Thomas, R. C., & Nugent, P. 2006, ApJ, 651, 366

Kasen, D., & Woosley, S. E. 2009, ApJ, 703, 2205

Kasen, D., Woosley, S. E., & Heger, A. 2011, ApJ, 734, 102

Katz, B., Sapir, N., & Waxman, E. 2011, ArXiv e-prints

Kessler, R., et al. 2010, PASP, 122, 1415

Kiewe, M., et al. 2012, ApJ, 744, 10

King, I. R. 1966, AJ, 71, 64

Kirby, E. N., Simon, J. D., Geha, M., Guhathakurta, P., & Frebel, A. 2008, ApJ, 685, L43

Komatsu, E., et al. 2011, ApJS, 192, 18

Koumpia, E., & Bonanos, A. Z. 2011, in IAU Symposium, Vol. 272, IAU Symposium, ed. C. Neiner, G. Wade, G. Meynet, & G. Peters, 515–516

Krauss, L. M. 1987, Nature, 329, 689

Kudritzki, R. P. 2002, ApJ, 577, 389

Labbé, I., et al. 2010a, ApJ, 716, L103

—. 2010b, ApJ, 708, L26

Lamontagne, R., Moffat, A. F. J., Drissen, L., Robert, C., & Matthews, J. M. 1996, AJ, 112, 2227

Langer, N. 1989, A&A, 220, 135

—. 2009, Nature, 462, 579

Langer, N., Norman, C. A., de Koter, A., Vink, J. S., Cantiello, M., & Yoon, S.-C. 2007, A&A, 475, L19

Larsen, S. S. 2004, A&A, 416, 537

—. 2009, A&A, 494, 539

Larson, R. B. 1982, MNRAS, 200, 159

—. 2003, Reports on Progress in Physics, 66, 1651

Levan, A. J., Read, A. M., Metzger, B. D., Wheatley, P. J., & Tanvir, N. R. 2013, ArXiv e-prints

Loeb, A. 2010, How Did the First Stars and Galaxies Form?, ed. Loeb, A.

Lou, Y.-Q., & Wu, Y. 2012, MNRAS, 422, L28

LSST Science Collaborations et al. 2009, ArXiv e-prints

Mac Low, M.-M., & Ferrara, A. 1999, ApJ, 513, 142

Mackey, A. D., & Gilmore, G. F. 2003, MNRAS, 338, 85

Mackey, J., Bromm, V., & Hernquist, L. 2003, ApJ, 586, 1

Maíz-Apellániz, J. 2001, ApJ, 563, 151

Maoz, D. 2010, in American Institute of Physics Conference Series, Vol. 1314, American Institute of Physics Conference Series, ed. V. Kologera & M. van der Sluys, 223–232

Maoz, D., & Badenes, C. 2010, MNRAS, 407, 1314

Maoz, D., Mannucci, F., & Brandt, T. D. 2012, MNRAS, 426, 3282

Marri, S., Ferrara, A., & Pozzetti, L. 2000, MNRAS, 317, 265

Martayan, C., Floquet, M., Hubert, A. M., Gutiérrez-Soto, J., Fabregat, J., Neiner, C., & Mekkas, M. 2007, A&A, 472, 577

Mason, B. D., Hartkopf, W. I., Gies, D. R., Henry, T. J., & Helsel, J. W. 2009, AJ, 137, 3358

Mauerhan, J. C., et al. 2012, ArXiv e-prints

McCrady, N., & Graham, J. R. 2007, ApJ, 663, 844

McMillan, S., & Portegies Zwart, S. 2004, ArXiv Astrophysics e-prints

Mesinger, A., Johnson, B. D., & Haiman, Z. 2006, ApJ, 637, 80

Meynet, G., Ekström, S., & Maeder, A. 2006, A&A, 447, 623

Miller, A. A., et al. 2009, ApJ, 690, 1303

—. 2010, MNRAS, 404, 305

Moriya, T., Tominaga, N., Tanaka, M., Maeda, K., & Nomoto, K. 2010, ApJ, 717, L83

Moriya, T. J., Blinnikov, S. I., Tominaga, N., Yoshida, N., Tanaka, M., Maeda, K., & Nomoto, K. 2013, MNRAS, 428, 1020

Moriya, T. J., & Tominaga, N. 2012, ApJ, 747, 118

Murase, K., Thompson, T. A., Lacki, B. C., & Beacom, J. F. 2011, Phys. Rev. D, 84, 043003

Nelemans, G., & van den Heuvel, E. P. J. 2001, A&A, 376, 950

Nomoto, K., Yamaoka, H., Shigeyama, T., Kumagai, S., & Tsujimoto, T. 1994, in Supernovae, ed. S. A. Bludman, R. Mochkovitch, & J. Zinn-Justin, 199–+

Nugis, T., & Lamers, H. J. G. L. M. 2000, A&A, 360, 227

Ofek, E. O., et al. 2010, ApJ, 724, 1396

—. 2013a, Nature, 494, 65

—. 2013b, ApJ, 763, 42

Owocki, S. P., Gayley, K. G., & Shaviv, N. J. 2004, ApJ, 616, 525

Pan, T., Kasen, D., & Loeb, A. 2012a, MNRAS, 422, 2701

Pan, T., Loeb, A., & Kasen, D. 2012b, MNRAS, 423, 2203

Patnaude, D. J., Ellison, D. C., & Slane, P. 2009, ApJ, 696, 1956

Phillips, M. M. 1993, ApJ, 413, L105

Planck Collaboration et al. 2013, ArXiv e-prints

Portegies Zwart, S. F., Baumgardt, H., McMillan, S. L. W., Makino, J., Hut, P., & Ebisuzaki, T. 2006, ApJ, 641, 319

Portegies Zwart, S. F., & McMillan, S. L. W. 2002, ApJ, 576, 899

Portegies Zwart, S. F., McMillan, S. L. W., & Gieles, M. 2010, ARA&A, 48, 431

Portegies Zwart, S. F., & van den Heuvel, E. P. J. 2007, Nature, 450, 388

Postman, M., et al. 2012, ApJS, 199, 25

Puls, J., Vink, J. S., & Najarro, F. 2008, A&A Rev., 16, 209

Puzia, T. H., Kissler-Patig, M., & Goudfrooij, P. 2006, ApJ, 648, 383

Quataert, E., & Shiode, J. 2012, MNRAS, 423, L92

Quimby, R. M., et al. 2011, Nature, 474, 487

Raiter, A., Fosbury, R. A. E., & Teimoorinia, H. 2010, A&A, 510, A109+

Rakavy, G., & Shaviv, G. 1967, ApJ, 148, 803

Raymond, J. C., Cox, D. P., & Smith, B. W. 1976, ApJ, 204, 290

Reddy, N. A., & Steidel, C. C. 2009, ApJ, 692, 778

Rest, A., et al. 2011, ApJ, 729, 88

Robertson, B. E., & Ellis, R. S. 2012, ApJ, 744, 95

Robertson, B. E., et al. 2013, ArXiv e-prints

Sabbi, E., et al. 2008, AJ, 135, 173

Sana, H., & Evans, C. J. 2011, in IAU Symposium, Vol. 272, IAU Symposium, ed. C. Neiner, G. Wade, G. Meynet, & G. Peters, 474–485

Scannapieco, E., & Bildsten, L. 2005, ApJ, 629, L85

Scannapieco, E., Madau, P., Woosley, S., Heger, A., & Ferrara, A. 2005, ApJ, 633, 1031

Scannapieco, E., Schneider, R., & Ferrara, A. 2003, ApJ, 589, 35

Schaefer, B. E., & Pagnotta, A. 2012, Nature, 481, 164

Schaerer, D. 2002, A&A, 382, 28

Schechter, P. 1976, ApJ, 203, 297

Scheepmaker, R. A., Haas, M. R., Gieles, M., Bastian, N., Larsen, S. S., & Lamers, H. J. G. L. M. 2007, A&A, 469, 925

Schinzel, F. K., Taylor, G. B., Stockdale, C. J., Granot, J., & Ramirez-Ruiz, E. 2009, ApJ, 691, 1380

Schneider, P., Ehlers, J., & Falco, E. E. 1992, Gravitational Lenses

Sgro, A. G. 1975, ApJ, 197, 621

Shaviv, N. J. 2000, ApJ, 532, L137

Sheth, R. K., & Tormen, G. 1999, MNRAS, 308, 119

Shull, J. M., Tumlinson, J., Giroux, M. L., Kriss, G. A., & Reimers, D. 2004, ApJ, 600, 570

Shull, J. M., & Venkatesan, A. 2008, ApJ, 685, 1

Smartt, S. J. 2009, ARA&A, 47, 63

Smith, N., Chornock, R., Li, W., Ganeshalingam, M., Silverman, J. M., Foley, R. J., Filippenko, A. V., & Barth, A. J. 2008, ApJ, 686, 467

Smith, N., Li, W., Silverman, J. M., Ganeshalingam, M., & Filippenko, A. V. 2011a, MNRAS, 415, 773

Smith, N., & McCray, R. 2007, ApJ, 671, L17

Smith, N., et al. 2011b, ApJ, 732, 63

Spitzer, L. 1962, Physics of Fully Ionized Gases

Stacy, A., Bromm, V., & Loeb, A. 2011, MNRAS, 142

Steidel, C. C., Pettini, M., & Adelberger, K. L. 2001, ApJ, 546, 665

Stolte, A., Brandner, W., Brandl, B., & Zinnecker, H. 2006, AJ, 132, 253

Suzuki, T. K., Nakasato, N., Baumgardt, H., Ibukiyama, A., Makino, J., & Ebisuzaki, T. 2007, ApJ, 668, 435

Svirski, G., Nakar, E., & Sari, R. 2012, ApJ, 759, 108

Swartz, D. A., Ghosh, K. K., Tennant, A. F., & Wu, K. 2004, ApJS, 154, 519

Tarter, C. B., Tucker, W. H., & Salpeter, E. E. 1969, ApJ, 156, 943

Terlevich, R., Tenorio-Tagle, G., Franco, J., & Melnick, J. 1992, MNRAS, 255, 713

Tornatore, L., Ferrara, A., & Schneider, R. 2007, MNRAS, 382, 945

Torres, G., Andersen, J., & Giménez, A. 2010, A&A Rev., 18, 67

Trac, H., & Cen, R. 2007, ApJ, 671, 1

Trenti, M., Stiavelli, M., & Michael Shull, J. 2009, ApJ, 700, 1672

Truelove, J. K., & McKee, C. F. 1999, ApJS, 120, 299

Tumlinson, J. 2007a, ApJ, 665, 1361

—. 2007b, ApJ, 664, L63

Úbeda, L., Maíz-Apellániz, J., & MacKenty, J. W. 2007, AJ, 133, 932

Vanbeveren, D., Belkus, H., van Bever, J., & Mennekens, N. 2009, Ap&SS, 324, 271

Vink, J. S., de Koter, A., & Lamers, H. J. G. L. M. 2000, A&A, 362, 295

—. 2001, A&A, 369, 574

Vinko, J., Wheeler, J. C., Chatzopoulos, E., Marion, G. H., & Caldwell, J. 2010, Central Bureau Electronic Telegrams, 2476, 1

Weaver, T. A. 1976, ApJS, 32, 233

Weidner, C., Kroupa, P., & Bonnell, I. A. D. 2010, MNRAS, 401, 275

Weigelt, G., & Baier, G. 1985, A&A, 150, L18

Weinmann, S. M., & Lilly, S. J. 2005, ApJ, 624, 526

Whalen, D. J., Joggerst, C. C., Fryer, C. L., Stiavelli, M., Heger, A., & Holz, D. E. 2012, ArXiv e-prints

Whalen, D. J., et al. 2013, ArXiv e-prints

Wise, J. H., & Abel, T. 2005, ApJ, 629, 615

Wood, K., & Loeb, A. 2000, ApJ, 545, 86

Woods, E., & Loeb, A. 1998, ApJ, 508, 760

Woosley, S. E., Blinnikov, S., & Heger, A. 2007, Nature, 450, 390

Woosley, S. E., Heger, A., & Weaver, T. A. 2002, Reviews of Modern Physics, 74, 1015

Young, D. R., et al. 2010, A&A, 512, A70

Yungelson, L. R., van den Heuvel, E. P. J., Vink, J. S., Portegies Zwart, S. F., & de Koter, A. 2008, A&A, 477, 223

Zackrisson, E., Rydberg, C.-E., Schaerer, D., Östlin, G., & Tuli, M. 2011, ApJ, 740, 13

Zhang, Q., & Fall, S. M. 1999, ApJ, 527, L81

Zinnecker, H., & Yorke, H. W. 2007, ARA&A, 45, 481